



# 1 Overview: On the transport and transformation of pollutants 2 in the outflow of major population centres - observational 3 data from the EMeRGe European intensive operational 4 period in summer 2017

5 M. Dolores Andrés Hernández<sup>1</sup>, Andreas Hilboll<sup>2,†</sup>, Helmut Ziereis<sup>3</sup>, Eric Förster<sup>4</sup>, Ovid O.  
6 Krüger<sup>5</sup>, Katharina Kaiser<sup>6,7</sup>, Johannes Schneider<sup>7</sup>, Francesca Barnaba<sup>8</sup>, Mihalis  
7 Vrekoussis<sup>2,18</sup>, Jörg Schmidt<sup>9</sup>, Heidi Huntrieser<sup>3</sup>, Anne-Marlene Blechschmidt<sup>1</sup>, Midhun  
8 George<sup>1</sup>, Vladyslav Nenakhov<sup>1,\*</sup>, Theresa Klausner<sup>3</sup>, Bruna A. Holanda<sup>5</sup>, Jennifer Wolf<sup>3</sup>, Lisa  
9 Eirenschmalz<sup>3</sup>, Marc Krebsbach<sup>10</sup>, Mira L. Pöhlker<sup>5</sup>, Anna B. Hedegaard<sup>2</sup>, Linlu Mei<sup>1</sup>, Klaus  
10 Pfeilsticker<sup>11</sup>, Yangzhuoran Liu<sup>1</sup>, Ralf Koppmann<sup>10</sup>, Hans Schlager<sup>3</sup>, Birger Bohn<sup>12</sup>, Ulrich  
11 Schumann<sup>3</sup>, Andreas Richter<sup>1</sup>, Benjamin Schreiner<sup>11</sup>, Daniel Sauer<sup>3</sup>, Robert Baumann<sup>3</sup>,  
12 Mariano Mertens<sup>3</sup>, Patrick Jöckel<sup>3</sup>, Markus Kilian<sup>3</sup>, Greta Stratmann<sup>3,\*\*</sup>, Christopher  
13 Pöhlker<sup>5</sup>, Monica Campanelli<sup>8</sup>, Marco Pandolfi<sup>13</sup>, Michael Sicard<sup>14,15</sup>, José L. Gómez-Amo<sup>16</sup>,  
14 Manuel Pujadas<sup>17</sup>, Katja Bigge<sup>11</sup>, Flora Kluge<sup>11</sup>, Anja Schwarz<sup>9</sup>, Nikos Daskalakis<sup>2</sup>, David  
15 Walter<sup>5</sup>, Andreas Zahn<sup>4</sup>, Ulrich Pöschl<sup>5</sup>, Harald Bönisch<sup>4</sup>, Stephan Borrmann<sup>6,7</sup>, Ulrich  
16 Platt<sup>11</sup>, and John Phillip Burrows<sup>1</sup>.

17 <sup>1</sup>Institute of Environmental Physics, University of Bremen, Bremen, Germany

18 <sup>2</sup>Laboratory for Modeling and Observation of the Earth System, Institute of Environmental Physics, Bremen,  
19 Germany.

20 <sup>3</sup>Deutsches Zentrum für Luft- und Raumfahrt (DLR), Institut für Physik der Atmosphäre, Oberpfaffenhofen,  
21 Germany

22 <sup>4</sup>Karlsruhe Institute of Technology, Institute of Meteorology and Climate Research, Karlsruhe, Germany

23 <sup>5</sup>Multiphase Chemistry Department, Max Planck Institute for Chemistry, Mainz, Germany

24 <sup>6</sup>Institute for Atmospheric Physics, Johannes Gutenberg University, Mainz, Germany

25 <sup>7</sup>Particle Chemistry Department, Max Planck Institute for Chemistry, Mainz, Germany

26 <sup>8</sup>National Research Council of Italy, Institute of Atmospheric Sciences and Climate (CNR-ISAC), Roma, Italy

27 <sup>9</sup>Leipzig Institute for Meteorology, Leipzig University, Leipzig, Germany

28 <sup>10</sup> Institute for Atmospheric and Environmental Research, University of Wuppertal, Wuppertal Germany

29 <sup>11</sup>Institute for Environmental Physics, University of Heidelberg, Heidelberg, Germany

30 <sup>12</sup>Institute of Energy and Climate Research IEK-8, Forschungszentrum Jülich, Jülich, Germany

31 <sup>13</sup>Institute of Environmental Assessment and Water Research, Barcelona, Spain

32 <sup>14</sup>CommSensLab, Dept. of Signal Theory and Communications, Universitat Politècnica de Catalunya, Barcelona,  
33 Spain

34 <sup>15</sup>Ciències i Tecnologies de l'Espai-Centre de Recerca de l'Aeronàutica i de l'Espai/Institut d'Estudis Espacials  
35 de Catalunya ), Universitat Politècnica de Catalunya Barcelona, Spain

36 <sup>16</sup>Dept. Earth Physics and Thermodynamics, University of Valencia, Burjassot, Spain

37 <sup>17</sup>Centro de Investigaciones Energéticas, Medioambientales y Tecnológicas (CIEMAT), Madrid, Spain

38 <sup>18</sup>Climate and Atmosphere Research Center (CARE-C), The Cyprus Institute, Nicosia, Cyprus

39 \*now at Flight Experiments, Deutsches Zentrum für Luft- und Raumfahrt (DLR), Oberpfaffenhofen, Germany

40 \*\*now at Deutsches Elektronen-Synchrotron DESY, Notkestr. 85, 22607 Hamburg, Germany

41 † deceased

42 Correspondence to: M.D. Andrés Hernández (lola@iup.physik.uni-bremen.de)

43 **Abstract.** EMeRGe (**E**ffect of **M**egacities on the transport and transformation of pollutants on the **R**egional to  
44 **G**lobal scale(s)) is an international project focusing on atmospheric chemistry, dynamics and transport of local and  
45 regional pollution originating in megacities and other major population centres (MPCs). Airborne measurements,  
46 taking advantage of the long range capabilities of the HALO research platform (High Altitude and Long range  
47 research aircraft, www.halo-spp.de), are a central part of the research project. In order to provide an adequate set  
48 of measurements at different spatial scales, two field experiments were positioned in time and space to contrast



49 situations when the photochemical transformation of plumes emerging from MPCs is large. These experiments  
50 were conducted in summer 2017 over Europe and in the inter-monsoon period over Asia in spring 2018. The  
51 intensive observational periods (IOP) involved HALO airborne measurements of ozone and its precursors,  
52 volatile organic compounds, aerosol particles and related species as well as coordinated ground-based ancillary  
53 observations at different sites. Perfluorocarbon (PFC) tracer releases and model forecasts supported the flight  
54 planning and the identification of pollution plumes.

55 This paper describes the experimental deployment of the IOP in Europe, which comprised 7 HALO research  
56 flights with aircraft base in Oberpfaffenhofen (Germany) for a total of 53 flight hours. The MPC targets London  
57 (Great Britain), Benelux/Ruhr area (Belgium, The Netherlands, Luxembourg and Germany), Paris (France),  
58 Rome and Po Valley (Italy), Madrid and Barcelona (Spain) were investigated. An in-flight comparison of HALO  
59 with the collaborating UK-airborne platform FAAM took place to assure accuracy and comparability of the  
60 instrumentation on-board.

61 Generally, significant enhancement of trace gases and aerosol particles are attributed to emissions originating in  
62 MPCs at distances of hundreds of kilometres from the sources. The proximity of different MPCs over Europe  
63 favours the mixing of plumes of different origin and level of processing and hampers the unambiguous  
64 attribution of the MPC sources. Similarly, urban plumes mix efficiently with natural sources as desert dust and  
65 with biomass burning emissions from vegetation and forest fires. This confirms the importance of wildland fire  
66 emissions in Europe and indicates an important but discontinuous contribution to the European emission budget  
67 that might be of relevance in the design of efficient mitigation strategies.

68 The synergistic use and consistent interpretation of observational data sets of different spatial and temporal  
69 resolution (e.g. from ground-based networks, airborne campaigns, and satellite measurements) supported by  
70 modelling within EMERGE, provides a unique insight to test the current understanding of MPC pollution  
71 outflows. The present work provides an overview of the most salient results and scientific questions in the  
72 European context, these being addressed in more detail within additional dedicated EMERGE studies. The  
73 deployment and results obtained in Asia will be the subject of separate publications.

## 74 **1 Introduction**

75 In recent decades, the number and size of major population centres (MPCs) have increased dramatically. The  
76 term MPC describes a single metropolitan area or converging urban conurbations with a population exceeding 10  
77 million inhabitants. In 1950, New York and Tokyo were the only two megacities in the world (Gardi, 2017)  
78 whereas for 2018 the United Nations reported 33 megacities and 48 urban agglomerations of 5 to 10 million  
79 inhabitants (UN, 2019). One cause of the recent growth of the number of MPCs is the rapid industrialisation of  
80 some parts of the world, in particular East Asia.

81 The economic consequences of urbanisation, the spatial growth of MPCs, and, in particular, the environmental  
82 and economical sustainability of megacities, have been a focus of recent discussion (ESPAS, 2018; Melchiorri et  
83 al., 2018; Hoole et al., 2019; Odendahl et al., 2019). The MPC has occasionally been presented as a favourable  
84 urban model, because the concentration of resources and services and the development of more effective  
85 mitigation strategies make it potentially less harmful for the environment than other more dispersed population  
86 distributions (Grimm, 2008; Dodman, 2009). However, the power required for transport, industrial and domestic



87 purposes, which is mostly generated from fossil fuel combustion, makes MPCs a growing and globally  
88 significant emission source of trace gases and aerosol particles for the troposphere.

89 High levels of urbanisation are associated with severe air pollution events which lead to adverse effects on  
90 human health (Lelieveld et al., 2015, 2020). Frequent exposure to poor air quality affects the respiratory,  
91 cardiovascular and neurocognitive systems, and is associated with cancer and premature death. The World  
92 Health Organisation has reviewed (WHO, 2013) the scientific evidence for the health risk from particulate  
93 matter (PM), and trace gases such as ozone ( $O_3$ ), carbon monoxide (CO), nitrogen dioxide ( $NO_2$ ), sulphur  
94 dioxide ( $SO_2$ ), metals (e.g. arsenic, lead and mercury) and polycyclic aromatic hydrocarbons (PAH). The effects  
95 of pollution originating from MPCs and the development of adequate control strategies are receiving growing  
96 attention as the public concern about air quality and the interaction of pollution and climate on a warming planet  
97 increases (e.g., Jacob and Winner, 2009). In that respect, the MPC emissions of environmental interest are  
98 aerosol particles, which contain sulphate ( $SO_4^{2-}$ ) and nitrate ( $NO_3^-$ ), particulate organic matter (POM), black  
99 carbon (BC), and ammonium ( $NH_4^+$ ), and long-lived greenhouse gases (GHG) such as carbon dioxide ( $CO_2$ ) and  
100 methane ( $CH_4$ ). Short-lived constituents of smog, such as nitrogen oxides ( $NO_x$ , i.e., NO and  $NO_2$ ), volatile  
101 organic compounds (VOC), and  $SO_2$  react to produce  $O_3$  and secondary aerosol particles and also have a climatic  
102 effect (UNEP, 2011; Mar, 2021).

103 The impact of aerosol particles on climate change has been investigated in detail (e.g. Pöschl, 2005; IPCC report,  
104 2014). The aerosol net radiative effect largely depends on the size and chemical composition of the aerosol  
105 particles which determine their scattering and absorption capabilities (e.g., Haywood and Boucher, 2000).  
106 Furthermore, aerosol particles act as cloud condensation nuclei (CCN) and modify the optical properties and  
107 lifetime of clouds. Anthropogenic aerosol is known to increase the number of cloud droplets while decreasing  
108 their sizes (e.g. Andreae and Rosenfeld, 2008; Campos Braga et al., 2017 and references therein). This results in  
109 extended cloud lifetimes, suppressing precipitation (Rosenfeld et al., 2008). Consequently, an accurate  
110 representation of mass and number concentration, size distribution and chemical composition of particles in  
111 models is essential to assess climatic change (Reddington et al., 2013).

112 Primary MPC emissions are transported and transformed into secondary pollutants such as  $O_3$  or secondary  
113 organic aerosols (SOA) and lead to smog episodes downwind of the source. Modelling studies using artificial  
114 aerosol tracers and estimations of deposition potentials, indicate that about 50% of MPC emitted particles with  
115 diameter  $\leq 2.5 \mu m$  ( $PM_{2.5}$ ) deposit more than 1000 km from their source (Kunkel et al., 2012). Chemical and  
116 physical processing of MPC emitted pollutants can in turn be affected by mixing with natural, biogenic and other  
117 anthropogenic emissions from regional sources or long-range transported from other areas (Lawrence et al.,  
118 2007, Monks et al., 2009, Lawrence and Lelieveld, 2010, and references therein).

119 The specific impact of the plumes from MPCs, therefore, depends not only on the type of emission sources (e.g.  
120 industry, traffic, domestic heating, and generation of electricity) but also on the variability of trace constituent  
121 emissions, the local meteorology and topography. The impact of MPC pollution on the atmospheric composition  
122 has been summarised by Zhu et al., (2012). In spite of the growing number of measurements campaigns,  
123 improved monitoring and modelling capabilities and the results achieved in the last decades, this review  
124 identifies important unresolved issues which limit the assessment of the impact of megacities on air quality and  
125 climate. Some examples are:



- 126 • the inaccurate modelling of the global effect of MPCs on anthropogenic emissions resulting from the  
127 current inconsistent local and regional MPC emission inventories (Denier van der Gon et al., 2011, Mayer  
128 et al., 2000; Butler and Lawrence, 2009),  
129 • the insufficient sub-grid parametrisation of MPCs in models,  
130 • the inadequate characterisation of pollution transport patterns, and,  
131 • the inaccurate prediction of cumulative pollution events observed in downwind regions of MPCs (Zhang et  
132 al., 2007; Kunkel et al., 2012).

133 In addition, modelling studies indicate that the combined effect of near-surface wind speeds and convection  
134 leads to significant latitudinal differences in regional to hemispheric dispersion characteristics (Lawrence et al.,  
135 2007 and references therein; Cassiani et al., 2013). Plumes emitted at higher latitudes are probably subject to  
136 faster transport than outflows from tropical or sub-tropical MPC, travel larger distances and for time scales  
137 exceeding ten days. Transport and transformation of MPC outflows are affected by the general weather patterns  
138 such as frontal passages and the frequency and duration of stagnation episodes, which are important for pollutant  
139 ventilation. The predicted changes in these patterns indicate that future air quality in MPCs will generally be less  
140 influenced by local emission sources than by the mixing of anthropogenic and natural emissions outside the  
141 MPC (Butler et al., 2012).

142 In summary, the overall assessment and prediction of the impact of pollution emitted by MPCs on tropospheric  
143 chemistry are challenging. Medium and long-term effects of anthropogenic emissions and their interaction with  
144 natural and biogenic emissions in the local and regional surroundings of individual MPCs are poorly understood  
145 and imprecisely quantified. In addition, controlling policies, changes in land cover and climate might  
146 substantially modify the relation between anthropogenic emissions and both natural aerosol and trace gases, as  
147 predicted by e.g., Butler et al., (2012), and recently reported for East Asia (Fu et al., 2016; Silver et al., 2018 and  
148 references herein; Leung et al., 2018). Decoupling the pollutant input upwind from the MPC emissions remains  
149 essential to establish accurate source-receptor relationships and effective control and mitigation policies. The  
150 current knowledge on all these aspects is still insufficient.

### 151 **1.1 Overarching objective of EMeRGe and methodology**

152 The EMeRGe (**E**ffect of **M**egacities on the transport and transformation of pollutants on the **R**egional to **G**lobal  
153 **s**cales) project began in 2016 and is part of the Priority research program of the German Research Foundation  
154 (DFG: Deutsche Forschungsgemeinschaft, www.halo-spp.de) to exploit the High Altitude and Long range  
155 research aircraft (HALO) for atmospheric science. EMeRGe has as an overarching objective the improvement of  
156 the current understanding of photochemical and heterogeneous processing of MPC plumes along expected  
157 transport pathways. This knowledge is required to assess the local and regional impacts of MPC outflows.

158 EMeRGe has a focus on airborne measurements and fostered cooperation with an international research  
159 partnership (hereinafter referred to as EMeRGe international) to facilitate the delivery and comprehensive  
160 analysis of a unique set of data from aircraft-, ground- and satellite-based sensors. The institutions currently  
161 involved in EMeRGe and EMeRGe international are listed in the supplementary information (see S1 and S2).

162 Europe and Asia are regions of the world with a differing heritage of pollution control strategies and notable  
163 differences in the number, size and proximity of MPCs as well as in the nature of emissions. For this reason, two  
164 field experiments were designed in EMeRGe to investigate the transport and transformation processes of  
165 pollution plumes originating from European and Asian MPCs. The first intensive observational period (IOP) was



166 carried out in Europe from 10 to 28 July 2017 with special focus on the study of active plume processing close to  
167 emission sources. The second IOP aimed at the investigation of long-range transport (LRT) of MPC outflows  
168 from the Asian continent to the Pacific during the spring inter-monsoon period and took place with HALO base  
169 in Taiwan from 10 March to 9 April 2018.  
170 EMeRGe aims to identify emission signatures and pollution hot spots by relating observations of pollutants to  
171 simulations and air mass trajectories. Chemical processing of the MPC emissions during transport is evaluated  
172 from the measurement of aerosol particles and trace gases. In particular O<sub>3</sub> and its precursors provide  
173 information about the photochemical activity and the transformation of primary into secondary pollutants within  
174 the MPC outflows. Furthermore, measurements at different altitudes downwind of selected MPCs are required  
175 for the identification of plume transport. Mixing of MPC plumes with biomass burning (BB) and mineral dust  
176 transport events and / or convection processes might have an impact in the processing of the MPC outflows.  
177 Finally, the accuracy and suitability of atmospheric chemistry models is investigated by comparing EMeRGe  
178 observations with dedicated simulations from state-of-the-art global and regional atmospheric chemistry models.  
179 The present article describes the experimental design and specific objectives of the IOP of EMeRGe in Europe.  
180 It highlights key research questions and some of the scientific results, which are further explored in forthcoming  
181 papers.

## 182 **2 EMeRGe in Europe**

### 183 **2.1 MPC pollution in Europe**

184 The level of urbanisation in Europe is presently ~ 74% and is expected to further increase by 10% up to the  
185 middle of this century (UN, 2019). Large conurbations are a more abundant European urban phenomena than  
186 megacities, of which there are a few. According to the European Environment Agency (EEA), the emission of  
187 air pollutants and precursors has decreased across Europe from the year 2000 to the present, partly as a result of  
188 the EU air quality legislation. Emissions of CO, BC, NO<sub>x</sub> and non-methane VOCs have been reduced by around  
189 30% and those of sulphur oxide (SO<sub>x</sub>, primarily SO<sub>2</sub>) up to 77%. Nevertheless, the daily and annual O<sub>3</sub> and PM  
190 limit concentrations for protection of human health are often exceeded in several areas of the continent (EEA,  
191 2019). Significant differences in pollution and photochemical episodes between Northern and Central Europe  
192 and the Mediterranean region are regularly observed, in particular due to the differences in solar actinic radiation  
193 (Kanakidou et al., 2011).

194 Europe air quality is frequently influenced by LRT of North American pollution as captured by airborne  
195 measurements and investigated in several model studies (e.g. Stohl et al., 2003; Huntrieser and Schlager, 2004;  
196 Huntrieser et al., 2005). Some evidence of LRT of Asian pollution to the Mediterranean has also been  
197 documented (Lawrence and Lelieveld, 2010; Lelieveld et al., 2002). The chemical signatures of LRT of  
198 pollutants vary depending on pollutant lifetime and mixing. Some recent modelling studies infer that the impact  
199 of non-European pollution on the European surface O<sub>3</sub> annual average is larger than previously expected (Jonson  
200 et al., 2018).

201 In recent years, large European projects such as MEGAPOLI (<http://megapoli.dmi.dk>) and CityZen (Megacity-  
202 Zoom for the Environment; <http://www.cityzen-project.eu>), provided comprehensive theoretical and  
203 experimental data about MPCs in Europe. MEGAPOLI was conducted in Paris in summer 2009 and winter 2010  
204 (Beekmann et al., 2015) and investigated source apportionment and photochemical processing of emitted



205 gaseous and particulate substances using several ground-based stations and measurement vehicles (Crippa et al.,  
206 2013; Freutel et al., 2013; von der Weiden-Reinmüller et al., 2014). Beekmann et al., (2015) estimated the  
207 impact of the urban emissions from the Paris megacity to be relatively low in comparison to other external  
208 industrial sources of pollution. Aircraft measurements were restricted to the near-field outflow (up to 200 km) in  
209 the boundary layer below 700 m asl (Brands et al., 2011; Freney et al., 2014). In comparison, EMeRGe focuses  
210 on the impact of different MPCs in middle and Southern Europe and investigates atmospheric pollution plumes  
211 over much larger latitudinal and longitudinal scales.

212 CityZen (2008-2011) studied air pollution in and around selected megacities and emission hotspots by using in-  
213 situ and satellite observations (Hilboll et al., 2013; Vrekoussis et al., 2013) as well as a series of different scale  
214 models (Colette et al., 2011; Im et al., 2012). The project focused on selected MPCs such as the Eastern  
215 Mediterranean, the Po Valley, the Benelux region, and the Pearl River Delta for intensive case studies but, in  
216 contrast to EMeRGe, did not conduct measurements of the photochemical evolution in the outflow of the studied  
217 regions.

218 The above studies focused on trace gases linked to air quality and provided relatively sparse information on  
219 GHGs. Long-lived greenhouse gases such as CH<sub>4</sub> and CO<sub>2</sub> emitted from individual European urban areas have  
220 been investigated in airborne and ground-based studies, e.g. for London (O'Shea et al., 2014; Helfter et al., 2016;  
221 Pitt et al., 2019), Paris (Bréon et al., 2015; Lian et al., 2019), Cracow (Kuc et al., 2003; Zimnoch et al., 2019),  
222 Berlin (Klausner et al., 2020) and Rome (Gioli et al., 2014). Collectively, they report on inconsistencies between  
223 the current emission inventories and measurements. This indicates the need for further experimental  
224 investigation of the GHG budget in Europe.

225 The capability of chemistry-transport models (CTMs) to reproduce the variability in air quality of major  
226 anthropogenic emission hot spots in Europe has been evolving and investigated (e.g. Colette et al., 2011, 2012).  
227 State-of-the-art models reasonably captured trends of primary species but the modelling of O<sub>3</sub> changes and  
228 projected exposure to O<sub>3</sub> pollution in Europe is still challenging.

229 Overall, the proximity of most European MPCs results in the mixing of different pollution plumes during their  
230 transport. This hampers the identification of the air mass origin. BB and mineral dust events have, moreover, a  
231 variety of impact on the total European burden of atmospheric aerosol and trace gases. Particularly in Southern  
232 Europe, BB and mineral dust plumes occur frequently and can significantly affect the chemical processing of  
233 MPC pollution plumes. BB events from agriculture or wildland fires have a strong seasonal pattern in Europe  
234 (Barnaba et al., 2011). Wildfires emit similar to MPC large amounts of pollutants, e.g. PM, NO<sub>x</sub>, CO, VOC and  
235 PAH (Andreae, 2019). The number and severity of wildfires are expected to increase in Europe under warmer  
236 and drier conditions as a co-effect of climate change (Forzieri et al., 2017; Guerreiro et al., 2018; Turco et al.,  
237 2018). Desert dust episodes of different intensity originating in North Africa frequently affect air mass  
238 composition and atmospheric stratification over the Mediterranean (Kalivitis et al., 2007; Pey et al., 2013;  
239 Pikridas et al.; 2018), in spring and in summer (Barnaba and Gobbi, 2004; Gkikas et al., 2013; Pey et al., 2013)..

## 240 **2.2 Specific scientific questions relevant to EMeRGe in Europe**

241 EMeRGe in Europe focuses on three primary scientific goals addressing a series of related specific questions:

### 242 I. Identification of emission signatures in MPC plumes over Europe

- 243 • Are there individual MPC emission signatures identifiable in pollution plumes measured over Europe?



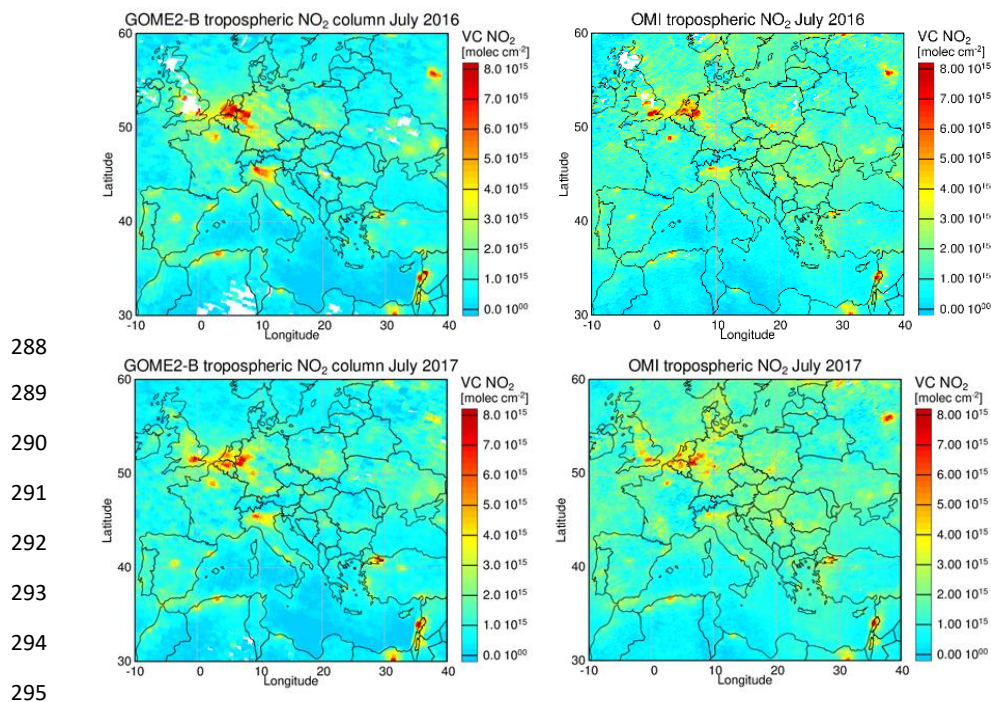
- 244 • Is it possible to unambiguously identify MPC plumes after transport times of hours or days by tagging the air  
245 masses in the source regions with passive tracers released at the surface and using airborne sensors  
246 downwind?
- 247 • Can the effect of plumes from different emission sources (e.g., anthropogenic, BB, and/or a mixture of them)  
248 on the oxidation potential of the atmosphere be inferred from changes in the NO/NO<sub>y</sub> and NO/VOC ratios in  
249 airborne measurements?
- 250 • Can airborne measurements detect signatures of urban and other emission sources of CH<sub>4</sub> in Europe  
251 adequately?
- 252 • How abundant are organic acids in European MPC plumes relative to inorganic acids and what are their main  
253 sources?
- 254 • Are satellite measurements of aerosol and trace gases capable of supporting the identification of MPC plumes  
255 and dominant transport paths?
- 256 II. Investigation and assessment of chemical processing in MPC pollution outflows
- 257 • Is the photochemical activity of MPC plumes readily related to changes in concentrations of radicals and  
258 their precursors measured by the HALO sensors?
- 259 • Is the photochemical ageing of MPC plumes well described by the chemical clocks inferred from the  
260 airborne measurements of trace gases and aerosol particles?
- 261 • Can the O<sub>3</sub> production efficiency and NO<sub>x</sub>-and VOC-sensitive regimes in MPC plumes be determined? How  
262 do these change with respect to the plume age and mixing with background air?
- 263 • Can the importance of the role of formaldehyde (HCHO) as an intermediate product in the oxidation of  
264 VOCs, and glyoxal (C<sub>2</sub>H<sub>2</sub>O<sub>2</sub>) and methylglyoxal (C<sub>3</sub>H<sub>4</sub>O<sub>2</sub>) in secondary aerosol formation be inferred from  
265 their airborne measurement in MPC pollution plumes?
- 266 • Which processes control the heterogeneous formation of HONO in polluted air masses of MPC origin in the  
267 BL and lower troposphere over Europe?
- 268 III. Assessment of the relative importance of MPCs as sources of pollution over Europe
- 269 • How important are BB and dust emissions to MPC plume photochemistry over Europe in the summer 2017?
- 270 • How do the regional CH<sub>4</sub> urban emission distributions in Europe compare with previous observations in the  
271 same areas?
- 272 • Is it possible to assess the relative role of primary and secondary pollutants in the proximity and in the  
273 outflow of MPCs?
- 274 • Are state-of-the-art chemical models capable of adequately simulating transport and transformation of  
275 European MPC outflows?

### 276 **2.3 Selection of MPC targets and measurement strategy**

277 The dominant source of NO<sub>x</sub> and CO in the planetary boundary layer (PBL) in Europe is anthropogenic activity,  
278 primarily fossil fuel combustion and biomass burning. Cloud free monthly average tropospheric composites of  
279 NO<sub>2</sub> columns retrieved from GOME2-B and OMI instruments on-board the MetOp-B and Aura satellites were  
280 used to identify the major MPCs in Europe during July in the EMERGe study. Due to its short lifetime, NO<sub>2</sub> is a  
281 good indicator of the origin of emission sources. The tropospheric NO<sub>2</sub> columns retrieved in July 2016 during  
282 the campaign preparation showed enhanced NO<sub>2</sub> concentrations over the London, Moscow and Paris megacities,



283 over large urban agglomerations such as the Benelux/Ruhr metropolitan area in Central Europe and the Po  
284 Valley in Northern Italy, and over the conurbations in Southern Europe such as Rome, Naples, Madrid and  
285 Barcelona. The satellite observations during the EMERGe IOP in 2017 confirmed the NO<sub>2</sub> hot spots identified  
286 (Fig. 1). The differences observed are most likely related to the special weather situation in 2017, as described in  
287 Sect. 3.1.



296 **Figure 1:** Satellite tropospheric NO<sub>2</sub> columns retrieved from GOME2-B (left panel, overpass at 9:30 h local time),  
297 and OMI (right panel, overpass at 12:45 h local time) instruments for a) July 2016, a year before the EMERGe IOP in  
298 Europe (top), and b) the IOP period in July 2017 (bottom).

299 CO was used in dispersion calculations to identify anthropogenic pollution from combustion. CO is a suitable  
300 tracer for transport pathways due to its relatively long atmospheric lifetime which is primarily lost by reaction  
301 with the OH radical and varies between a few weeks and a few months. To address the EMERGe scientific  
302 objectives, the day-to-day flight planning focused on the identification of the location of the plumes from the  
303 targeted MPC outflows during potential flights. For this, the following forecast tools were exploited:

- 304 i) ECMWF (European Centre for Medium-Range Weather Forecasts, <https://www.ecmwf.int/>) and NCEP  
305 (National Center for Environmental Prediction, <https://www.ncep.noaa.gov/>) weather forecasts,
- 306 ii) NOAA (National Oceanic and Atmospheric Association) HYSPLIT (Hybrid Single Particle Lagrangian  
307 Integrated Trajectories, <https://www.arl.noaa.gov/hysplit/>) model for forward dispersion calculations using  
308 CO as a tracer of pollution. These forecasts, carried out by DLR (Deutsches Zentrum für Luft- und  
309 Raumfahrt), assume MPCs to be continuous emission sources and provide snapshots as well as horizontal  
310 and vertical cross sections of the selected outflows at certain times.





311 iii) Tailor-made CO and stratospheric ozone tracer simulations provided by CAMS (Copernicus Atmosphere  
312 Monitoring Service, <http://atmosphere.copernicus.eu>) through its field campaign support (see also  
313 Flemming et al., 2019).  
314 A list of model simulations and satellite observations used for flight planning is given in Tables 1a and 1b. These  
315 are described in more detail in the supplement (see S3). The dedicated mission support tool (MSS, Mission  
316 Support System; Rautenhaus et al., 2012) provided additional assistance in the flight planning.

317  
318 **Table 1a:** Model simulations used for flight planning during EMerGe in Europe

Name	Type	Resolution of model output	Institution
CAMS-global (CIFS-TM5)	CTM	0.4° x 0.4°; 60 vertical levels	ECMWF
CAMS-regional ensemble	Median of 7 regional CTMs	0.1° x 0.1°; surface, 50, 250, 500, 1000, 2000, 3000, 5000 km	ECMWF
EMEP	regional CTM	0.25° E x 0.125° N; 20 vertical levels	Norwegian Meteorological Institute
HYSPLIT	Lagrangian trajectory model	0.1° x 0.1°; 20 vertical levels	NOAA/DLR
FLEXPART	Lagrangian trajectory model	1min /10 days back ECMWF-ERA5; 0.25° horizontal	NILU

319

320 **Table 1b:** Satellite observations used during EMerGe in Europe

Sensor name	Satellite	Equator crossing time	Footprint	Institution
GOME-2	MetOp-B	10:30 LT	40 x 80 km <sup>2</sup>	IUP Uni-Bremen
OMI	EOS-Aura	13:30 LT	13 x 24 km <sup>2</sup>	IUP Uni-Bremen
SEVIRI	MSG	Geostationary	3 x 3 km <sup>2</sup>	ICARE

321

322 The flight track and patterns available to HALO were constrained by a) flight restrictions from the air traffic  
323 authorities and special military used airspaces (SUA), and b) the unstable meteorological conditions dominating  
324 in Central Europe during the measurement period (see Sect. 3.1).

325 Flight tracks to investigate the plumes from the MPC targets, London (Great Britain), Benelux/Ruhr area  
326 (Benelux countries and Germany, hereinafter referred to as BNL/Ruhr), Paris (France), Rome and Po Valley  
327 (Italy), and Madrid and Barcelona (Spain) were selected. It was possible to fly these flight tracks under  
328 favourable conditions typically more than once during the EMerGe IOP, improving somewhat the  
329 representativeness of the measurements.



330 The HYSPLIT dispersion forecast indicated that the MPC pollution plumes targeted by EMeRGe resided  
331 predominantly below 3000 m. Consequently, the flights over Europe made use of the HALO long-endurance  
332 capabilities to fly in the PBL and incorporated vertical shuttles. The flight pattern involve the descent or climb  
333 between holding altitudes, coupled with long flight tracks at a given flight altitude. Typically, three flight levels  
334 (FL), upwind or downwind of the target MPCs are part of the shuttle. Some of the MPC outflows were tagged by  
335 a coordinated release of a perfluorocarbon (PFC) tracer at the ground (see Sect. 2.4.2).

336 All HALO flights started from the DLR base Oberpfaffenhofen (OP), located Southwest of Munich in Germany.  
337 The flights are named E-EU-FN, where E stands for EMeRGe, EU for Europe and FN are the two digits of the  
338 flight number. Details about flight tracks and flight routes are provided in Sect. 3.3.

#### 339 **2.4 EMeRGe instrumentation**

340 The pollutant measurements made aboard HALO were enhanced during the EMeRGe IOP in Europe by  
341 coordinated flights with other airborne sensors, complementary ground-based measurements and model  
342 predictions. In this manner, the EMeRGe international cooperation provided additional aircraft-, satellite- and  
343 ground-based observations and modelling studies during the preparation and execution phases of the EMeRGe  
344 IOP in Europe, as described in the following sections.

##### 345 **2.4.1 HALO payload**

346 A key element of the EMeRGe data are the airborne measurements made on-board HALO, a Gulfstream G550  
347 business jet modified and specifically equipped for scientific research (see [www.halo.dlr.de](http://www.halo.dlr.de)). The HALO  
348 payload for EMeRGe comprises a set of state-of-the-art instrumentation for the measurement of trace gases and  
349 aerosol particles. Table 2 summarises target species and parameters measured by the instruments installed on-  
350 board HALO, which are complemented by the HALO ancillary measurements (BAHAMAS, see S4 in the  
351 supplement) during the EMeRGe campaign in Europe.

352

353 **Table 2:** HALO instrumental payload for EMeRGe: PeRCA: Peroxy Radical Chemical Amplification; CRDS: Cavity Ring-  
354 Down Spectroscopy; HVS: High Volume Sampler; GC-C-IRMS: Gas Chromatography Combustion Isotope Ratio Mass  
355 Spectrometry; PTR-MS: Proton-Transfer-Reaction Mass Spectrometer; CI-ITMS: Chemical Ionisation Ion Trap Mass  
356 Spectrometry; GC-MS: Gas chromatography-mass spectrometry analysis; PAN: Peroxyacetyl nitrate;  $\delta^{13}\text{C}(\text{CH}_4)$ : Isotopic  
357 signature of methane; PFC: Perfluorinated carbon chemicals; DOAS: Differential Optical Absorption Spectrometry; AT-BS:  
358 Adsorption Tube and Bag air Sampler; TD-GC-MS: Thermal Desorption Gas Chromatography and Mass Spectrometry; ToF-  
359 AMS: Time of Flight- Aerosol Mass Spectrometry; SP2: Single Particle Soot Photometry; CCNC: Cloud Condensation  
360 Nucleus Counting; MI: Multi Impactor for aerosol off-line analysis; CPC: Condensation Particle Counting; DMA:  
361 Differential Mobility Analysis; OPC: Optical Particle Counting; PSAP: Particle Soot Absorption Photometry. See details and  
362 HALO ancillary measurements in the supplement. The instrument details are given in the quoted literature.



Trace gas-in situ measurements				
Species/parameters	Acronym	Institution	Technique/Instrument	Reference
$\text{RO}_2^* = \text{HO}_2 + \sum \text{RO}_2$	PeRCEAS	Univ. Bremen	PeRCA + CRDS	George et al., 2020
VOC/C isotope ratios	MIRAH	Univ. Wuppertal	HVS/GC-C-IRMS	Wintel et al., 2013
OVOC	HKMS	KIT Karlsruhe	PTR-MS	Brito and Zahn, 2011
$\text{O}_3$	FAIRO	KIT Karlsruhe	UV-Photometry/ Chemiluminescence	Zahn et al., 2012
$\text{O}_3, \text{CO}$	AMTEX	DLR-IPA	UV-Photometry/ VUV-Fluorimetry	Gerbig et al., 1996
$\text{NO}, \text{NO}_y$	AENEAS	DLR-IPA	Chemiluminescence/ Gold converter	Ziereis et al., 2004
$\text{SO}_2, \text{HCOOH}$	CI-ITMS	DLR-IPA	CI-ITMS	Speidel et al., 2007
a) $\text{CO}_2$ and $\text{CH}_4$			a) CRDS	Chen et al., 2010
b) PAN	CATS	DLR-IPA	b) GC-MS	Volz-Thomas et al., 2001
c) $\delta^{13}\text{C}(\text{CH}_4)$			c) GC-IRMS	Fisher et al., 2006
PFC tracer	PERTRAS	DLR-IPA	AT-BS/TD-GC-MS	Ren et al., 2015
Trace gas- remote sensing measurements				
Species/parameters	Acronym	Institution	Technique/Instrument	Reference
$\text{NO}_2, \text{HONO}, \text{BrO}, \text{CH}_2\text{O}, \text{C}_2\text{H}_2\text{O}_2, \text{C}_3\text{H}_4\text{O}_2, \text{SO}_2, \text{IO}$	mini-DOAS	Univ. Heidelberg	DOAS / UV-nIR: 2D optical spectrometer	Hüneke et al., 2017
$\text{NO}_2, \text{CH}_2\text{O}, \text{C}_2\text{H}_2\text{O}_2, \text{H}_2\text{O}, \text{SO}_2, \text{BrO}, \text{O}_3$	HAIDI	Univ. Heidelberg	DOAS / 3x2D-imaging spectrometers	General et al., 2014
Aerosol measurements				
Species/parameters	Acronym	Institution	Technique/Instrument	Reference
Particle composition	C-ToF-AMS	MPIC Mainz & Univ. Mainz	ToF-AMS	Schulz et al., 2018
BC, CCN, microscopic properties	CCN-Rack	MPIC Mainz	SP2 CCNC, MI	Holanda et al., 2020 Wendisch et al., 2016
Particle size distribution/number concentration	AMETYST	DLR-IPA	CPC, OPC, PSAP, DMA	Andreae et al., 2018
Other parameters				
Species/parameters	Acronym	Institution	Technique/Instrument	Reference
Spectral actinic flux density (up/down) Photolysis frequencies	HALO-SR	FZ Jülich	CCD spectro- radiometry	Bohn and Lohse, 2017
Basic aircraft data	BAHAMAS	DLR -FX	various	Mallaun et al., 2015

363

364



365

#### 366 **2.4.2 Perfluorocarbon tracer experiments**

367 Tracer experiments were performed during EMeRGe using perfluorocarbon compounds (PFC). PFCs are  
368 suitable tracers as they are chemically inert, do not interact with aerosol and clouds, have very low background  
369 in the atmosphere (~10 ppqv), and can be detected at mixing ratios as low as 1 ppqv. The tracer experiments  
370 involved the release of a mixture of PFCs at a site close to the centre of an MPC. These experiments establish  
371 Lagrangian connections between MPC centres and HALO measurements downwind. They support the studies on  
372 the formation of secondary gases and aerosol particles from the primary emissions in the pollution plumes. In  
373 addition, tracer experiments were used to test the dispersion parametrisations in transport models.

374 During the EMeRGe IOP in Europe, PMCH (C<sub>7</sub>F<sub>14</sub>, 350 amu) was the PFC used to tag polluted air masses at the  
375 release sites. The tracer was sampled on sorption tubes on-board and subsequently analysed in the laboratory, as  
376 described in Ren et al., (2013, 2015). The limit of detection (LOD) and limit of quantification (LOQ) of the PFC  
377 analysis system are 0.7 ppqv and 2 ppqv, respectively, for sorption tube samples loaded for 3 min. The precision  
378 and accuracy are 6% and 11%, respectively. Three tracer releases were performed two in the city centre of  
379 London at the Imperial College on 17 and 26 July 2017 and one in the Ruhr region, at the University of  
380 Wuppertal on 26 July 2017 in Germany. The HALO flights and pattern for the tracer sampling in the plumes  
381 downstream were optimised with respect to the time of the tracer releases by using HYSPLIT tracer dispersion  
382 forecasts. Post-campaign comparisons of the tracer measurements were performed with HYSPLIT and  
383 FLEXPART. More details of the EMeRGe tracer experiments are described in Schlager et al. (2021, in  
384 preparation).

#### 385 **2.4.3 Other airborne observations**

386 The Facility for Airborne Atmospheric Measurements (FAAM, see [www.faam.ac.uk](http://www.faam.ac.uk)) from the UK Natural  
387 Environment Research Council (NERC) joined the EMeRGe IOP in Europe. It made a set of flights around  
388 London in the Southeast of England in the UK.

389 To assure the accuracy and comparability of the instrumentation on-board, one research flight on 13 July 2017  
390 was dedicated to common and simultaneous measurements of HALO and FAAM in a so-called blind  
391 intercomparison exercise. The two research aircraft flew in close formation for 1.6 hours around noon in the  
392 northern part of a restricted airspace. In total, 24 instruments were operated on the two aircraft and provided data  
393 for the comparison. The data obtained were uploaded under blind conditions and evaluated by an external  
394 referee. In addition, observational data were collected from the German Meteorological Service at the  
395 observatory Hohenpeissenberg (47°48'N, 11°01'E) located downwind of the aircraft track, and model results  
396 were generated from 6 models and interpolated along the common flight path. A summary of the measured and  
397 modelled data available for direct comparisons is provided in the supplement (S5). Overall, about half of the data  
398 pairs from the sets of measurements on the two aircraft differ less than their combined error estimates. In most  
399 cases, the differences between the measurements are smaller than the deviations between the model results. For  
400 some instruments, the comparison led to significant data analysis improvements. The root mean square  
401 deviations between the measurements on FAAM and HALO were less than estimated errors for temperature,  
402 relative and absolute humidity, CO<sub>2</sub>, benzene, vertical and horizontal wind components, and methane. The



403 largest discrepancies were found for some VOCs, sulphate aerosol and black carbon mass and number  
404 concentrations. The instrumental accuracy assessment from the comparison results in Schumann (2020).  
405 The Italian Sky Arrow Environmental Research Aircraft (Gioli et al., 2009) from the National Research Council  
406 of Italy (CNR) undertook additionally two research flights up to 2000 m over the city of Rome (Italy)  
407 concurrently with the HALO overpass flight on 11 July 2017. The aircraft was equipped with instrumentation  
408 targeting some aerosol parameters (total number and size distribution), gas concentrations (CO<sub>2</sub>, O<sub>3</sub>, H<sub>2</sub>O) and  
409 key meteorological data (temperature, pressure and wind).

#### 410 **2.4.4 Collocated ground-based observations**

411 EMeRGe was supported by measurements from a variety of ground-based stations which complemented the  
412 HALO observations. These measurements were also used for the planning of subsequent HALO flights and  
413 occasionally for in-flight manoeuvres.

414 For example, the European Aerosol Research Lidar Network, EARLINET (Pappalardo et al., 2014), a key  
415 component of the Aerosols, Clouds and Trace gases Research Infrastructure ACTRIS, joined as an EMeRGe  
416 international partner and provided coordinated, ground-based lidar measurements. Additional support was  
417 provided from other non-EARLINET lidar stations. Altogether, 19 stations supported the EMeRGe IOP in  
418 Europe. The specifications and location of the operated lidars as well as the coordinated measurements for each  
419 HALO flight are included in the supplement (S6).

420 In addition, measurements from several ceilometer networks contributed to EMeRGe, in particular the German  
421 Ceilonet of DWD (Deutscher Wetterdienst), the Italian ALICENet (Automated Lidar-Ceilometer network) and  
422 the ceilometers of the Belgian RMI (Royal Meteorological Institute of Belgium). The RMI also provided ozone  
423 soundings from Uccle three times per week. Additional ground-based and in-situ measurements were provided  
424 from ACTRIS stations, and sun-photometer measurements from AERONET (Aerosol Robotic Network, Holben  
425 et al., 1998)

426 Two ground-based field campaigns deploying both remote sensing and in-situ measurements concurred with the  
427 EMeRGe IOP: ACTRIS-2 in the Po Valley, Italy (see <http://actris-cimone.isac.cnr.it/>), and HOUSE (High  
428 Ozone, Ultrafine particles and Secondary aerosol Episodes in urban and regional backgrounds) in Northeast  
429 Spain (see <https://www.idaea.csic.es/egar/portfolio-items/house/>). These data were made accessible for the  
430 analysis in the framework of EMeRGe international.

#### 431 **2.4.5 Satellite observations**

432 Near real-time tropospheric NO<sub>2</sub> columns from the GOME-2 instruments on MetOp-A (GOME2-A; 40 km x 40  
433 km resolution) and MetOp-B (GOME2-B; 80 km x 40 km resolution) as well as OMI (13 km x 24 km resolution  
434 at nadir) on NASA Aura were provided in July and August 2017 to support flight planning and quick-look  
435 interpretation of the EMeRGe IOP observations. NO<sub>2</sub> columns are calculated using the method described in  
436 Richter et al., (2005, 2011), and Hilboll et al., (2014). The retrievals use GOME-2 lv1 data provided by  
437 EUMETSAT and OMI lv1 data provided by NASA. They are not official GOME-2 / OMI data products. The  
438 plots were usually available 6 hours after measurement (<https://www.iup.uni-bremen.de/does/emerge.htm>).

439 In addition, daily values of the aerosol optical thickness (AOT) at 0.55 μm were retrieved from the Spinning  
440 Enhanced Visible and Infrared Imager (SEVIRI) on-board the Meteosat Second Generation (MSG) satellite. The  
441 spatial and temporal resolutions for the SEVIRI AOT product are 3 km at nadir and 15 minutes, respectively.



442 The SEVIRI AOT product over land (SMAOL\_AOT.v1.3.6) and ocean (SEV\_AER-OC-L2.v1.04) (Thieuleux et  
443 al., 2005; Bréon et al., 2011) are merged and post-processed by using the eXtensible Bremen Aerosol/cloud and  
444 surfacE parameters Retrieval (XBAER) algorithm to minimise potential cloud contamination (Mei et al., 2017a,  
445 2017b).

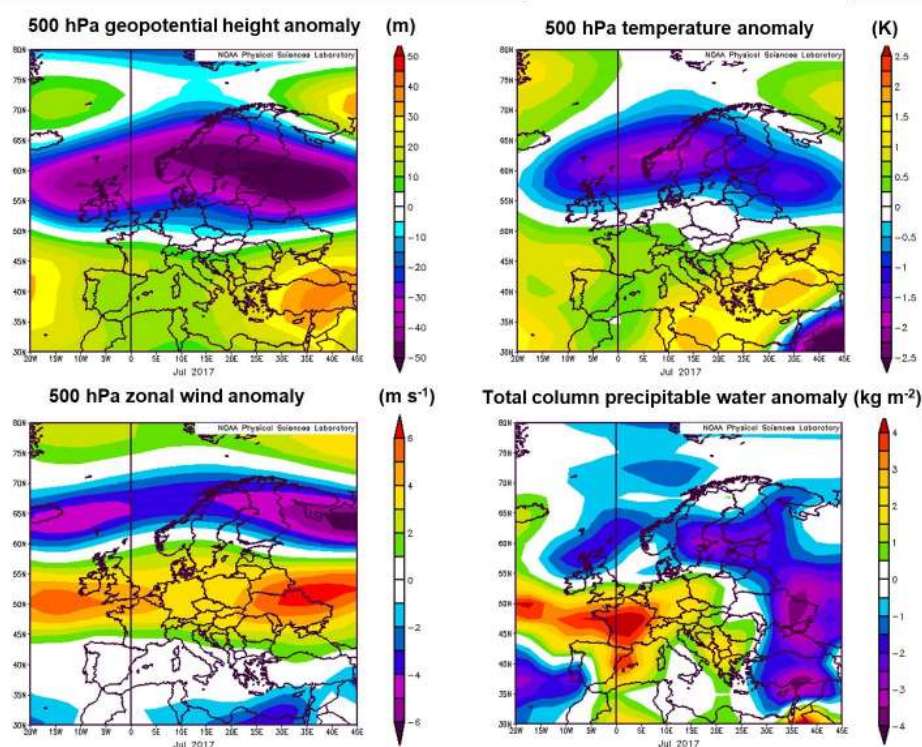
### 446 **3 Characteristics of the EMerGe IOP in Europe and its conditions**

447 The EMerGe IOP in Europe took place from 10 July 2017 to 28 July 2017. The results obtained are analysed  
448 considering the prevailing meteorological conditions in Europe during this period and the characteristics of the  
449 deployment in the different flight legs.

#### 450 **3.1 Meteorological conditions**

451 The month of July was selected for the EMerGe investigation because the summer period in Europe offers  
452 frequent events of high temperature and high insolation, which result in active photochemical processing of the  
453 air masses.

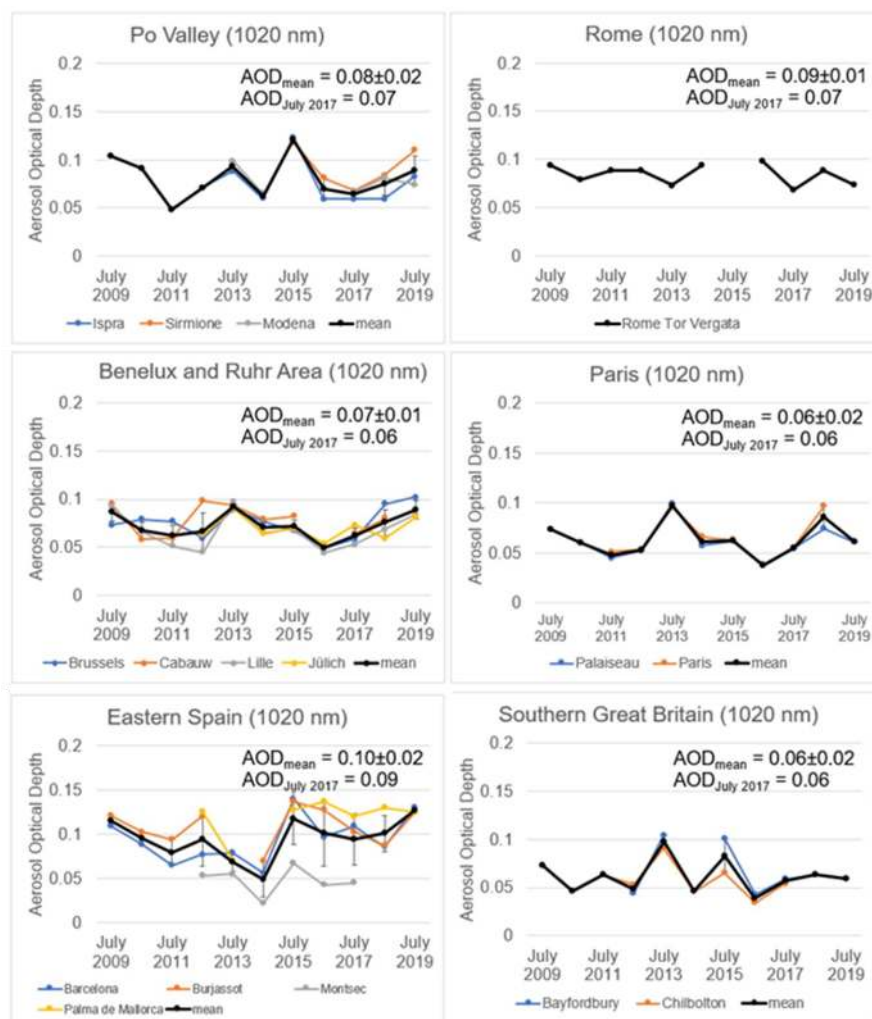
454 The monthly average weather conditions of July 2017 were evaluated by comparing 500 hPa geopotential height,  
455 temperature, wind and precipitable water with a 30-year (1981-2010) reference climatology using NCEP  
456 reanalysis data (Kalnay et al., 1996). As shown in Fig. 2, stagnation events, high temperatures and insolation  
457 dominated Southern Europe similar to the average of the 30-year climatology. At the ground, the summer 2017  
458 was characterised by heatwaves, which contributed to the propagation of frequent fire events especially on the  
459 Iberian Peninsula (EEA, 2018). In contrast, an upper-level negative pressure and temperature anomaly was  
460 located over Northern Europe. The polar front was positioned further southwards than is usual with anomalously  
461 high upper-level wind speeds over Central Europe. These conditions favoured the passage of upper-level troughs  
462 associated with mid-latitude cyclones and enhanced precipitation over Central Europe. A cut-off low located  
463 over Great Britain during approximately the last ten days of the campaign affected the average weather  
464 conditions. Thunderstorms frequently developed near the Alps over Southern Germany and Northern Italy.



465  
466 **Figure 2:** Mean anomalies of the 500 hPa geopotential height (top left panel), temperature (top right), zonal wind (bottom  
467 left) and total column precipitable water (bottom right) for July 2017 with respect to a 1981-2010 July climatology based on  
468 NCEP reanalysis data (Kalnay et al. 1996). Total column precipitable water is the amount of water potentially available in the  
469 atmosphere for precipitation from the surface to the upper edge of the troposphere. NCEP reanalysis data and images  
470 provided by the NOAA/ESRL Physical Sciences Laboratory, Boulder Colorado (<http://psl.noaa.gov/>).

### 471 3.2 Aerosol optical depth

472 The aerosol load in the target regions during the EMERGe IOP in July 2017 was investigated. Monthly averages  
473 of aerosol optical depths (AODs) measured in July 2017 at 14 AERONET sun-sky photometer sites  
474 (AERONET, 2020), in all six EMERGe target regions (see S7 in the supplement) were compared to the 10-year  
475 AOD July average between 2009 and 2019. Throughout this study, only version 3 level 2.0 data were considered  
476 (Giles et al., 2019). The measurements at 1020 nm presented here have the largest data coverage (139 data  
477 points). Data for other wavelengths (500 nm, 118 data points; and 675 nm, 132 data points) are shown in the  
478 supplement. Figure 3 displays the derived AODs. The AODs measured in July 2017 close to Paris and in  
479 Southern Great Britain are very similar in the period 2009 to 2019. The AODs are within the standard deviation  
480 of the 10-year average for the majority of the other stations with relative deviations ranging from 10% to 14%. In  
481 contrast, the AOD observed in the Rome region was 22% lower than the 10-year average.



482

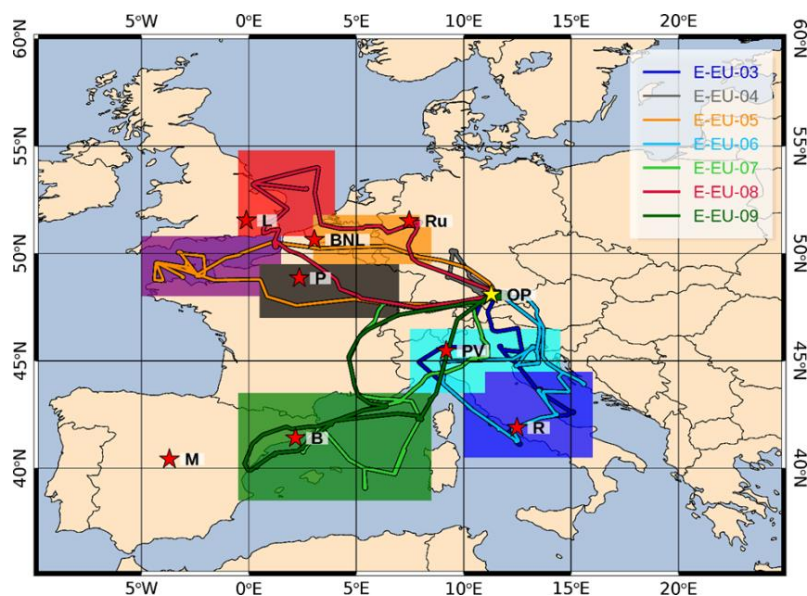
**Figure 3:** AODs derived at 1020 nm for AERONET stations in all six target regions of EMERGe in Europe. Black lines show mean AOD values. The AODs derived for July 2017 and the 2009 to 2019 average are shown on each diagram. The AODs from July 2017 are representative of the average AODs from 2009 to 2019.

### 483 3.3 Flight routes and HALO flight tracks

484 The EMERGe IOP in Europe comprised seven HALO flights from 11 July 2017 to 28 July 2017, for a total of 53  
485 flight hours. As mentioned in Sect. 2.3, all HALO flights started from OP in Germany. The flight tracks are  
486 shown in Fig. 4 and Table 3 summarises the corresponding flight times and targets.

487

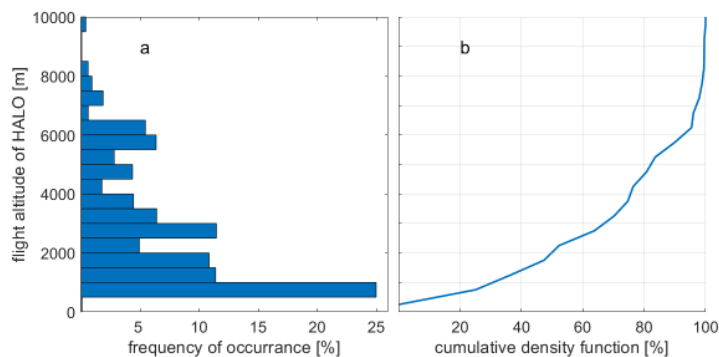




488

489 **Figure 4:** HALO flight tracks during the EMerGe campaign in Europe on 11, 13, 17, 20, 24, 26 and 28 July 2017 (E-EU-03  
490 to E-EU-09, respectively, colour coded). The specific flight times are presented in Table 3. MPC target areas are colour  
491 coded by shading: English Channel (purple) North Sea (red) Benelux/Ruhr (orange), Paris (black), Po Valley (cyan), Central  
492 Italy (blue), East Mediterranean (green). Distinctive locations/regions are marked with red stars, M: Madrid, B: Barcelona, P:  
493 Paris, L: London; BNL: Benelux; Ru: Ruhr area; PV: Po Valley, R: Rome. The coordinates of the MPC areas can be found in  
494 the supplement (S8). The position of the HALO base at DLR in Oberpfaffenhofen (OP) is also indicated by a yellow star for  
495 reference.

496 Overall, 60% of the HALO measurements during EMerGe in Europe were performed below 3000 m to probe  
497 fresh and transported outflows of selected MPCs (see Fig. 5 for the distribution of HALO flight altitudes during  
498 the EMerGe IOP).



499

500 **Figure 5:** Frequency of occurrence of flight altitudes during EMerGe in Europe in bins of 500 m, a) cumulated  
501 frequencies of flight altitudes from the ground to 10000 m b) cumulative density function.

502



503

504 **Table 3:** Characteristics of the HALO flights carried out in Europe during EMeRGe. FR: flight route. Note that E-EU-01 and  
505 E-EU-02 were technical flights and are not considered in the present work.

Flight number	Day/ Month	Start/ End time (UTC)	FR	MPC emission and transport targets	Other features
E-EU-03	11/07	10:00/16:30	1	Rome, Po Valley; convection over Alps and Apennines	Mineral dust from Northern Africa; Fires in Southern Italy. Flights Sky Arrow over Rome
E-EU-04	13/07	10:40/15:00	2	Central Europe; Intercontinental transport	HALO-FAAM blind comparison Canada fires
E-EU-05	17/07	10:30/18:30	2	London, BNL/Ruhr, English Channel and Central Europe	FAAM flights over London PFC tracer release
E-EU-06	20/07	9:00/17:30	1	Rome, Po Valley; Convection over Alps and Apennines	Mineral dust from Northern Africa; Fires in Southern Italy and Croatia
E-EU-07	24/07	9:45/18:15	3	Po Valley, South France, Barcelona; West Mediterranean	Dust transport from Northern Africa, fires in Southern Europe
E-EU-08	26/07	7:45/15:20	2	London, BNL/Ruhr, Paris; English Channel and Central Europe	PFC tracer releases London, Wuppertal
E-EU-09	28/07	10:00/18:30	3	Po Valley, South France, Madrid, Barcelona; West Mediterranean	Fires in Southern France and Portugal

506

507 Different flight routes were selected to optimise the identification and measurement of outflows of target MPCs  
508 under the prevailing meteorological conditions. Taking the measurement objectives, the flight constraints and the  
509 weather conditions into account, three flight routes were selected for the EMeRGe IOP:

- 510 a) Flight route 1: Southern Europe - Italy
- 511 b) Flight route 2: London and Central Europe
- 512 c) Flight route 3: Southwestern Europe

513

514 **a) Flight route 1: Southern Europe- Italy**

515 The flight route 1 was selected for the HALO flights E-EU-03 and E-EU-06 on the 11 and 20 July 2017,  
516 respectively.

517 The synoptic situation in Europe during these days was characterised by a high-pressure system over the  
518 Mediterranean region and a cut-off low over the British Islands associated with the rapid passage of low-pressure  
519 systems over Great Britain and Scandinavia. As a result, a Southwest flow with a trough approaching from the  
520 West and a short wave passage dominated. These conditions were suitable for the investigation of the MPC  
521 targets in Italy (Po Valley and Rome) and of the transport of pollution over the Alps and Apennines.

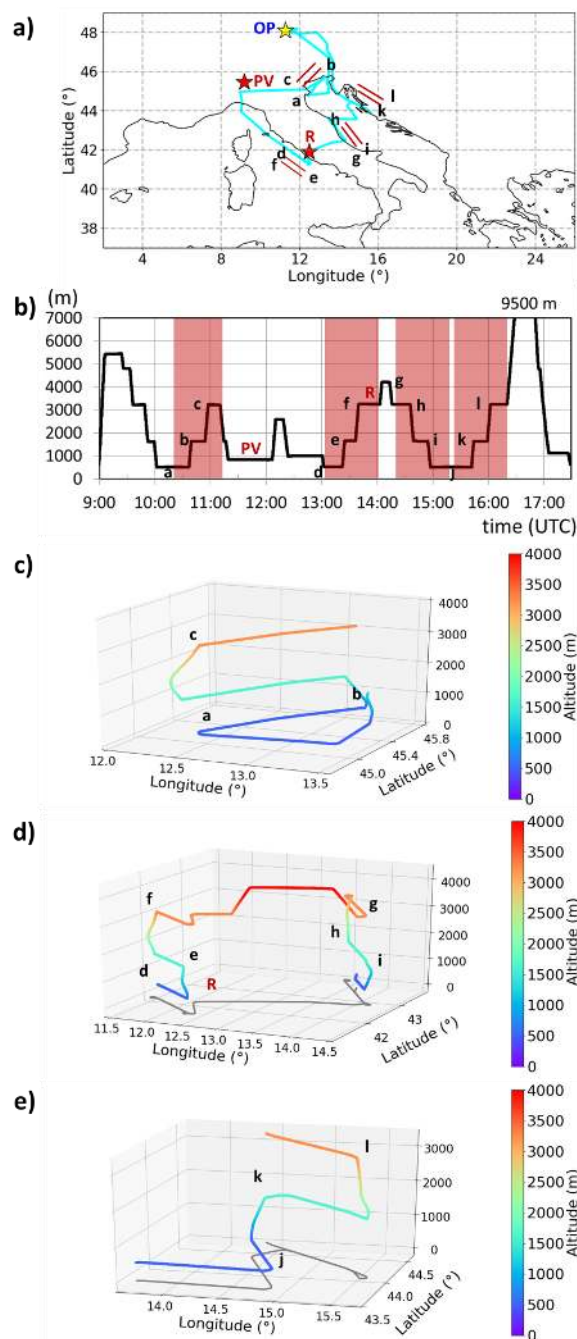
522 Along the flight route, cloud formation in the Po Valley and thunderstorms in Southern Germany in the  
523 afternoon after 15 UTC were observed on both days.

524 During these flights, BB emissions from forest and intentional fires in Southern Italy, particularly in the Naples  
525 area and along the coast of Croatia were detected. In addition, the transport of mineral dust from Northern Africa  
526 to the central Mediterranean and the Italian west coast was observed.

527 The E-EU-03 and E-EU-06 flights were carried out over approximately the same geographical area. Initially  
528 HALO flew over the Alps, then along the Po Valley to the Mediterranean coast of Italy. During E-EU-06 the



529 vertical and horizontal distribution of pollutants was investigated in more detail by shuttles before entering the  
530 Po Valley and flying at lower altitudes. The tracks followed the Tyrrhenian Sea heading to the South and  
531 crossing the Italian Peninsula from West to East towards the Adriatic coast after a shuttle upwind of Rome.  
532 Along the Adriatic coast, shuttles were made while flying to the North. Finally, the flights crossed over the Alps  
533 back to OP. The E-EU-06 flight track details are summarised in Fig. 6.  
534 During E-EU-03 the HALO airborne measurements were complemented by two circuits around Rome by the  
535 Sky Arrow aircraft and its payload, starting at 8 UTC and at 12 UTC, respectively. Each circuit comprised three  
536 vertical spirals from 200 m to 1800 m altitude approximately. In addition, ground-based measurements of trace  
537 gases and aerosol particles are available at selected sites (see S6 in the supplement). The interpretation of these  
538 airborne and ground-based observations is discussed in Barnaba et al. (2021, in preparation).  
539 Whole air samples for VOCs and their carbon isotope ratios were collected at the ground in evacuated canisters  
540 to determine a representative VOC fingerprint for Rome and Milan. To account for emission variations on the  
541 ground during the day, air samples were taken around 9 to 10 and 14 h local time.



542

543 **Figure 6:** Details of the E-EU-06 flight on the 20 July 2017. Three shuttles took place downwind of the Po Valley (PV),  
 544 upwind of Rome (R) and along the Adriatic coast and are marked with red lines on the map in a) as red shaded areas on the  
 545 altitude diagram in b), and as a 3-D depiction in c), d) and e). The flight tracks during the shuttles d) and e) are shown in  
 546 grey. The flight track in a) is coloured as in Fig. 4 and the EMeRGe MPC targets in red. Main changes in course and altitude  
 547 are marked (a-l) on the graphs for reference. OP indicates the position of the HALO base.



548 **b) Flight route 2: London and Central Europe**

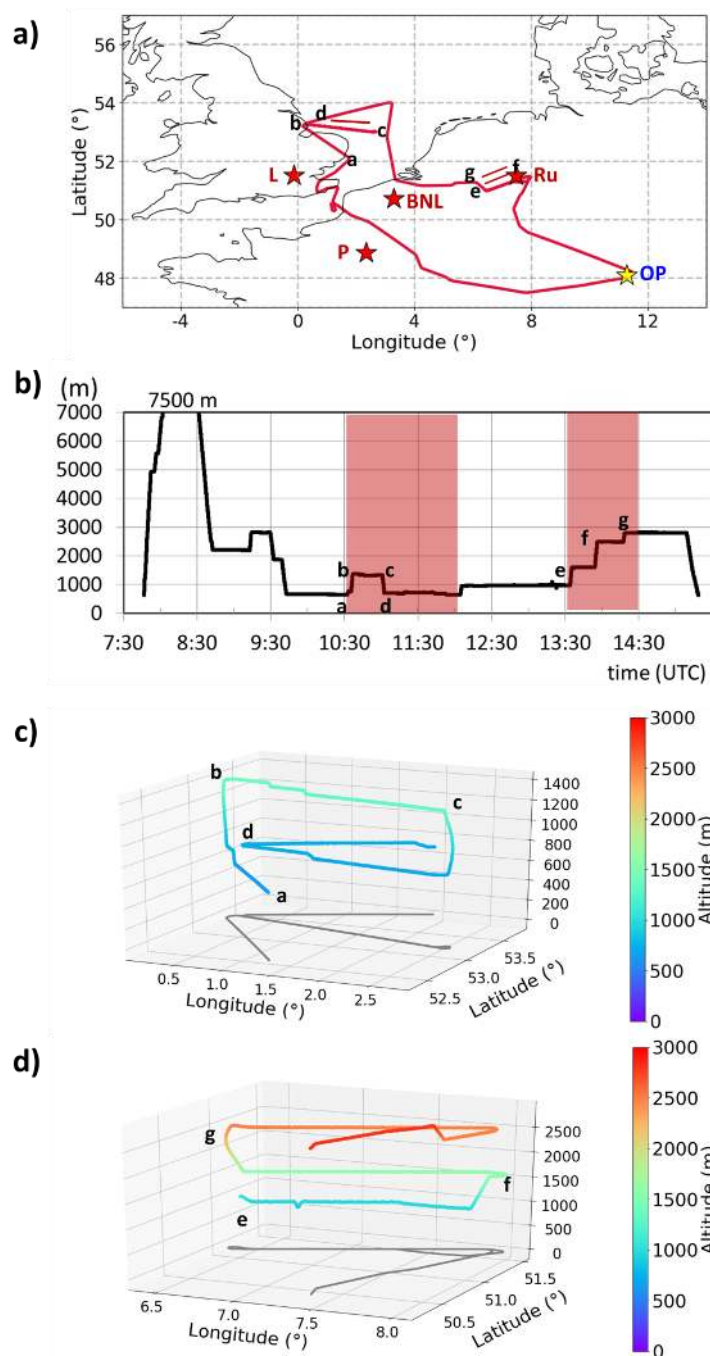
549 Flight route 2 was selected to study the London and BNL/Ruhr outflows with a scientific focus on their transport  
550 and interaction over Central Europe. As mentioned in Sect. 3.1, July 2017 had an unsettled weather in the UK  
551 and Central Europe with heavy, persistent rain at times and only brief hot spells. This made the selection of  
552 optimal flight tracks for this investigation challenging. The precise flight route 2 was tailored for the  
553 meteorological conditions prevailing during the E-EU-05, and E-EU-08 flights, which took place on 17 July and  
554 26 July 2017 respectively, to optimally cover different aspects of the target outflows.

555 The flight E-EU-05 took advantage of a short high-pressure ridge that formed behind a trough over Scandinavia  
556 on 17 July 2017. The outflow of the MPC London was predicted to travel to the English Channel and the  
557 Northern coast of France. This area is regularly used by the UK and French air forces whose activities in the  
558 SUAs constrained the original flight options and the flight track were optimised during the flight route. Over the  
559 area of interest, HALO flew at different altitudes within the PBL. On the way back to OP, the outflow of Paris  
560 was probed South of Orly. On that day, the FAAM platform carried out two complementary circuits around  
561 London at 8:00 and 13:30 UTC.

562 On 26 July 2017, the synoptic situation changed slightly as a cut-off low moved eastwards over Germany while  
563 a trough approached from the West. In the period after the cut-off low and before the passage of the warm front  
564 over London, the route of E-EU-08 was chosen such that the outflow of London close to the East coast of  
565 England and its mixing with the BNL/Ruhr outflow over the European continent were probed (see Fig. 7).  
566 Cloudy conditions predominated throughout the day. This flight is studied in more detail in Sect. 4.2.

567 The identification of the London outflow was confirmed by the on-board measurement of a PFC tracer released  
568 in the centre of London for both flights. During E-EU-08, a second tracer release was carried out in Wuppertal in  
569 the afternoon to identify the BNL/Ruhr outflow. In addition, information on the isotopic fingerprints in VOCs  
570 representative for London and Ruhr MPC air were obtained by collecting whole air samples at the tracer release  
571 sites before, during and after the release, and in the afternoon (see Sect. 4.2.).

572 The E-EU-04 flight track on 13 July 2017 is a particular case that also covered Central Europe (see S9 in the  
573 supplement). The first part of the flight was dedicated to the blind instrumental intercomparison between the  
574 HALO and FAAM platforms described in 2.4.3 (see Schumann, 2020). A weak high-pressure ridge over  
575 Germany dominated. The main objective for the rest of the flight was to probe intercontinental pollution  
576 transport between 5000 and 7000 m altitude with signatures of fires originating in Canada.



577

578 **Figure 7:** Details of the E-EU-08 flight on the 26 July 2017. The position of the shuttles downwind from London and the  
 579 BNL/Ruhr area are indicated in red on the map in a), marked by the red shaded areas in b), and as a 3-D depiction in c) and  
 580 d). The flight tracks during the shuttles are shown in c) and d) in grey. In a) the EMerGe MPC targets are shown in red and  
 581 the flight track coloured as in Fig. 4. Main changes in course and altitude are marked (a-g) on the graphs for reference. OP  
 582 indicates the position of the HALO base.



583 **c) Flight route 3: Southwestern Europe**

584 The objective of flight route 3 was to investigate the transport of Southern European MPC outflows into the  
585 Western Mediterranean. This flight route was selected for the E-EU-07 and E-EU-09 flights on the 24 and 28  
586 July 2017, respectively.

587 The meteorological situation on 24 July 2017 over Europe was characterised by the eastwards displacement of a  
588 cut-off low leaving the British Islands. This was associated with a Southwest flow during the passage of a trough  
589 over Spain and France. Dust transport from Northern Africa, thunderstorms in the Po Valley and fires in the  
590 South Mediterranean coast of France and Corsica prevailed. The E-EU-07 flight track crossed the Po Valley and  
591 focused on the measurement of the predicted outflow of pollution from Southern France and Barcelona into the  
592 Mediterranean. Three shuttle flight patterns downwind from Marseille, Barcelona and close to the western coast  
593 of Sardinia were carried out (see S9 in the supplement).

594 On 28 July 2017, a short wave trough with a weak cold front passed over France. This situation led to a  
595 prevailing westerly flow and suitable conditions for the E-EU-09 flight over Southern Europe. Two shuttle flight  
596 patterns were carried out downwind of Marseille and Barcelona. Features of interest during this flight were the  
597 transport of the Madrid and Barcelona outflows in stratified layers into the Mediterranean and the transport of  
598 forest fire emissions originating in Southern France and Portugal. This is described in more detail in 4.3.2.

599 Further details on all the flight tracks and shuttles are given in the supplement (S9).

600 **3.4 Model predicted pollution transport patterns**

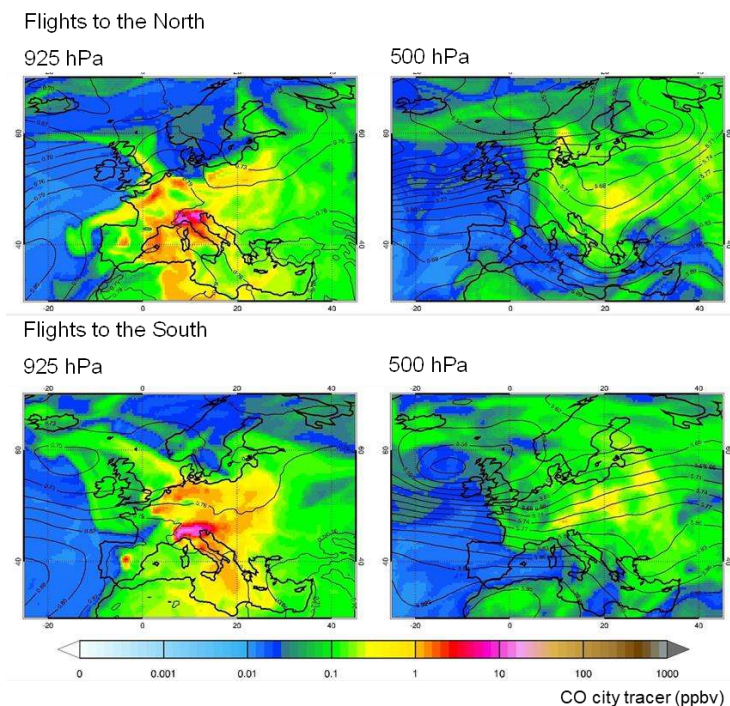
601 CAMS global model data (see S3 for the model description) were used to evaluate characteristic pollution  
602 transport patterns during the EMERGE IOP over Europe. CAMS operational near-real time (NRT) simulations  
603 with full emissions and chemistry were incorporated in the analysis. A stratospheric O<sub>3</sub> tracer as a proxy for  
604 stratospheric-tropospheric transport was also used. In addition, passive CO tracers (i.e., no chemical loss or  
605 production) provided through the CAMS field campaign support (<https://atmosphere.copernicus.eu/scientific-field-campaign-support>) were used with either a) only emissions from EMERGE target cities switched on in the  
606 simulations (CO city tracer), or b) only BB emissions switched on in the simulations.

607  
608 Figures 8, 10 and 11 show composite average maps of 12 h CAMS-global forecast for the EMERGE flights to the  
609 North (Flight route 2: E-EU-05 and E-EU-08) and to the South of Europe (Flight routes 1 and 3: E-EU-03, E-  
610 EU-06, E-EU-07, and E-EU-09; see Fig.4 and Table 3 for description). The model was initialised at 00 UTC, for  
611 the forecast at 12:00 UTC. The CO city tracer simulations at 500 and 925 hPa (see Fig. 8) indicate that the  
612 anthropogenic MPC emissions remained close to the surface within the PBL. The emissions from the MPCs in  
613 the North (e.g. London, Paris) are expected to be frequently transported eastwards due to the dominant west-  
614 southwesterly winds. In contrast, emissions from MPCs South of the polar front, such as Madrid, spread in all  
615 directions due to variable weak winds. In the highly polluted Po Valley, the emissions were transported to the  
616 Northeast and lifted over the high mountains of the Alps.

617 Higher temperatures and dry conditions in Southern Europe during the EMERGE IOP favoured O<sub>3</sub> production  
618 and smog events. This was the case for flights to the South of Europe, as indicated by the simulations at 925 hPa  
619 (see Fig. 8 and Fig. 11). These meteorological conditions supported the propagation of multiple and mostly  
620 intentionally started fires in the Mediterranean area. Figure 9 shows average fire radiative power observed by  
621 MODIS (MODerate resolution Imaging Spectroradiometer, <http://modis-fire.umd.edu/>) and assimilated within  
622 CAMS-global over Europe in July 2017. In the target area, fire hot spots are visible around the Mediterranean



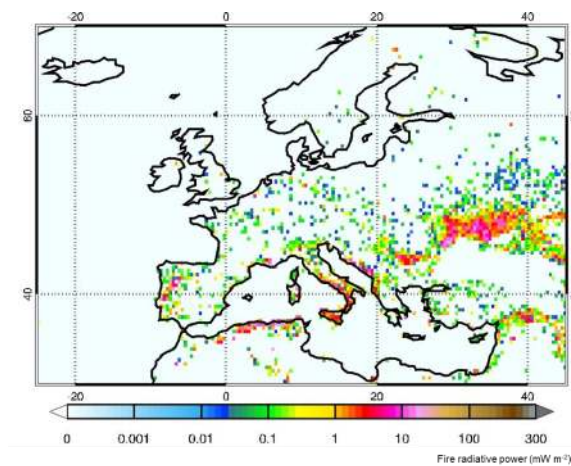
623 (e.g., Southern Italian Peninsula, Sicily, Sardinia, Croatia, France around Marseille, North Africa) and in  
624 Portugal.  
625 Further evaluation of the CAMS simulations shows that CO emitted by fires around the Mediterranean mainly  
626 remained at altitudes below approximately 700 hPa. In contrast, CO resulting from the LRT of North American  
627 fire emissions was observed around 500-700 hPa over Europe. The average fields show that CO from North  
628 American fires was expected to be more pronounced during flights to the North (see Fig. 10), than to the South  
629 (see Fig.11) with a maximum in the average fields over Great Britain.  
630 The stratospheric O<sub>3</sub> tracer indicates that stratospheric intrusions over the flight domain during the campaign  
631 concurred with the LRT of North American fire emissions initially lofted by warm conveyor belts or deep  
632 convection. The LRT of fire emissions towards Europe is associated with mid-latitude cyclones crossing the  
633 Atlantic. Dry air masses rich in O<sub>3</sub> were then transported downwards to comparably low altitudes. In the average  
634 fields of stratospheric O<sub>3</sub> for flights towards the North (see Fig. 10, lower right panel), the stratospheric intrusion  
635 over Europe stretches broadly from Southern Greece and Southern Italy to the Northeast. The latter is associated  
636 with the cut-off low which developed on 20 July 2017 over UK and started to move eastwards on 26 July 2017.  
637



638

639 **Figure 8:** Coloured shadings of composite averages of CAMS-global city tracer forecasts of CO  
640 (ppbv) at 12:00 UTC for days of flights to the North ((E-EU-05, E-EU-08, top) and South (E-EU-  
641 03, E-EU-06, E-EU-07, E-EU-09, bottom) of Europe. Black contours show corresponding averages  
642 of geopotential height (km) from the ECMWF-Integrated Forecasting System (IFS).

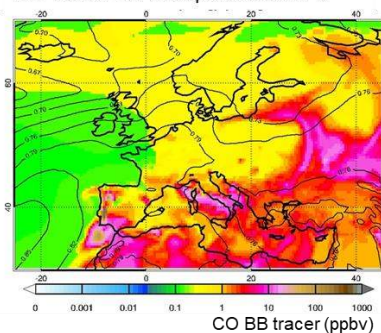




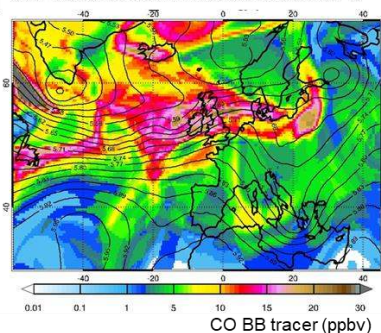
643  
 644 **Figure 9:** Average fire radiative power ( $\text{mW m}^{-2}$ ) as observed by MODIS over Europe in July 2017. Data  
 645 from the CAMS Global fire assimilation system (GFAS). <https://www.ecmwf.int/en/forecasts/dataset/global-fire-assimilation-system-gfas>  
 646 fire emission database (Kaiser et al., 2012).  
 647

Flights to the North

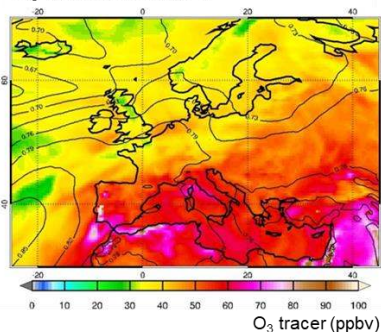
CO tracer BB Europe at 925 hPa



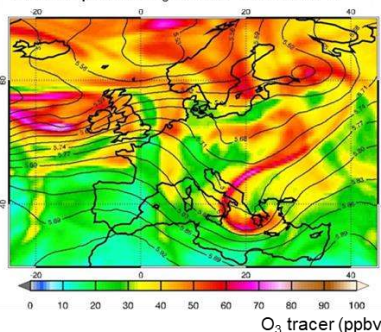
CO tracer BB N. America at 925 hPa



O<sub>3</sub> tracer at 925 hPa

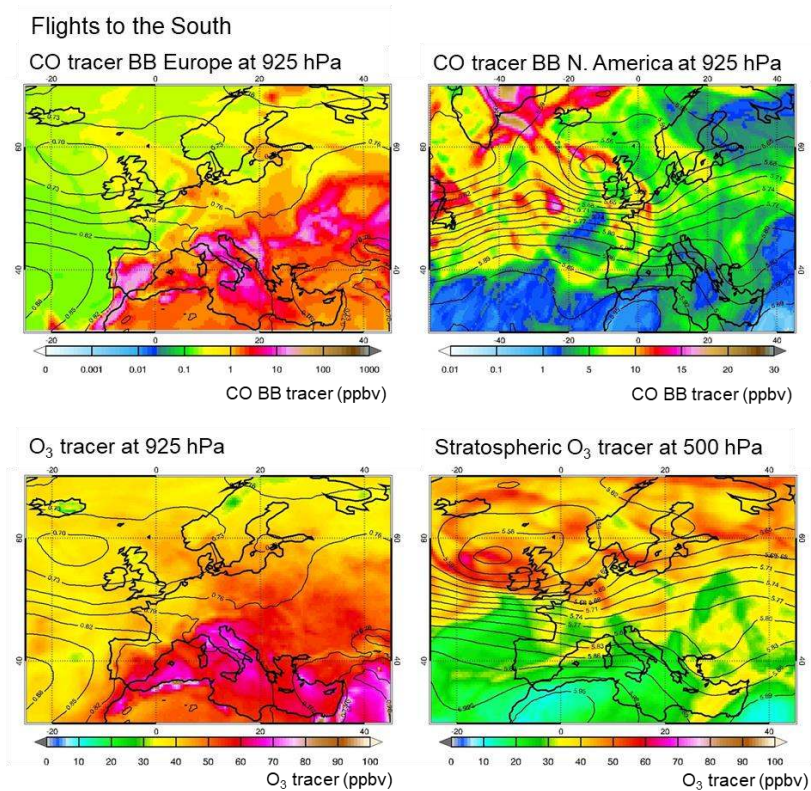


Stratospheric O<sub>3</sub> tracer at 500 hPa



648

649 **Figure 10:** Coloured shadings of composite averages of CAMS-global forecasts at 12:00 UTC for  
 650 flights to the North (E-EU-05, E-EU-08): BB CO tracer (ppbv) from Europe (top left), and from  
 651 North America (top right) at 925 hPa; O<sub>3</sub> (ppbv) at 925 hPa (bottom left), and stratospheric ozone  
 652 tracer (ppbv) at 500 hPa (bottom right). Black contours show averages of geopotential height (km)  
 653 from ECMWF-IFS. Note the different scales. The BB tracer from North America is shown on a  
 654 larger map than the other CAMS forecasts in this image.



655

656

657

**Figure 11:** Coloured shadings of composite averages of CAMS-global forecasts as in Fig.10, for flights to the South (E-EU-03, E-EU-06, E-EU-07 and E-EU-09).

658



659 **3.5 Measured amount and distribution of trace gases and aerosol particles**

660 The chemical composition and the extent of photochemical activity of the air masses probed during the EMeRGe  
 661 IOP were different for the different flight routes and tracks. This is to be expected as a result of the large  
 662 geographical coverage of the flights, the different solar insolation conditions and the flight path of the air masses,  
 663 the heterogeneous topography and the proximity of pollution sources of different types.

664 Table 4 shows the average, median and quartiles values of selected species measured during E-EU-08 and E-EU-  
 665 06 as examples of flights in Northern and Southern Europe, respectively. The mean values and variability of  
 666 most of the species are of the same order of magnitude in both flights and generally higher for E-EU-06 below  
 667 2000 m except for NO. Higher temperatures and insolation in the South are associated with higher O<sub>3</sub> and RO<sub>2</sub><sup>\*</sup>  
 668 as for example observed in E-EU-06 below 2000 m. The higher SO<sub>2</sub> and CH<sub>3</sub>CN mean values are associated to  
 669 the plumes measured in the Po Valley and to the fires dominating in the South during the IOP, respectively. The  
 670 average concentrations measured for the rest of the EMeRGe flights are included in the supplement (S10).

671

672 **Table 4:** Mean concentrations (mean), median (med) and quartiles (25<sup>th</sup> 75<sup>th</sup>) of selected measured trace gases and aerosol  
 673 particles for E-EU-08 and E-EU-06 as examples of flights in Northern and Southern Europe. n.a. non-available <sup>x</sup>HCHO:  
 674 HCHO from PTRMS measurements; <sup>h</sup>HCHO: HCHO from miniDOAS measurements; N<sub>CN</sub>: N<sub>D>250nm</sub> particle with D > 10  
 675 nm, and D > 250 nm, respectively (inlet cut-off 1.5 to 3 μm depending on height); BCm: black carbon mass concentration;  
 676 BCn: black carbon number concentration; OA: Organic aerosol. Note that CN, N<sub>D</sub>, BCm, BCn, OA, NO<sub>3</sub><sup>-</sup>, SO<sub>4</sub><sup>2-</sup>, NH<sub>4</sub><sup>+</sup> and  
 677 Cl<sup>-</sup> are given for standard temperature and pressure conditions.

E-EU-08 species	<2000 m				2000-4000 m				>4000 m				Unit
	mean	med	25 <sup>th</sup>	75 <sup>th</sup>	mean	med	25 <sup>th</sup>	75 <sup>th</sup>	mean	med	25 <sup>th</sup>	75 <sup>th</sup>	
O <sub>3</sub>	43	45	37	49	51	53	49	55	64	63	56	73	ppbV
CO	98	96	92	102	90	91	85	93	94	93	92	96	ppbV
NO	407	225	155	450	138	77	60	108	109	102	82	131	pptV
NO <sub>y</sub>	3734	3039	2075	4018	1991	1302	720	1777	4619	3765	2652	5761	pptV
HONO	n.a.	n.a.	n.a.	n.a.	n.a.	n.a.	n.a.	n.a.	n.a.	n.a.	n.a.	n.a.	pptV
NO <sub>2</sub>	n.a.	n.a.	n.a.	n.a.	n.a.	n.a.	n.a.	n.a.	n.a.	n.a.	n.a.	n.a.	pptV
<sup>*</sup> HCHO	n.a.	n.a.	n.a.	n.a.	n.a.	n.a.	n.a.	n.a.	n.a.	n.a.	n.a.	n.a.	pptV
RO <sub>2</sub> <sup>*</sup>	20	21	10	29	31	28	21	37	19	13	0	35	pptV
SO <sub>2</sub>	193	99	68	169	55	54	43	64	55	52	38	68	pptV
N <sub>CN</sub>	4514	3186	2066	4551	1041	790	582	1245	2900	1635	728	3935	cm <sup>-3</sup>
N <sub>D&gt;250nm</sub>	119.2	111.5	61.1	161.1	18.2	12.3	6.2	21.8	7.7	4.4	2.3	9.2	cm <sup>-3</sup>
BCm	0.14	0.12	0.07	0.18	0.02	0.01	0.01	0.03	0.01	0.00	0.00	0.01	μg m <sup>-3</sup>
BCn	71	68	42	92	10	8	4	13	4	3	2	6	cm <sup>-3</sup>
OA	1.80	1.88	1.21	2.37	0.58	0.51	0.34	0.71	0.49	0.50	0.36	0.63	μg m <sup>-3</sup>
NO <sub>3</sub> <sup>-</sup>	1.21	0.96	0.60	1.68	0.10	0.07	0.05	0.11	0.07	0.06	0.05	0.08	μg m <sup>-3</sup>
SO <sub>4</sub> <sup>2-</sup>	0.85	0.73	0.56	0.97	0.20	0.18	0.13	0.23	0.09	0.09	0.07	0.11	μg m <sup>-3</sup>
NH <sub>4</sub> <sup>+</sup>	0.80	0.65	0.46	1.08	0.16	0.13	0.10	0.19	n.a.	n.a.	n.a.	n.a.	μg m <sup>-3</sup>
Cl <sup>-</sup>	0.09	0.08	0.05	0.12	0.03	0.02	0.01	0.03	0.03	0.03	0.02	0.03	μg m <sup>-3</sup>
C <sub>3</sub> H <sub>6</sub> O	1517	1543	1347	1705	1384	1404	1312	1495	1602	1614	1534	1707	pptV
CH <sub>3</sub> CN	94	95	80	106	130	126	113	140	130	131	116	147	pptV
C <sub>5</sub> H <sub>8</sub>	80	68	56	89	61	57	50	65	69	65	56	71	pptV
C <sub>6</sub> H <sub>6</sub>	64	63	47	78	33	29	25	36	30	27	24	38	pptV
C <sub>7</sub> H <sub>8</sub>	45	35	25	55	29	24	18	33	22	19	17	24	pptV
<sup>x</sup> HCHO	1234	1165	937	1461	642	637	538	733	411	407	290	496	pptV
C <sub>2</sub> H <sub>2</sub> O <sub>2</sub>	n.a.	n.a.	n.a.	n.a.	n.a.	n.a.	n.a.	n.a.	n.a.	n.a.	n.a.	n.a.	pptV
C <sub>3</sub> H <sub>4</sub> O <sub>2</sub>	n.a.	n.a.	n.a.	n.a.	n.a.	n.a.	n.a.	n.a.	n.a.	n.a.	n.a.	n.a.	pptV

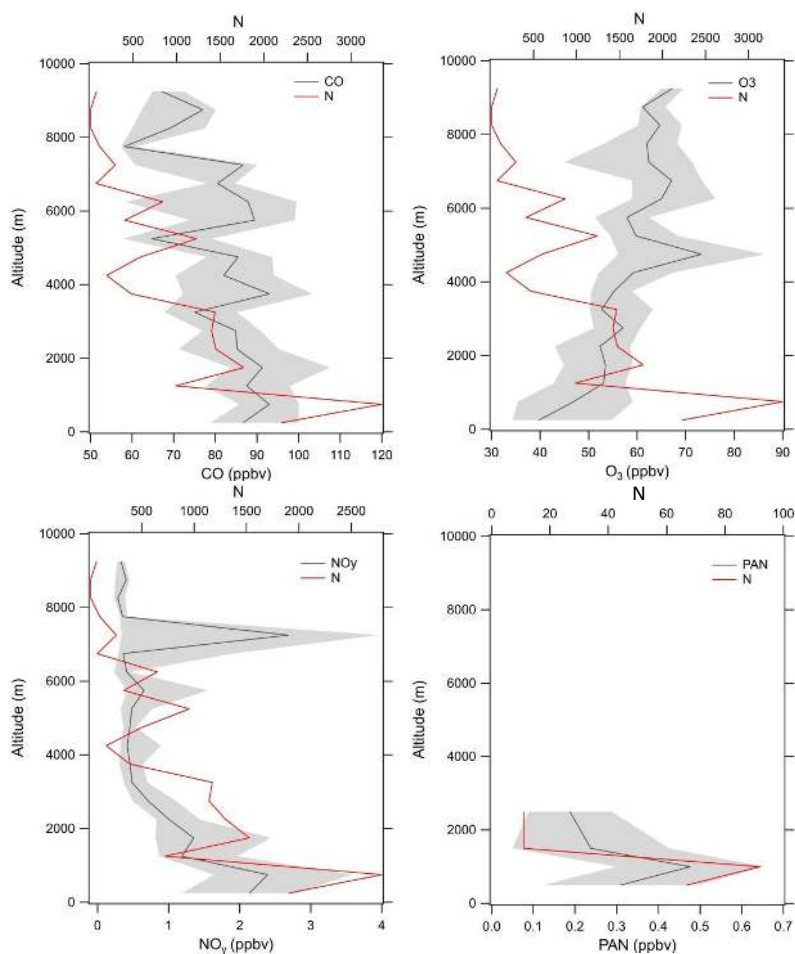
678



E-EU-06 species	<2000 m				2000-4000 m				>4000 m				Unit
	mean	med	25 <sup>th</sup>	75 <sup>th</sup>	mean	med	25 <sup>th</sup>	75 <sup>th</sup>	mean	med	25 <sup>th</sup>	75 <sup>th</sup>	
O <sub>3</sub>	69	71	58	77	52	51	50	52	58	56	53	64	ppbV
CO	111	113	94	125	78	77	73	81	77	78	70	82	ppbV
NO	189	123	84	205	71	56	47	66	483	42	23	136	pptV
NO <sub>y</sub>	3321	2542	1701	4104	737	581	465	939	2006	366	283	490	pptV
HONO	15	13	0	27	3	0	0	9	0	0	0	0	pptV
NO <sub>2</sub>	454	378	238	531	169	174	115	199	191	172	43	303	pptV
*HCHO	1408	1219	996	1731	709	690	627	748	588	597	580	599	pptV
RO <sub>2</sub> <sup>*</sup>	49	52	36	63	41	44	30	53	31	38	16	44	pptV
SO <sub>2</sub>	673	514	289	877	136	131	113	152	120	85	73	100	pptV
NCN	6136	2943	2052	4823	1493	1291	1147	1496	914	803	603	1185	cm <sup>-3</sup>
NO <sub>&gt;250nm</sub>	174.2	150	85.8	224.3	49	48.5	41.1	54.9	22.2	16.3	7	30.7	cm <sup>-3</sup>
BCm	0.30	0.28	0.14	0.40	0.09	0.07	0.05	0.10	0.04	0.02	0.01	0.04	µg m <sup>-3</sup>
BCn	127	127	65	176	34	33	28	39	11	7	4	18	cm <sup>-3</sup>
OA	3.12	3.25	2.02	3.92	1.07	1.00	0.73	1.32	0.45	0.34	0.28	0.51	µg m <sup>-3</sup>
NO <sub>3</sub> <sup>-</sup>	0.69	0.15	0.09	0.62	0.07	0.06	0.05	0.08	0.07	0.05	0.04	0.08	µg m <sup>-3</sup>
SO <sub>4</sub> <sup>2-</sup>	1.64	1.49	0.98	1.93	0.59	0.61	0.55	0.68	0.27	0.20	0.11	0.44	µg m <sup>-3</sup>
NH <sub>4</sub> <sup>+</sup>	0.82	0.67	0.46	1.04	0.28	0.29	0.24	0.32	0.17	0.17	0.09	0.22	µg m <sup>-3</sup>
Cl <sup>-</sup>	0.04	0.04	0.02	0.05	0.02	0.02	0.01	0.02	0.03	0.03	0.03	0.03	µg m <sup>-3</sup>
C <sub>3</sub> H <sub>6</sub> O	2444	2434	1935	2937	1645	1656	1514	1799	1476	1452	1316	1605	pptV
CH <sub>3</sub> CN	140	131	115	152	129	131	118	138	135	132	123	145	pptV
C <sub>5</sub> H <sub>8</sub>	98	78	59	112	62	57	50	64	73	67	55	83	pptV
C <sub>6</sub> H <sub>6</sub>	109	94	56	152	36	34	25	41	32	30	22	37	pptV
C <sub>7</sub> H <sub>8</sub>	57	42	25	77	35	25	22	51	32	30	26	37	pptV
*HCHO	1843	1651	1088	2374	891	875	748	993	641	616	491	782	pptV
C <sub>2</sub> H <sub>2</sub> O <sub>2</sub>	220	192	132	276	182	103	49	260	101	63	8	111	pptV
C <sub>3</sub> H <sub>4</sub> O <sub>2</sub>	1496	1275	1075	1577	1351	790	574	1622	817	571	296	756	pptV

679

680 The transport, transformation and radiative impact of pollutants depend on their vertical distribution. During the  
 681 EMerGe IOP the maximum concentrations of trace gases and aerosol species were typically measured below  
 682 2000 m. Figure 12 shows the vertical distribution of CO, O<sub>3</sub>, NO<sub>y</sub> and PAN mixing ratios for all HALO  
 683 observations made during the EMerGe IOP, averaged over altitude bins of 500 m. CO, total reactive nitrogen  
 684 (NO<sub>y</sub>) and its most reactive forms NO and NO<sub>2</sub>, are key species in the identification of anthropogenic pollution.  
 685 During daylight, NO and NO<sub>2</sub> are typically in or close to a photostationary state that is established in the order of  
 686 minutes. Further photochemical reactions convert NO and NO<sub>2</sub> into longer lived reservoirs such as PAN or  
 687 HNO<sub>3</sub>. PAN has major implications for the global distributions of O<sub>3</sub> and OH as it can release NO<sub>2</sub> at higher  
 688 tropospheric temperatures far from the sources of pollution (e.g. Fischer et al., 2014). On average, changes of  
 689 CO with altitude were not pronounced except below 2000 m and above 8000 m. This is consistent with the  
 690 relatively long lifetime of CO and a well-mixed troposphere in summer. As the lifetime of NO<sub>y</sub> is much shorter  
 691 than that of CO, the distance from the source has a stronger influence on NO<sub>y</sub> than on CO observations. NO<sub>y</sub>  
 692 shows a pronounced height dependence and variability which is reflected in the large standard deviations and the  
 693 differences between mean and median values (not shown). The PAN measurements made up to 3000 m altitude  
 694 have a similar behaviour. The high NO<sub>x</sub>/NO<sub>y</sub> ratios occasionally observed at high altitudes are attributed to NO<sub>x</sub>  
 695 production by lightning and more rapid transport.



696

697

698 **Figure 12:** Variation of CO, O<sub>3</sub>, NO<sub>y</sub> and PAN volume mixing ratios versus altitude during EMerGe over Europe. Solid  
699 lines represent the medians averaged over altitude bins of 500 m and the shaded areas are the quartiles. The number of  
700 measuring points (N) is shown in red.

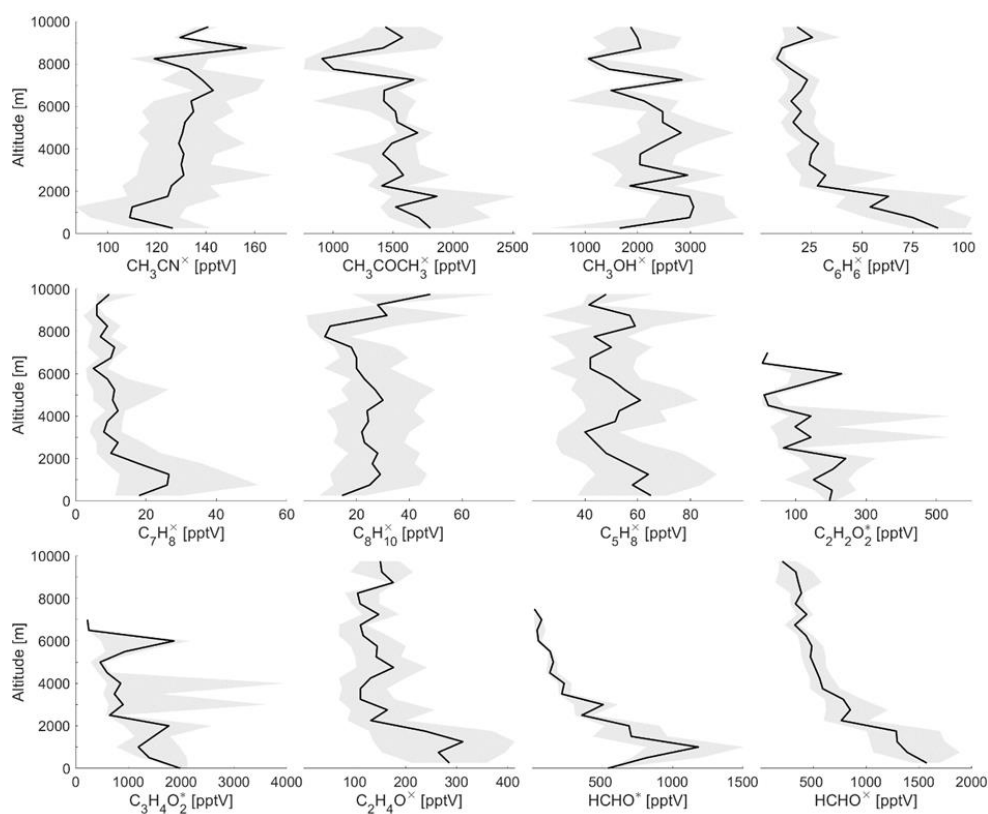
701 Figure 13 shows median vertical distributions of major primary and secondary VOCs observed during the  
702 EMerGe IOP in Europe. Longer lived VOCs were well mixed in the troposphere and those with anthropogenic  
703 sources showed higher variability and highest mixing ratios below 2000 m. HCHO and acetaldehyde (C<sub>2</sub>H<sub>4</sub>O)  
704 have anthropogenic BB and significant biogenic sources. They are also generated downwind by the oxidation of  
705 transported VOCs. In contrast, benzene (C<sub>6</sub>H<sub>6</sub>) and toluene (C<sub>7</sub>H<sub>8</sub>) are primarily of anthropogenic origin. These  
706 species have a short lifetime as they are oxidised quickly in the lower layers of the troposphere. As a result, the  
707 concentrations observed above 2000 m were close to the instrumental limit of detection. The same is true for  
708 isoprene (C<sub>5</sub>H<sub>8</sub>) and xylene (C<sub>8</sub>H<sub>10</sub>) which have lifetimes in the order of some hours.

709 Acetonitrile (CH<sub>3</sub>CN) and acetone (CH<sub>3</sub>COCH<sub>3</sub>) are typically well mixed in the troposphere due to their longer  
710 lifetimes, which are in the order of months. As a recognised tracer for BB, the increase of median CH<sub>3</sub>CN with  
711 altitude identifies the LRT of BB emissions from North America and the local transport of BB events in Europe.



712 The averaged vertical distribution of methanol ( $\text{CH}_3\text{OH}$ ), having  $\sim 12$  days lifetime, might result from the  
713 convective mixing of a variety of ground sources which in the summer are largely of biogenic origin.  
714 Known sources of glyoxal ( $\text{C}_2\text{H}_2\text{O}_2$ ) and methylglyoxal ( $\text{C}_3\text{H}_4\text{O}_2$ ) are the oxidation of  $\text{C}_3\text{H}_8$  and BB.  $\text{C}_2\text{H}_2\text{O}_2$  is  
715 also an oxidation product of acetylene ( $\text{C}_2\text{H}_2$ ) which is of anthropogenic origin.  $\text{C}_3\text{H}_4\text{O}_2$  is produced in the  
716 oxidation of  $\text{CH}_3\text{COCH}_3$ , which is thought to have a dominant biogenic source (Andreae, 2019; Wennberg et al.,  
717 2018). Both gases are also formed during the oxidation of other VOCs, particularly alkenes, aromatics, and  
718 monoterpenes (Myriokefalitakis et al., 2008; Fu et al., 2008; Taraborrelli et al., 2020) and are present both as  
719 primary or secondary pollutants during BB events (e.g., Vrekoussis et al., 2009; Alvarado et al., 2020).

720



721

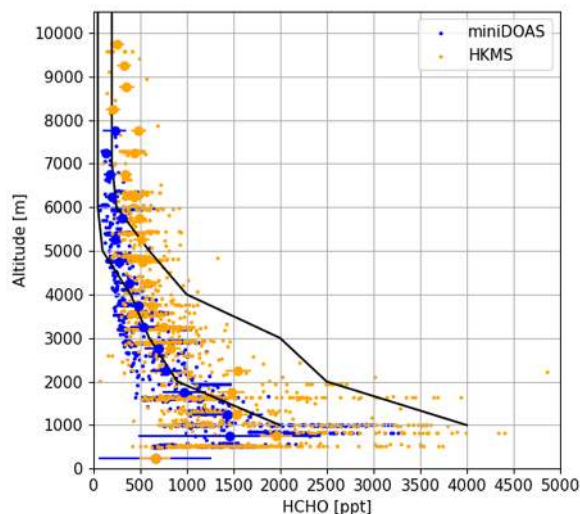
722 **Figure 13:** Variation of VOC versus altitude measured by the HKMS (labeled with  $\times$ ) and the miniDOAS (labeled with  $\ast$ )  
723 instruments during EMERGe over Europe. Shaded areas are the quartiles, solid lines represent median concentrations.

724 The HCHO mixing ratios measured by the in-situ PTRMS (HKMS) and the remote sensing miniDOAS  
725 instruments during the IOP in Europe are consistent with previous remote sensing observations over South East  
726 Asia (Burrows et al., 1999) and North America in summer (Kluge et al., 2020; Chance et al., 2000; Dufour et al.,  
727 2009; Boeke et al. 2011; De Smedt et al., 2015; Kaiser et al., 2015; Chan Miller et al., 2017, and references  
728 therein). They are also in the same range as those measured in the Po Valley (Heckel et al., 2005).

729 The HCHO mixing ratios observed in the PBL and middle troposphere during EMERGe are somewhat lower  
730 than the North American mixing ratios (see Fig. 14). This might be related to the fact that several EMERGe flight  
731 tracks were carried out far from emission sources over the North and the Mediterranean Seas. In addition, the



732 emissions of HCHO and its VOC precursors have been reported in previous studies to be lower in Europe than in  
733 North America (e.g. Dufour et al., 2009; De Smedt et al., 2015).  
734



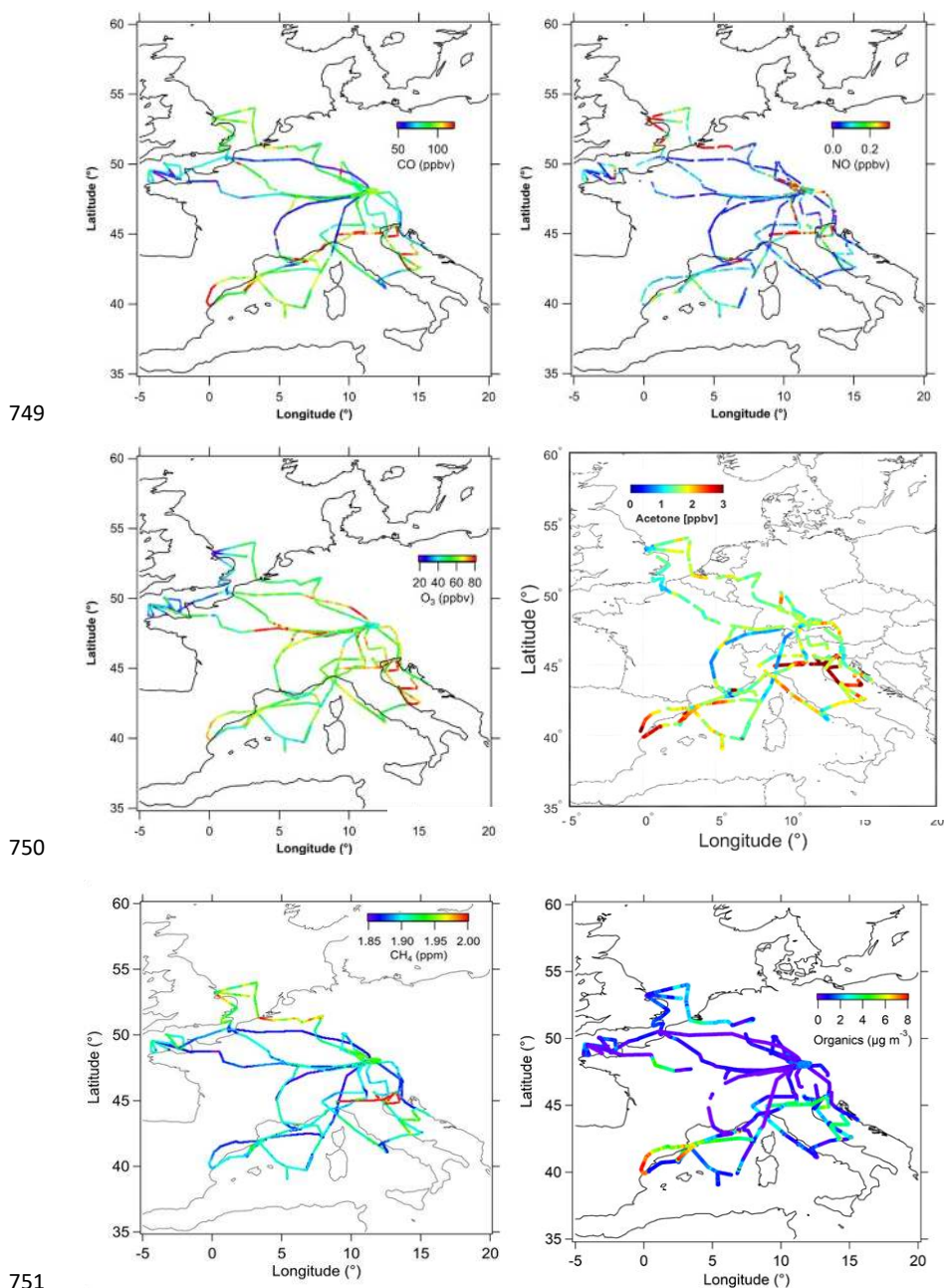
735

736 **Figure 14:** HCHO measurements by the HKMS (in orange) and the miniDOAS instruments (in blue). Mean values  
737 (bigger dots) and the respective accuracies (horizontal bars) are also shown. The black lines indicate the range of  
738 previous HCHO measurements over North America in summer (Kluge et al., 2020). Note that HKMS and miniDOAS  
739 agree within their accuracies in spite of having different air sampling volumes, which did not perfectly overlap.

740 The vertical profiles shown in Fig. 14 are averages from the measurements taken along all flights at variable  
741 distances from various source regions and under different meteorological conditions. In a next step, pollution  
742 hotspots are identified by using the spatial distribution of trace gases and aerosol particles observed over the  
743 flight tracks.

744 Figure 15 shows as an example the CO, NO, O<sub>3</sub>, CH<sub>3</sub>COCH<sub>3</sub>, CH<sub>4</sub>, and the organic aerosol mass concentrations  
745 measured during the EMeRGe flights in Europe. A detailed analysis of the complexity of the air masses  
746 measured and the variations encountered in individual flights is beyond the scope of the present work and will be  
747 presented in dedicated publications.

748



752 **Figure 15:** Mixing ratios of CO NO<sub>x</sub> O<sub>3</sub> CH<sub>3</sub>COCH<sub>3</sub> CH<sub>4</sub> and organic aerosol mass concentrations measured along all  
753 EMeRGe flights in Europe. To increase colour contrast, 50 ppbv has been set as lower limit for CO, and 0.5 ppbv and 80  
754 ppbv as upper limit for NO and O<sub>3</sub> respectively. These limits are representative for more than 95% of all measurements. CH<sub>4</sub>  
755 mixing ratios are in 0.05 x 0.05° bins as in Klausner (2020). Organic aerosol mass concentrations are plotted for the original  
756 time resolution of 30 sec. Note that mixing ratios measured at different altitudes in the shuttle areas are not distinguishable in  
757 the figure.

758 During the EMeRGe IOP in Europe, the highest NO concentrations were found in the vicinity and downwind of  
759 major pollution sources like London, the BNL/Ruhr region and the Po Valley. High NO concentrations are



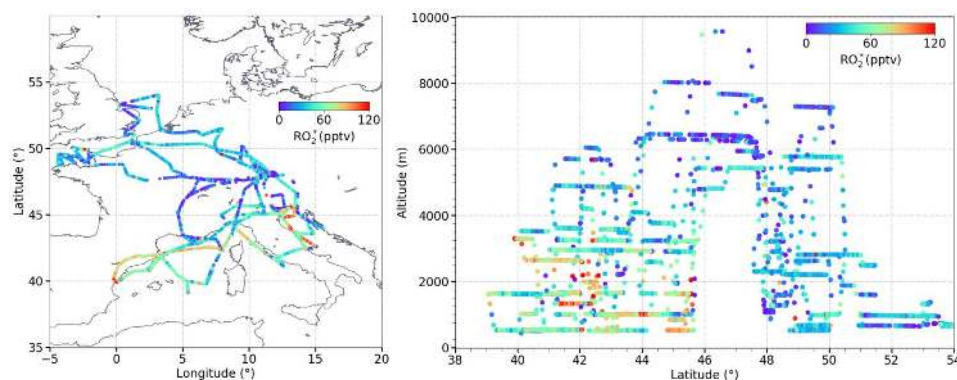


760 indicative of recent or “fresh” anthropogenic emissions. The  $\text{NO}_y$  lifetime of a few days enables a more reliable  
761 identification of aged polluted air masses further out from the source regions. Maximum  $\text{NO}_y$  values as large as  
762 12 ppbv were measured. Elevated CO and  $\text{NO}_y$  accompanied by low NO, as measured in the proximity of  
763 Barcelona, indicate that there has been a significant amount of processing of the pollution plumes sampled.  
764 Emission hot-spots can be hardly identified in the spatial distribution of  $\text{O}_3$  as expected from its non-linear  
765 secondary formation. Maximum  $\text{O}_3$  mixing ratios were generally observed at a distance downwind of MPCs,  
766 determined by  $\text{O}_3$  production and loss in the plumes.

767 Organic aerosol has strong anthropogenic sources such as combustion (traffic, fossil fuel combustion, BB) and  
768 industrial activity, and shows similar behaviour to CO and NO, in that larger mass concentrations are closer in  
769 time and space to MPCs such as London, Po Valley, and BNL. The lifetime of aerosol particles in the PBL is a  
770 few days, which explains the high variability observed. Additionally, aerosol particle concentrations have a  
771 strong gradient above the PBL (see Sect. 4.1). As a result, the flight shuttles at different altitudes have large  
772 variability in the horizontal distribution.

773 The highest and most distinctive  $\text{CH}_4$  mixing ratios in the PBL were likewise encountered in the Po Valley (up to  
774 2.4 ppm), downwind of London and across the BNL/Ruhr region (up to 2 ppm). Slightly lower mixing ratios  
775 were detected downwind of Barcelona (up to 1.94 ppm). The mixing ratios were higher than the global mean  
776 ground level mixing ratio of around 1.85 ppm for July 2017. The emission plume signatures were generally more  
777 evident when shuttles were performed close to the respective MPC regions. At large downwind distances the  
778  $\text{CH}_4$  emissions are diluted and/or mixed with pollution from surrounding sources. For the assignment of the  
779 GHG enhancements to their source region, supporting model simulations and complementary measurements of  
780 shorter-lived species with smaller background concentrations and thus better signal-to-background ratios are  
781 needed (Klausner, 2020).

782 The distribution of highly reactive species such as peroxy radicals, during the flights is determined by the rates  
783 of photochemical production and loss of  $\text{HO}_2$  and organic peroxy radicals  $\text{RO}_2^*$ . The  $\text{RO}_2^*$  measured is the sum of  
784  $\text{HO}_2 + \sum \text{RO}_2^*$ , R being an organic chain which produces  $\text{NO}_2$  in its reaction with NO. Oxygenated VOC (OVOC)  
785 result from the oxidation of VOC emissions (e.g.  $\text{CH}_3\text{COCH}_3$  or HCHO) and are strong sources of  $\text{HO}_2$  and  
786  $\text{CH}_3\text{O}_2$ . The  $\text{RO}_2^*$  mixing ratios observed in EMeRGe are shown in Fig. 16. Mixing ratios up to 120 pptv  $\text{RO}_2^*$ ,  
787 3 ppbv of  $\text{CH}_3\text{COCH}_3$  and 4 ppbv of HCHO were measured in the air masses probed. Provided insolation  
788 conditions (i.e. actinic fluxes) and amount of precursors are similar, the production of peroxy radicals is  
789 observed as long as plumes mix at any altitude. Generally, higher  $\text{RO}_2^*$  were measured below 45°N. This is in  
790 part due to the higher insolation during the flights over the Mediterranean area, which accelerates photooxidation  
791 and the production of  $\text{RO}_2^*$ . The  $\text{O}_3$  production rates calculated from the  $\text{RO}_2^*$  measured on-board are consistent  
792 with the values reported in urban pollution for  $\text{NO} < 1$  ppbv (e.g. Tan et al, 2017; Whalley et al, 2018, 2021). The  
793 photochemical activity of the air masses has been studied using the  $\text{RO}_2^*$ , the trace constituents and photolysis  
794 rates measured during the EMeRGe IOP (George et al., 2021, in preparation).



795

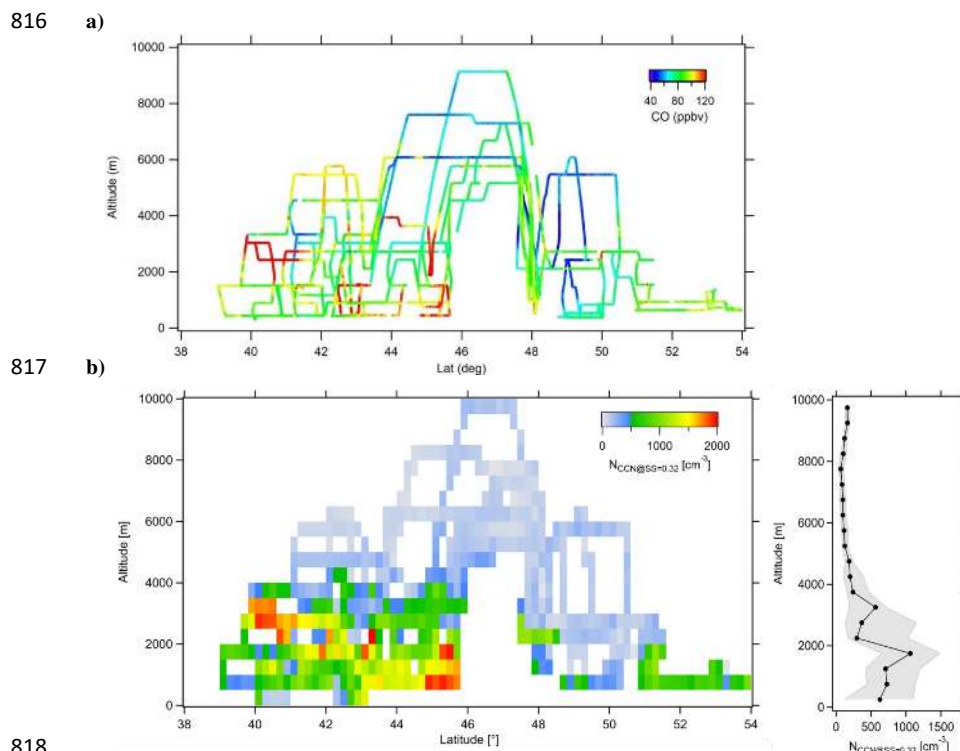
796 **Figure 16:**  $\text{RO}_2^*$  spatial and vertical distribution measured along all EMeRGe flights in Europe.

797 The identification of MPC outflows and the investigation of the pollution events benefits from knowledge of the  
798 mixing of anthropogenic, natural and biogenic sources during the EMeRGe flights. The curtain maps showing  
799 the latitudinal and vertical distributions of selected species help to classify the air mass mixtures, especially in  
800 the lower 2000 m of the troposphere. Differences observed North and South of the Alps are evident in Fig. 17,  
801 showing a reasonable agreement between the vertical distributions of CCN and CO which has been documented  
802 in earlier studies (e.g. Pöhlker et al. 2016, 2018).

803 The vertical and latitudinal distribution of the cloud condensation nuclei number concentration ( $N_{\text{CCN}}$ ) shows a  
804 strong vertical gradient. Generally,  $N_{\text{CCN}}$  is highest in and above the PBL, up to ~2000 m a.s.l. The  $N_{\text{CCN}}$  depend  
805 strongly on the particular air mass, its photochemical history and the source of pollution as shown in Fig. 17b. In  
806 Northern Europe, (50 to 55 °N),  $N_{\text{CCN}}$  up to 1200  $\text{cm}^{-3}$  were measured in the London outflow over the North Sea  
807 and over the BNL/Ruhr region. Below 46 °N,  $N_{\text{CCN}}$  often exceeds 1500  $\text{cm}^{-3}$  above the MPC in the Po Valley,  
808 Rome, Marseille and Barcelona, the highest concentrations being observed in the Po Valley.

809 An interesting observation was the distinct layer of BB smoke measured above the PBL between 2000 and 3500  
810 m altitude, close to Marseille and Barcelona (40 to 42 °N). The high  $N_{\text{CCN}}$  due to BB are episodic in nature,  
811 whereas the CCN emissions from anthropogenic activity are produced daily with probably a weekend  
812 modulation.. The vertical profile in Fig. 17b is a composite of all data but clearly shows that altitudes below  
813 2000 m have the highest  $N_{\text{CCN}}$ . The peak between 2000 and 4000 m is associated with air masses, which either  
814 come from BB events upwind and flow into the Mediterranean, or are Po Valley air being lifted up the Alps.

815



818

819 **Figure 17:** Vertical and latitudinal distribution observed during the EMeRGe IOP of a) CO mixing ratios, and b) CCN  
820 number concentration at a supersaturation ( $S$ ) of 0.32 % (except for E-EU-04, due to instrumental failure). The CCN curtain  
821 plot on the left is made with latitude- ( $0.2^\circ$ ) and altitude-binned (500 m) CCN number concentrations. On the right, the  
822 median vertical  $N_{\text{CCN}}(S=0.32\%)$  profile is represented by a solid black line and the interquartile range by a grey shaded area.  
823 CCN data is STP corrected.

#### 824 4 Identification of pollution outflows within the EMeRGe IOP in Europe

825 The investigation of transport and transformation of MPC outflows over Europe benefits from the unambiguous  
826 identification of individual MPC sources. With this objective, a series of complementary plume tagging or  
827 identification approaches were used in the EMeRGe IOP in Europe:

828

##### 829 I) Enhancement in the concentration of selected atmospheric species

830 Periods in which large pollution plume events were measured on-board HALO were initially categorised into the  
831 following: a) anthropogenic pollution (AP), b) biomass burning (BB) and c) mixed plumes, by using the  
832 presence and enhancements of VOCs in these plumes, which are characteristic for different sources. For  
833 example,  $\text{CH}_3\text{CN}$  is almost exclusively emitted from BB (de Gouw et al., 2003; Warneke et al., 2010) whereas  
834  $\text{C}_6\text{H}_6$  is emitted by traffic and petroleum- related industrial activities (Paz et al., 2015) as well as BB (Simpson et  
835 al., 2011; Andreae, 2019). Hence,  $\text{C}_6\text{H}_6$  enhancements in the absence of  $\text{CH}_3\text{CN}$  can be used to identify relatively  
836 “pure” anthropogenic pollution. Similarly,  $\text{CH}_3\text{CN}$  enhanced plumes in the absence of  $\text{C}_6\text{H}_6$  are identified as pure  
837 or aged BB events. Events with only  $\text{CH}_3\text{CN}$  can originate from mixed sources, as  $\text{C}_6\text{H}_6$  may have decayed  
838 while  $\text{CH}_3\text{CN}$  remains, due to the different atmospheric lifetimes of these two tracers ( $\text{CH}_3\text{CN} \sim 6$  month,  $\text{C}_6\text{H}_6 \sim$



839 10 days). When both VOCs are enhanced, the plumes are considered to have air masses from either BB and AP  
840 sources or only from recent BB. Additionally, enhanced  $C_5H_8$  as short-lived biogenic tracer is used as an  
841 indicator for recent contact with the PBL having biogenic sources (Förster et al., 2021, in preparation).  
842 These large categorised pollution events were then further classified into single plumes by using altitude, water  
843 content, wind direction and enhancements in the concentrations of pollution tracers such as CO and  $NO_y$   
844 measured on-board HALO. Fine structures or signatures in individual plumes were numbered relative to the  
845 main plume event they belong to.

846 All plumes encountered are numbered using the notation E-EU-FN-S-PL similarly to the flight nomenclature  
847 mentioned in Sect. 2.3, i.e., E stands for EMeRGe, EU for the campaign in Europe, FN are 2 digits for the flight  
848 number, S is the letter assigned to the identified captured pollution event, and PL are two digits reserved for the  
849 plume number within each pollution event.

850

851 II) Backward trajectories: last contact with PBL

852 The origin and history of the plumes probed at each point of the flight track are traced by using highly-resolved  
853 backward trajectories calculated by the kinematic trajectory model FLEXTRA (Stohl et al., 1995, 1999).  
854 Parameters calculated using FLEXTRA and meteorological fields are used to assign the origin of the observed  
855 plumes to the EMeRGe targets in different parts of the flight tracks. Typically, the last contact to the PBL  
856 (lcPBL), i.e., the time when the backward trajectory reaches the PBL the first time, and sensitivity trajectories  
857 which provide the probability of contact of a particular air mass with the lower meters of the PBL before the  
858 measurement are used. This information is cross-checked with the estimated age of air masses based on  
859 HYSPLIT CO dispersion calculations in III). More details about trajectories and related parameters are given in  
860 S11 in the supplement.

861

862 III) Forward trajectories: dispersion of MPC outflows

863 In a similar approach to that used in the forecast procedures (see Sect. 2.3 and S3 in the supplement), the  
864 HYSPLIT dispersion model was used to calculate the dispersion of CO emissions using emission rates from the  
865 EDGAR HTAP V2 emission inventory. They are expressed as CO enhancement caused by the selected MPC  
866 outflow over the CO background. The performances of FLEXPART and HYSPLIT for the EMeRGe data are  
867 compared for the case studies within EMeRGe.

868

869 IV) Detection of released PFC tracers

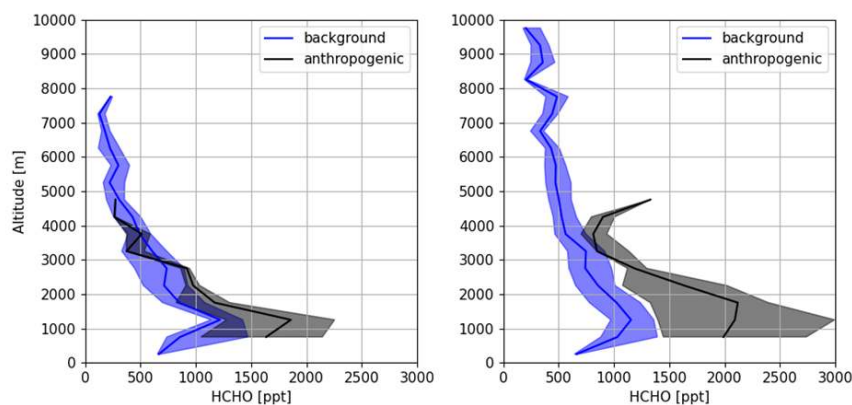
870 Sampling of PMCH from a tracer release in the centre of London during E-EU-05, and from a tracer release in  
871 the centre of London and at the University of Wuppertal during E-EU-08, enabled the prediction of the  
872 dispersion and the mixing of the targeted MPC outflows in these flights to be compared. Details on the tracer  
873 experiments during the EMeRGe IOP over Europe are described in Schlager et al. (2021 in preparation).

#### 874 4.1 Characterisation of polluted air masses by using chemical tracers

875 Initially, as described in I) in the previous section, in-situ measurements of  $C_6H_6$  and  $CH_3CN$  on-board HALO  
876 (Förster et al., 2021, in preparation) were used to identify measurements of unpolluted background air (absence  
877 of both tracers) and of anthropogenic polluted air masses (enhancement of  $C_6H_6$  and absence of  $CH_3CN$ ).



878 In Fig. 18, the HCHO measured by the miniDOAS and HKMS instruments on board is shown. In the air masses  
879 classified as polluted the HCHO results from direct emission and oxidation of VOC precursors and is discernibly  
880 higher than the lower boundary of the measurements. The HCHO in the less polluted or background air in  
881 Europe is then attributed to be predominantly released from CH<sub>4</sub> oxidation.

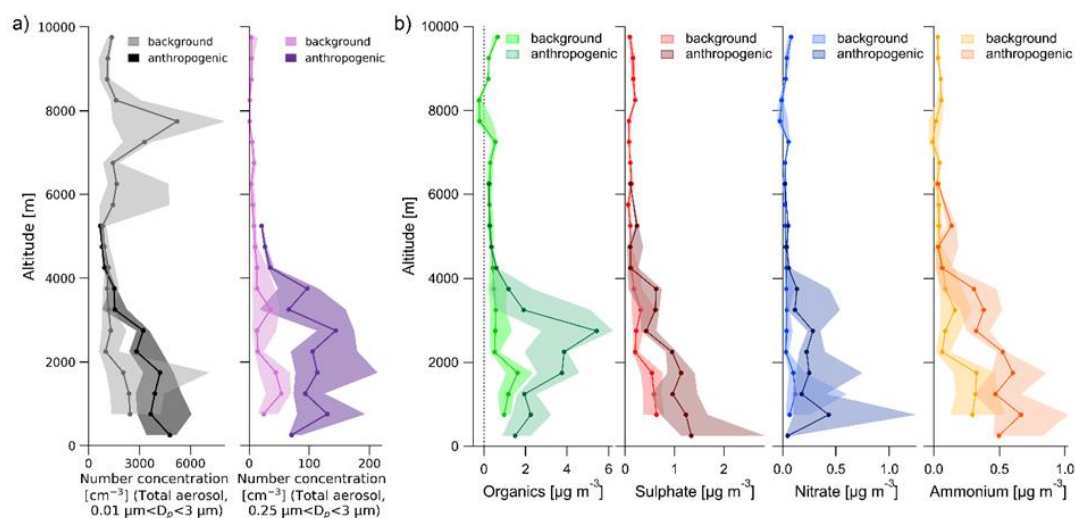


882

883 **Figure 18:** Vertical profiles of HCHO (miniDOAS left, HKMS right) for pure anthropogenic emissions (C<sub>6</sub>H<sub>6</sub>  
884 enhancement in absence of CH<sub>3</sub>CN) and background air (in the absence of C<sub>6</sub>H<sub>6</sub> and CH<sub>3</sub>CN). Shaded areas are the  
885 quartiles, solid lines represent median concentrations.

886 In a similar manner, the aerosol particle concentration and composition have been tagged for anthropogenic and  
887 background air masses (see Fig. 19).

888



889

890 **Figure 19:** As in Fig. 18, for a) the total aerosol number concentrations for two different size ranges (0.01-3 µm and 0.25-3  
891 µm) and b) organic, sulphate, nitrate and ammonium mass concentrations in the aerosol particles. The dots in the solid lines  
892 represent the medians averaged over altitude bins of 500 m and the shaded areas are the quartiles.



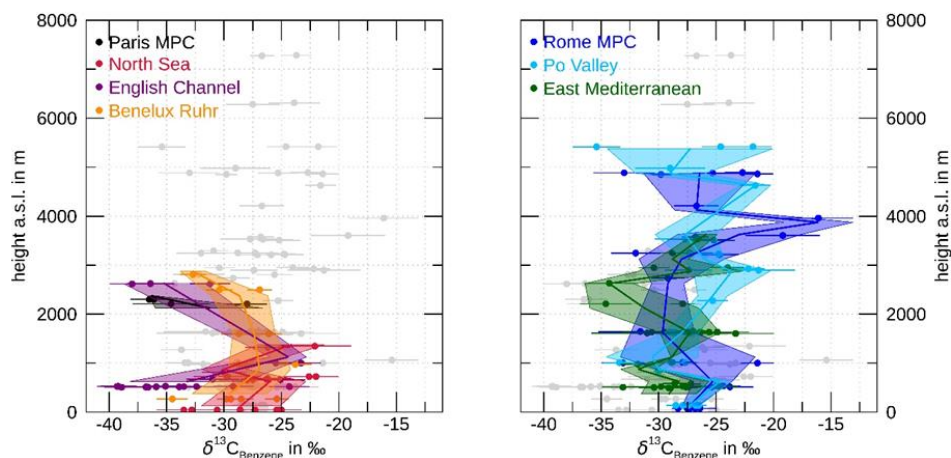
893 In the vertical distribution of the total aerosol number concentrations (Fig. 19a), the difference between  
894 anthropogenic and background air masses is more pronounced in the size range between 0.25  $\mu\text{m}$  and 3  $\mu\text{m}$  than  
895 in the size range between 0.01  $\mu\text{m}$  and 3  $\mu\text{m}$ . At altitudes below 4000 m the averaged total aerosol number  
896 concentrations show several maxima which are mainly caused by local pollution plumes. In contrast to all other  
897 profiles, there are two additional maxima in the number concentration compared to background aerosol for the  
898 size range 0.01  $\mu\text{m}$  to 3  $\mu\text{m}$  at around 6000 m and 7500 m. These maxima are not apparent in the profiles of  
899 particle larger than 0.25  $\mu\text{m}$ . This is consistent with the attribution of LRT of air masses from North America,  
900 where they had contact with BB emissions. New particle formation events cannot be excluded but are considered  
901 unlikely.

902 The vertical profiles of the chemically resolved aerosol mass concentrations in Fig. 19b clearly show the  
903 enhanced concentrations in the anthropogenically influenced air masses compared to the background air masses.  
904 Differences in the median vertical profiles of the inorganic and organic aerosol suggest that organic aerosol in  
905 anthropogenic air masses is mainly formed by secondary processes. As a result of the time required by the  
906 emitted precursor VOCs to be converted into secondary organic aerosol, the anthropogenic organic aerosol  
907 concentration increases above 2000 m altitude. In contrast, the inorganic components of the aerosol, especially  
908 ammonium and sulphate ions, show a steady decrease in the anthropogenically influenced air masses until up to  
909 about 4000 m. Above that altitude, the difference between background and anthropogenic profiles becomes  
910 small for both organic and inorganic aerosol components. This is a very interesting finding, implying that the  
911 direct influence of anthropogenic emissions on the aerosol of the free troposphere over Europe is small.

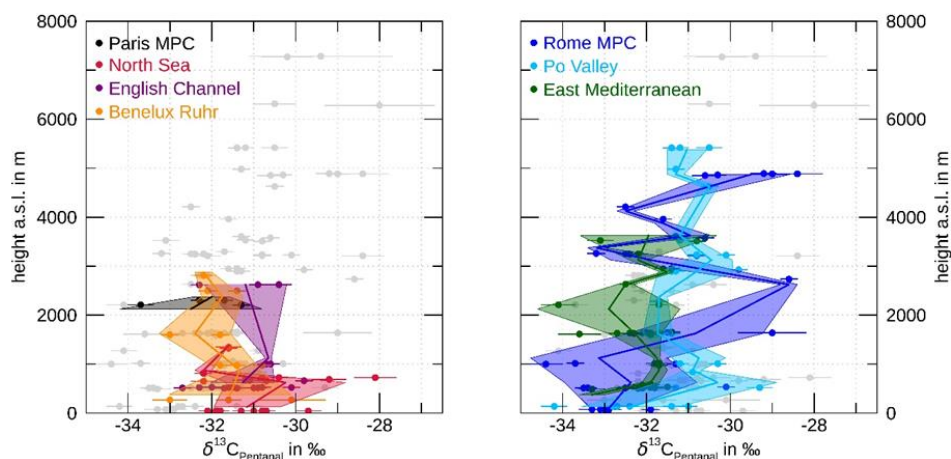
912 Additional information is provided by the vertical distribution of carbon isotope ratios obtained from whole air  
913 samples taken on HALO and at the ground sites in London, Wuppertal, Milan and Rome. The  $\delta^{13}\text{C}$  values in  
914 pentanal ( $\text{C}_5\text{H}_{10}\text{O}$ ) and  $\text{C}_6\text{H}_6$  shown in Fig. 20 are colour coded according to the different areas sampled, as given  
915 in the overview map in Fig. 4. In general, the  $\delta^{13}\text{C}$  values are in the expected range reported by previous studies  
916 (e.g. Rudolph et al., 2000; Goldstein and Shaw, 2003).

917 The air samples taken during the EMERGe IOP at ground stations exhibited different features in  $\delta^{13}\text{C}$  values for  
918 the Southern and for the Northern European MPCs. In general, lower  $\delta^{13}\text{C}$  values for  $\text{C}_5\text{H}_{10}\text{O}$  and  $\text{C}_6\text{H}_6$ ,  
919 indicative of fresh emissions, were observed below 2000 m altitude. On average,  $\text{C}_5\text{H}_{10}\text{O}$  is less enriched in  $^{13}\text{C}$   
920 in the Rome and Milan (-32.6 ‰) than in the London and Wuppertal samples (-31.4 ‰), whereas it is the  
921 opposite for  $\text{C}_6\text{H}_6$ , i.e., (-27.3 ‰) and (-29.0 ‰), respectively. Moreover, the  $\delta^{13}\text{C}$  ground values in Italy indicate  
922 more constant sources in  $\text{C}_5\text{H}_{10}\text{O}$  and  $\text{C}_6\text{H}_6$  as in the Northern MPCs, as is apparent from the standard deviations  
923 of 0.8 ‰ and 0.7 ‰ in contrast to 1.2 ‰ and 3.3 ‰, respectively.

924 The EMERGe flights to the Southern MPCs in Europe covered a larger altitude range than the flights to the  
925 Northern MPCs. The upwind and downwind shuttles at different flight altitudes of the Rome MPC illustrate a  
926 general increase in  $\delta^{13}\text{C}$  in  $\text{C}_5\text{H}_{10}\text{O}$  and  $\text{C}_6\text{H}_6$  with increasing altitude. This implies that chemically processed air  
927 was encountered during the transits over the Apennines. In comparison to  $\text{C}_5\text{H}_{10}\text{O}$ , the enrichment in  $^{13}\text{C}$  with  
928 altitude in  $\text{C}_6\text{H}_6$  is not very pronounced. This is consistent with the longer lifetime of  $\text{C}_6\text{H}_6$  and a well-mixed  
929 troposphere with a variety of ground sources mixed by convection in summer. Consequently, the values for  $\delta^{13}\text{C}$   
930 in  $\text{C}_5\text{H}_{10}\text{O}$  represent local conditions, whereas those in  $\text{C}_6\text{H}_6$  provide regional or LRT information. The isotopic  
931 signatures reveal a second layer with rather fresh emissions in the altitude region between 2000 and 3000 m  
932 which extends to 4000 m in the Southern MPCs (e.g. Rome and Po Valley). These observations are consistent  
933 with the trace gases and aerosol measurements.



934



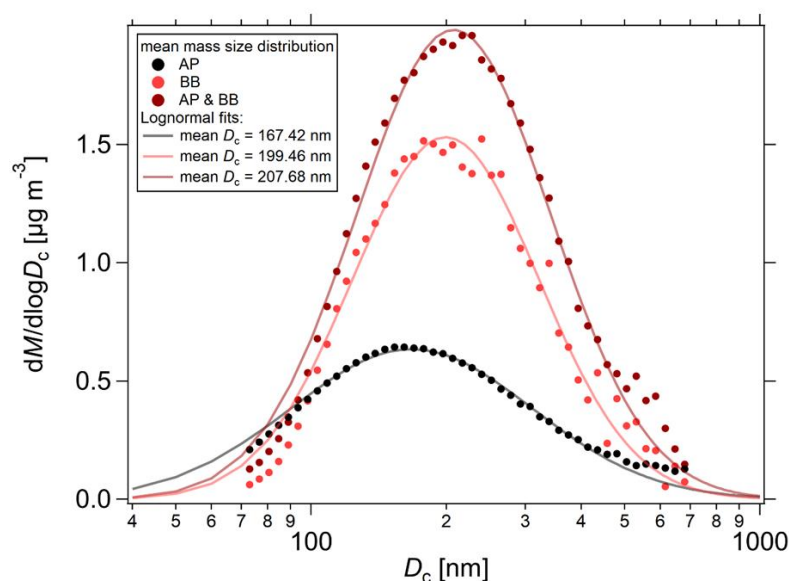
935

936 **Figure 20:** Vertical distribution of  $\delta^{13}\text{C}$  values in  $\text{C}_5\text{H}_{10}\text{O}$  (left) and  $\text{C}_6\text{H}_6$  (right) in whole air samples taken on HALO and at  
937 the ground sites in London, Wuppertal, Milan and Rome. Data for northbound flights (left column) are colour coded for Paris  
938 MPC (black), North Sea (red), English Channel (violet), BNL/Ruhr (orange). Data for southbound flights (right column) are  
939 colour coded for Rome MPC (blue), Po Valley MPC (cyan) and East Mediterranean (green). The coloured shadings refer to  
940 the standard deviation of  $\delta^{13}\text{C}$  values in altitude bins of 250 m. Mean  $\delta^{13}\text{C}$  values of the respective altitude bins are  
941 represented as solid colour-coded lines. The  $\delta^{13}\text{C}$  values at the lowest altitudes in each colour represent the results of air  
942 samples at the ground stations: London (red), Wuppertal (orange), Rome (blue) and Milan (cyan). Error bars in  $\delta^{13}\text{C}$  are  
943 given for each sample value.

944 Typically, plumes of anthropogenic and biogenic origin were mixed in the air probed over Europe. The EMeRGe  
945 IOP was characterised by the contribution of fresh wildfires in the Mediterranean area, which add BB signatures  
946 to the probed air masses, and mixed with anthropogenic plumes as indicated by VOCs and in particular by the  
947  $\text{CH}_3\text{CN}$  observations. For particles emitted from BB, a frequently used tracer is levoglucosan which is identified  
948 using the  $m/z$  60 ion ( $\text{C}_2\text{H}_4\text{O}_2^+$ ) in aerosol mass spectrometry (Schneider et al., 2006; Alfara et al., 2007). The  
949 photochemical degradation of levoglucosan is fast in summer (Hennigan et al., 2010, 2011; Lai et al., 2014), and  
950 the BB aerosol observed during the IOP in Europe flight tracks was generally processed too fast to be  
951 distinguished from other secondary aerosol.



952 A more robust indicator for particles from BB is BC. BC particles are formed in processes of incomplete  
953 combustion, and therefore are an important component of both BB and urban aerosol particles (Bond et al.,  
954 2013). The microphysical properties of BC give insights into the combustion sources and atmospheric ageing  
955 time of the pollution plumes (Liu, 2014, Laborde, 2012, Holanda et al., in preparation 2021). Figure 21 shows  
956 average BC mass size distributions for different plumes encountered during the E-EU-06 flight (anthropogenic,  
957 BB, and mixture). The plumes were classified according to the VOC observations as described in I) in Sect. 4.  
958 Larger BC cores were found in pure BB plumes and mixed BB and AP plumes, with mean modal diameter ( $D_c$ )  
959 of 200 and 210 nm, respectively. Smaller BC cores, with mass size distribution peaking at  $D_c = 170$  nm, were  
960 found in urban pollution, as a result of the different fuel burnt and combustion conditions. These values obtained  
961 during EMERGE are consistent with previous aircraft observations for urban and BB plumes (Schwarz et al.,  
962 2008; Laborde et al., 2013). During E-EU-06, the average total BC mass concentration was also substantially  
963 higher in BB and mixed BB (  $0.61 \pm 0.12 \mu\text{g m}^{-3}$  and  $0.81 \pm 0.35 \mu\text{g m}^{-3}$ , respectively) than in urban pollution  
964 ( $0.35 \pm 0.15 \mu\text{g m}^{-3}$ ).



965

966 **Figure 21:** Mean mass size distribution of black carbon particles measured in anthropogenic pollution (AP, black),  
967 BB (light red), pollution from anthropogenic/ BB mix (AP & BB, dark red) during E-EU-06 on 20 July 2017.  
968 Lognormal fits were applied to the mean size distributions for  $100 < D_c < 300$  nm.

#### 969 4.2 Identification and classification of MPC outflows: London

970 The flight E-EU-08 on 26 July 2017 has been selected to illustrate the procedure for the identification and  
971 classification of air mass origin and the different source contributions to the plumes. As briefly described in Sect.  
972 3.3, the E-EU-08 investigated the London and BNL/Ruhr MPC outflows. HYSPLIT dispersion calculations of  
973 the CO city plumes were used to define the location of the outflows, which were measured along the Eastern UK  
974 coast between 10 and 12 UTC and over the European continent between 13:20 and 14:15 UTC approximately.  
975 Cloudy and rainy conditions prevailed throughout the flight reduced flight visibility and limited further tracing  
976 of the BNL/Ruhr outflow over Germany in the afternoon. However, the PMCH was observed from the two  
977 releases showing the success of this technique and the adequacy of the description of the transport in HYSPLIT.

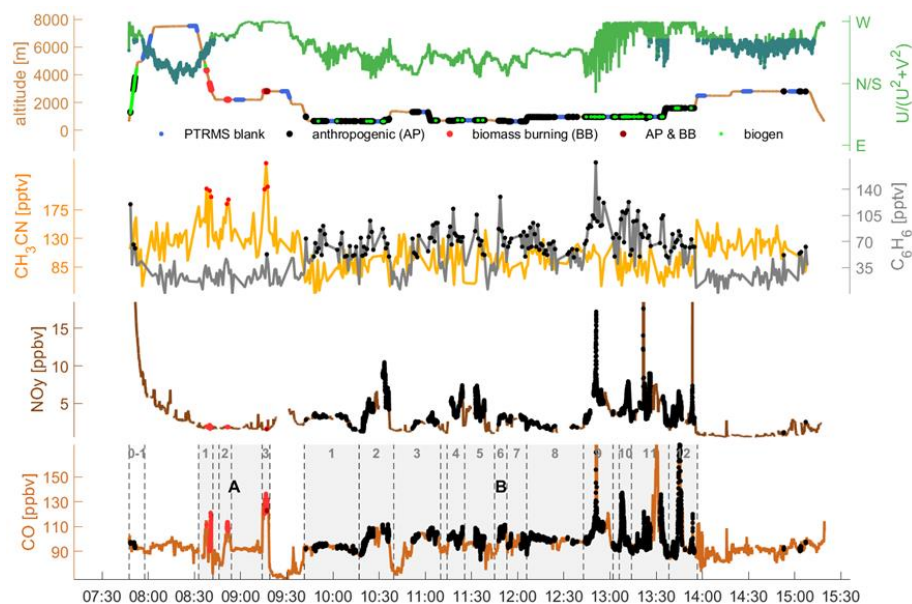




#### 978 4.2.1 Identification of pollution plumes

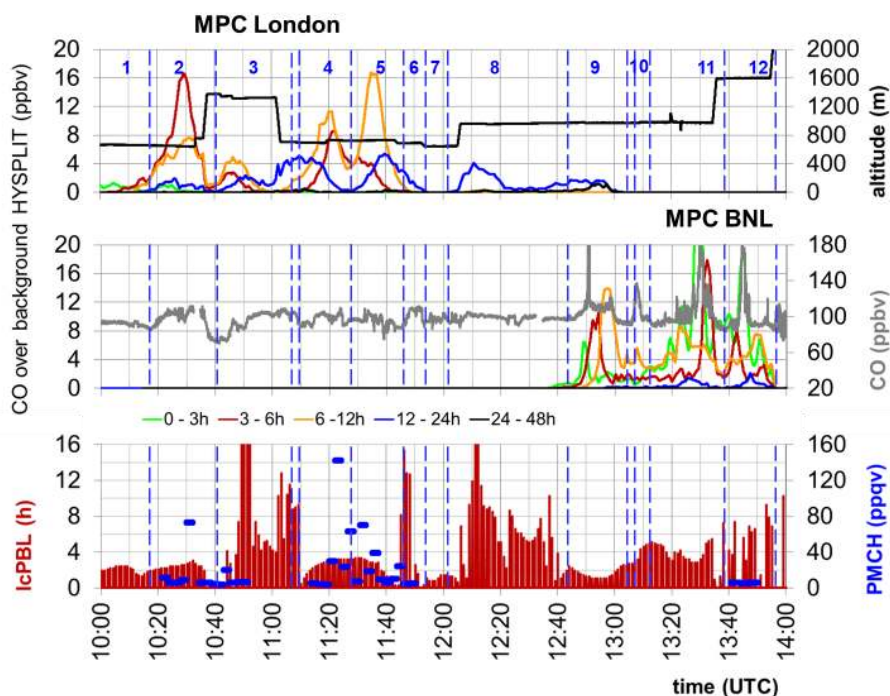
979 Figure 22 shows the time series of  $C_6H_6$  and  $CH_3CN$ , their enhancements colour-coded on the altitude and the  
980 identified plumes along the flight by using the time series of  $CO$  and  $NO_y$ , as described in I) in Sect. 4. Figure 23  
981 summarises the result of applying the tagging tools II) and III) to the E-EU-08. Overall, the HYSPLIT dispersion  
982 and FLEXTRA backward calculations agree reasonably in identifying fresh emitted London plumes such as B-  
983 02 and B-04: the measured 22 and 19 ppbv  $CO$  increases over background are estimated by HYSPLIT as 25 and  
984 22 ppbv (sum of all transport times). B-05 is a good example of significant mixing with aged plumes (12-24 h)  
985 which seem to dominate in B-06 and B-08 (see detail in Fig. 23). Plume B-09 is a good example of mixing of  
986 freshly emitted plumes from BNL/Ruhr (0-6 h) and aged emissions (>24 h) of London origin. The PFC tracer  
987 measured on-board is also depicted in Fig. 23. For B-02, B-04 and B-05, enhanced PMCH volume mixing ratios  
988 above the 8.5 ppqv atmospheric background in Europe were clearly detected.

989



990

991 **Figure 22:** Time series for E-EU-08 on the 26 July 2017 used for the categorisation of plumes based on VOC  
992 measurements: altitude, wind direction,  $CH_3CN$ ,  $C_6H_6$  and  $NO_y$  as refinement. The wind direction is given as  
993  $U/(U^2+V^2)$ , -1 is east wind, +1 is west wind, values around zero have North or South components. South components  
994 are marked with dark green colour. Altitude is colour-coded in light-green during  $C_5H_8$  enhancements, in light red  
995 during  $CH_3CN$  enhancements, in black during  $C_6H_6$  enhancements and in dark red during both,  $CH_3CN$  and  $C_6H_6$   
996 enhancements. Additionally, blue colour-coded blank measurements of  $CH_3CN$ ,  $C_6H_6$  and  $C_5H_8$  are given. Final  
997 numbering of structures and plumes according to concentration enhancements are shown for  $CO$ . Colour-coding  
998 indicates  $CH_3CN$  enhancements (light red),  $C_6H_6$  enhancements (black), and both,  $CH_3CN$  and  $C_6H_6$   
999 (dark red).



1000

1001 **Figure 23:** Detail of the MPC outflow of London (B-01 to B-09) and BNL/Ruhr (B-09 to B-12) probed with HALO along  
1002 the E-EU-08 flight track. Numbering in blue corresponds with the classification in Fig. 22 (B is omitted for simplicity). The  
1003 position of the plumes is also indicated by the blue lines. Dispersion of CO emissions of target MPCs and the transport time  
1004 of the air mass calculated by HYSPLIT are depicted. The last contact with the PBL (IcPBL) calculated using FLEXTRA is  
1005 also shown. Elevated PMCH mixing ratios were measured for B-02, B-04 and B-05.

1006 The plumes identified using I, i.e., enhanced concentrations of mixing ratios of selected atmospheric species,  
1007 and the MPC assigned outflow with the estimated air-mass transport times are summarised in Table 5. These  
1008 plumes show mixtures of anthropogenic pollution (AP), BB and biogenic emissions (BIO).

1009



1010 **Table 5:** Synopsis of identified structures (A and B) and plumes with anthropogenic (AP), biomass burning (BB) and  
1011 biogenic signatures (BIO), MPC assignments and estimated transport times (Ttime) based on HYSPLIT and FLEXTRA for  
1012 E-EU-08.

Notation	begin [UTC]	end [UTC]	signature	MPC origin	Ttime [h]
E-EU-08-0-01	07:47:34	07:57:40	BB, BIO		
E-EU-08-A-00	08:32:45	09:19:00			
E-EU-08-A-01	08:32:45	08:42:00	BB		
E-EU-08-A-02	08:46:00	08:54:00	BB		
E-EU-08-A-03	09:14:00	09:19:00	AP, BB		
E-EU-08-B-00	09:41:25	13:56:45			
E-EU-08-B-01	09:41:25	10:17:00	AP, BIO	London	0-3
E-EU-08-B-02	10:17:00	10:39:30	AP, BIO	London	0-3
E-EU-08-B-03	10:39:30	11:10:00	AP, BIO	London	6-24
E-EU-08-B-04	11:14:10	11:25:35	AP, BIO	London	3-6
E-EU-08-B-05	11:25:35	11:45:00	AP, BIO	London	3-6
E-EU-08-B-06	11:45:00	11:53:00	AP	London	12-24
E-EU-08-B-07	11:53:00	12:05:50	AP		
E-EU-08-B-08	12:05:50	12:42:45	AP	London	12-24
E-EU-08-B-09	12:42:45	13:02:00	AP, BIO	London/BNL/Ruhr	12-48/0-6
E-EU-08-B-10	13:06:00	13:14:00	AP, BIO	BNL/Ruhr	0-12
E-EU-08-B-11	13:14:00	13:38:15	AP, BIO	BNL/Ruhr	0-3
E-EU-08-B-12	13:38:15	13:56:45	AP, BIO	BNL/Ruhr	0-3

1013

#### 1014 4.2.2 Characterisation of the MPC London outflow

1015 The vertical and horizontal extension of the observed outflows during EMeRGe is investigated by combining the  
1016 information from transects and shuttles in selected areas. Figure 24 shows, as an example, the CO, O<sub>3</sub>, SO<sub>2</sub>,  
1017 RO<sub>2</sub>\*, NO<sub>y</sub>, NO, C<sub>6</sub>H<sub>6</sub> and BC observations made for the B-01 to B-12 plumes during the E-EU-08 flight. The E-  
1018 EU-08 track included a flight transect (a-b-c-d-e) at approximately 600 m altitude and a shuttle (600-1400 m)  
1019 between b-c and c-d in the outflow of London from 10 UTC to 12 UTC. A second shuttle (g-h-i) at 900, 1500  
1020 and 2400 m was made in the BNL outflow from 13:20 UTC approximately. Relevant changes in the HALO  
1021 course and altitude are marked by coloured circles and letters in Fig. 24.

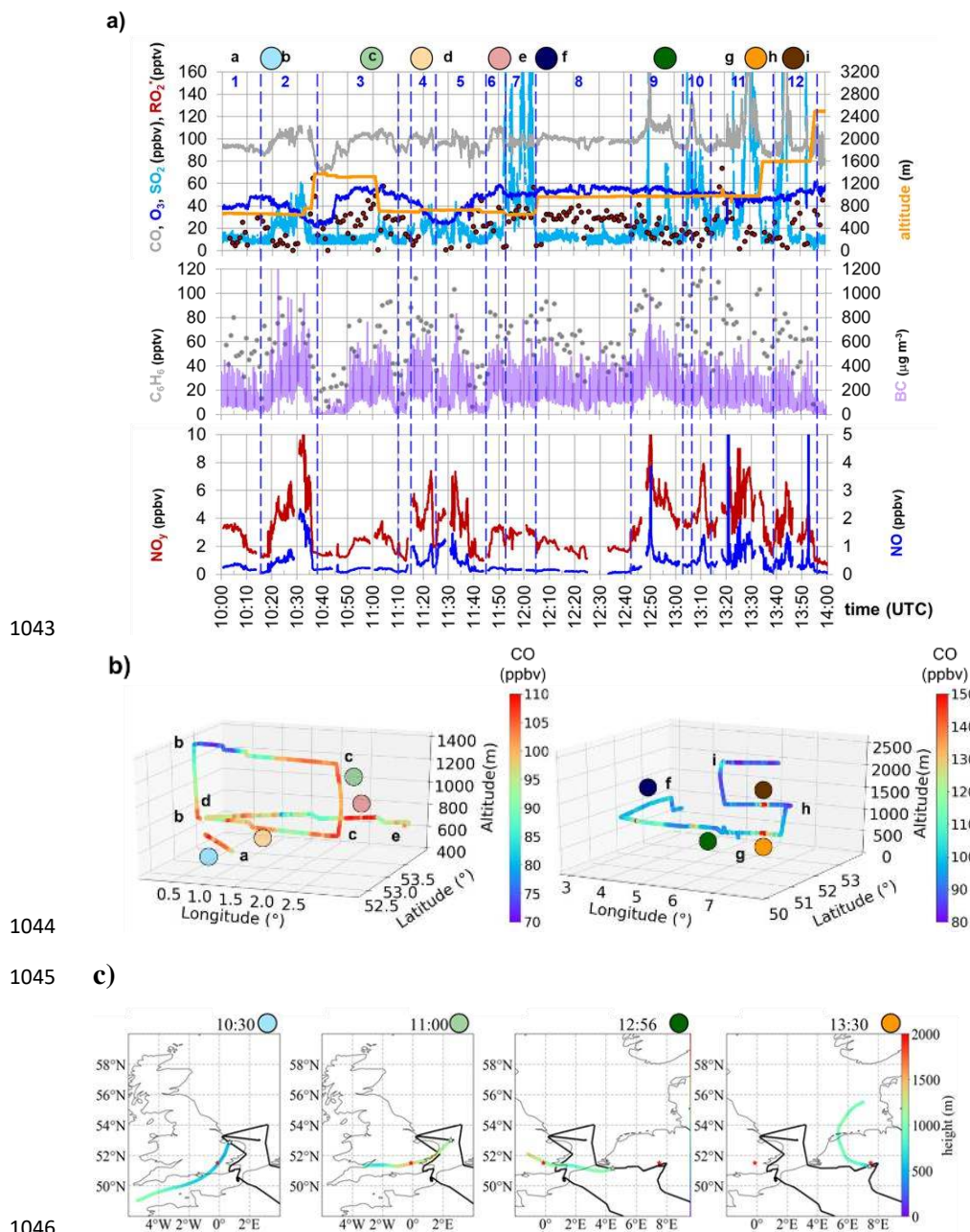
1022 Backward trajectories indicate that the air measured at around 10:30 UTC at 600 m (blue circle), 11:00 UTC  
1023 (point c at 1400 m and 600 m), 11:20 UTC (yellow circle) and 11:50 UTC at 600 m (pink circle) had passed over  
1024 the MPC London a few hours before being probed at an altitude below 1000 m. Selected backward trajectories  
1025 are shown in Fig. 24c. At these times, the measured enhancements in CO and NO<sub>y</sub> and the NO/NO<sub>y</sub> ratios are in  
1026 reasonable agreement with the transport time predicted by HYSPLIT for the CO enhancement in the MPC  
1027 London plumes in Fig. 23. For plume B-02, HYSPLIT predicts the London contribution to be a mixture of air  
1028 masses transported in the previous 3 to 24 hours. The air probed had up to 10 ppb of NO<sub>y</sub> and approximately 2  
1029 ppbv NO. The latter suppresses RO<sub>2</sub>\*. OH and RO are produced but also react with NO and NO<sub>2</sub>. These  
1030 measurements confirm the predicted mixing of relatively fresh emissions with aged and more photochemically  
1031 processed air masses. The vertical distribution of CO in the plume during the shuttles is depicted in the 3D  
1032 diagrams in Fig. 24b. The CO measured indicates that the plume B-03 is well mixed horizontally with the plume  
1033 B-06 up to 1400 m altitude. According to the backward trajectories (not shown), the plume at 11:52 UTC is



1034 transported from the Northeast coast of UK and had no recent contact with the outflow of London. This is  
1035 distinguishable by the significantly higher SO<sub>2</sub> mixing ratios measured.

1036 The plumes B-08 and B-09 measured over the continent at 900 m are predicted to have been in contact with  
1037 emissions of the MPC London within the previous 24 hours (Fig.23 and Fig. 24c). From 12:50 UTC the air  
1038 probed is expected to mix with recent emissions of the MPC BNL as indicated by the observed higher NO levels  
1039 and enhancements in NO<sub>y</sub>, SO<sub>2</sub> and C<sub>6</sub>H<sub>6</sub> in Fig. 24a.

1040 The composition of the air measured during the shuttle between the way points g and h in Fig. 24a at 13:30 and  
1041 13:45 UTC and the backward trajectories indicate that the outflow from the MPC BNL was sampled in a plume  
1042 extending from 1000 m to 1500 m. This air mass was not detectable at 2500 m.

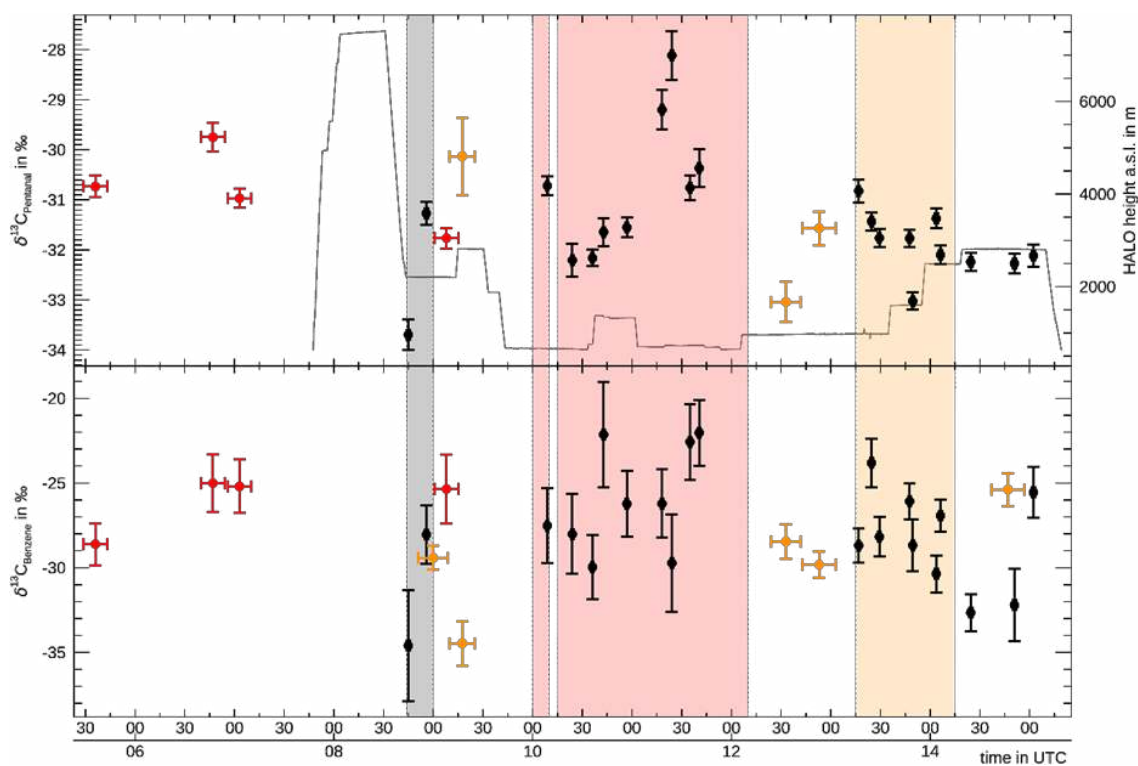


1047 **Figure 24:** a) CO, O<sub>3</sub>, SO<sub>2</sub>, RO<sub>2</sub><sup>\*</sup>, NO<sub>y</sub>, NO, C<sub>6</sub>H<sub>6</sub> and BC measured in the outflow of London and BNL during E-EU-08 on  
 1048 26 July 2017. The position and numbering of the plumes is indicated by blue lines and numbers as classified in Fig. 22 (B is  
 1049 omitted for clarity). b) 3D shuttles colour coded with the CO mixing ratios observed. Relevant changes in the HALO course  
 1050 and altitude are marked by colour circles and letters (a-i). c) Selected backward trajectories (24h). The red stars indicate the  
 1051 position of the MPCs of interest.

1052 Further information about the characteristics of the plumes is obtained from the air samples gathered with  
 1053 MIRAH on-board HALO and on the ground sites in London and Wuppertal during the flight E-EU-08. As stated



1054 in 4.1, lower carbon isotope ratios indicate fresh emissions, whereas higher values indicate an enrichment of the  
1055 compound in  $^{13}\text{C}$ , which is linked to chemical ageing.  
1056 In Fig. 25, the measured  $\delta^{13}\text{C}$  values of  $\text{C}_5\text{H}_{10}\text{O}$  and  $\text{C}_6\text{H}_6$  are shown as examples. The identified London outflow  
1057 is also evident in the carbon isotope ratios obtained from HALO samples taken between 10 and 11 UTC. The  
1058 latter remain in the range of the representative source values from whole air samples collected at the ground  
1059 station in London. The higher  $\delta^{13}\text{C}$  values observed between 11:10 and 12:00 UTC indicate chemically-  
1060 processed London outflow air.  
1061 Later in the flight, the  $\delta^{13}\text{C}$  values measured over the BNL/Ruhr area are in the range of the source values in air  
1062 samples collected in Wuppertal. The range in  $\delta^{13}\text{C}$  values of  $\pm 1.5\text{‰}$  in  $\text{C}_5\text{H}_{10}\text{O}$  ( $\pm 3.5\text{‰}$  in  $\text{C}_6\text{H}_6$ ) implies a  
1063 mixture of slightly aged air and rather fresh emissions from the Ruhr area.  
1064



1065  
1066 **Figure 25:**  $\delta^{13}\text{C}$  values in  $\text{C}_5\text{H}_{10}\text{O}$  (top panel) and  $\text{C}_6\text{H}_6$  (bottom panel) in whole air samples gathered with the whole air  
1067 sampler MIRA on the HALO aircraft (black) during E-EU-08 as well as on the ground sites in London (red) and Wuppertal  
1068 (orange). The HALO flight altitude is given in grey on the top panel. Background shadings indicate different measurement  
1069 regions during the flight according to Fig. 4: Paris (grey), South of London and North Sea region (red), BNL/Ruhr (orange).  
1070 Pollution plumes of the London MPC outflow were also assigned during E-EU-05. These were measured after  
1071 transport over the English Channel and to the European continent. Similar to the study of Ashworth et al. (2020),  
1072 the processing of the plumes from the emissions probed by the FAAM aircraft in the circuits around London will  
1073 be addressed in separate publications. Observations of the released PFC tracer in London improved the definition  
1074 of the plume in the area of measurement.



1075 **4.3 Specific case studies of MPC outflows**

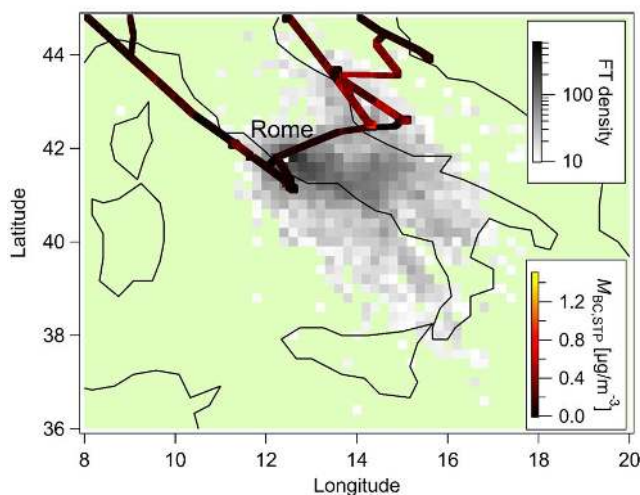
1076 In addition to the plume from London, other MPC outflows were identified and analysed during the EMERGE  
1077 IOP in Europe by combining tagging and observational tools. Two representative case studies are briefly  
1078 presented in the following. The corresponding detailed analysis is subject of separate publications.

1079 **4.3.1 MPC Po Valley and Rome**

1080 Shuttles at different altitudes upwind of Rome in the Mediterranean and along the Adriatic coast during the  
1081 flights E-EU-03 and E-EU-06 provided information about the vertical distribution of trace gases at different  
1082 distances from the sources of the MPC Po Valley and MPC Rome.

1083 As for the MPC London case in Sect. 4.2., backward and sensitivity trajectories support the identification of  
1084 plumes downwind from these MPCs. The density distribution for forward trajectories (FT) of MPC Rome  
1085 outflows in Fig. 26 highlights the typical transport pattern towards the Adriatic coast and the representativeness  
1086 of the HALO measurements. The flight tracks for E-EU-03 and E-EU-06 are colour-coded with the BC mass,  
1087 showing a good agreement between the four-year FT analysis and the actual in-situ measurements. These results  
1088 also strengthen the assumption of the HALO measurements being representative for the transport of air masses  
1089 from the MPC Rome. The FT density distribution was calculated as explained in Pöhlker et al., (2019). The FT  
1090 starts at 100 m above ground level for the month of July in a multi-year period (2017 until 2020) by using the  
1091 HYSPLIT package (version 4, Revision 664, October 2014) (Stein et al., 2015; Rolph et al., 2017).

1092 For the Rome MPC, the airborne measurements at low altitudes made by the Sky Arrow research aircraft agree  
1093 reasonably well with the columnar amounts of gases observed by the PANDONIA global network for air quality  
1094 and atmospheric composition (<https://www.pandonia-global-network.org/>) and the remote sensing observations  
1095 on-board HALO. These data support the determination of the geographical extension and location of the Rome  
1096 outflow (see Barnaba et al., Campanelli et al., in preparation 2021).

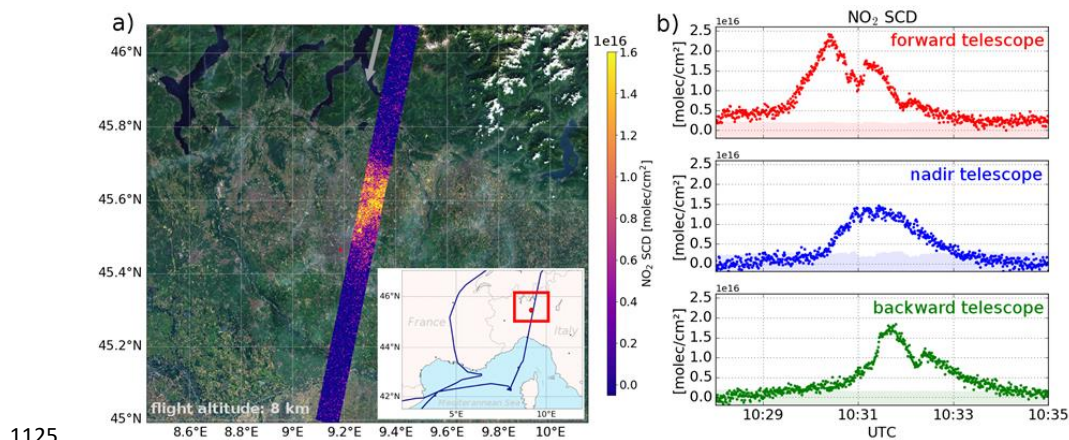


1097

1098 **Figure 26:** Forward trajectory (FT) density plot for air masses starting in Rome (100 m a.g.l.) in the month  
1099 of July from multiple years (2017 to 2020). The grey scale represents the counts of FT points in each grid  
1100 cell. The flight track of E-EU-03 and E-EU-06 is colour-coded with the BC mass concentration.



1101 The MPC Po Valley has surface emissions from the urban agglomeration over a relatively large area. It is a good  
1102 example of a patchy and complex outflow that has largely been investigated as pollution hot spot in Europe.  
1103 Several studies show the importance of the pollution transport from this area to the surrounding regions (e.g.  
1104 Diémoz et al., 2019a, 2019b) and the complexity of chemical and dynamical processes within the Po Valley  
1105 mixing layer (e.g. Curci et al., 2015). The Alps and Apennines on the Italian Peninsula lead to the transport of  
1106 the Po Valley outflow southwards along the Italian Adriatic coast which is the geographic opening of the Po  
1107 Valley (Finardi et al., 2014). In a dedicated study, the in-situ and remote instruments at ground-based sites and  
1108 airborne measurements from two aircrafts are combined to examine in detail the transport of pollutants during  
1109 the EMERGE IOP for the case Po Valley (Andrés Hernández et al., in preparation 2021).  
1110 When HALO flew over MPC outflows but did not sample them in-situ, the down-looking remote sensing  
1111 instruments on-board enabled the identification of plumes as illustrated in Fig. 27 by using HAIDI measurements  
1112 at 8 km of the Milan outflow during E-EU-09. The measurements of HAIDI were used to estimate emissions and  
1113 plume geometries, NO<sub>2</sub> being an important target species.  
1114 The HAIDI instrument has three scanning telescopes pointed at nadir, 45° forward and 45° backwards direction.  
1115 On the left side of Fig.27, the data from the nadir telescope scanner are shown at high spatial resolution. The  
1116 map shows a strong NO<sub>2</sub> plume Northeast of Milan. The plume substructures are also clearly visible. On the  
1117 right side of the figure, the data from all three telescope scanners are plotted as a function of time at a lower  
1118 spatial resolution. The time delay of about 80 s between the peak as seen in the forward and backward scanners  
1119 indicates that this plume is close to the ground. Wind data from the lowest layer from the ECMWF ERA-5  
1120 reanalysis product [Copernicus Climate Change Service, 2017] implied a wind angle of 23.8°, which is  
1121 consistent with this plume originating from the city of Milan. The estimated NO<sub>2</sub> emission rate of 607± 67  
1122 kg/day may have a higher uncertainty due to the low wind speed (0.6 m/s), the complex plume shape and the  
1123 small relative angle between the HALO flight track and the plume direction.  
1124



1125  
1126 **Figure 27:** HAIDI measurement at 8 km altitude of the Milan outflow during the flight E-EU-09: a) pixel-resolved NO<sub>2</sub> slant  
1127 column densities observed by the nadir camera (marked by the red square on the map). An enhancement of up to  $1.5 \times 10^{16}$   
1128 molec/cm<sup>2</sup> over the background is observed Northeast of Milan (red coloured circle), b) NO<sub>2</sub> slant column densities averaged  
1129 over the whole swath for all three telescopes: forward (top) nadir (middle) and backward (bottom). The height of the plume  
1130 centre is estimated from the time difference of the maxima. Sources of background imagery: ESRI, DigitalGlobe, GeoEye, i-  
1131 cubed, USDAFSA, USGS, AEX, Getmapping, Aerogrid, IGN, IGP, swisstopo, and the GIS User Community.



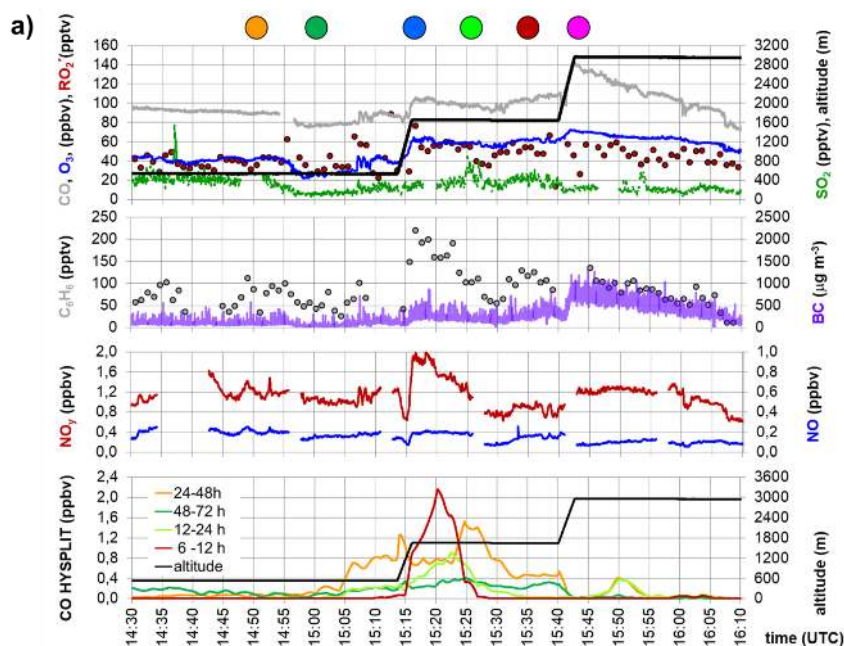


1132 **4.3.2 MPC Madrid and Barcelona**

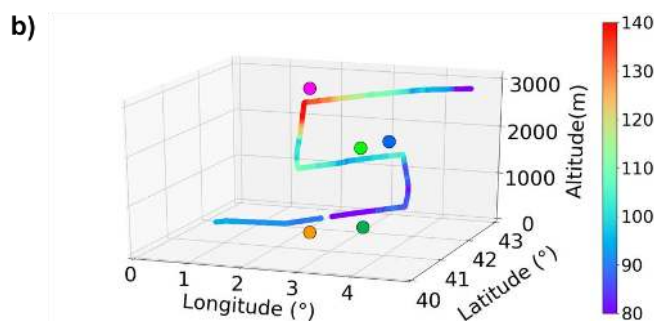
1133 The vertical distribution of pollutants observed at the coast of Barcelona during E-EU-09 is a particular case of  
1134 interest for the study of vertical layering of pollution. HYSPLIT CO dispersion simulations indicate that the  
1135 Madrid outflow was transported over a long distance above the Iberian Peninsula to the North-Eastern coast at  
1136 altitudes above 2000 m while in the lower layers the Barcelona outflow predominated, as illustrated in Fig. 28.

1137 In contrast with the air sampled at 500 m, the backward trajectories and HYSPLIT dispersion calculations  
1138 indicate that the air probed from 15:15 to 15:25 UTC at 1600 m had passed over MPC Barcelona within 6-12  
1139 hour before sampling. There is no indication of fresh NO emissions, and NO<sub>y</sub>, C<sub>6</sub>H<sub>6</sub> and CO are significantly  
1140 higher than at the lower altitude. The layering is attributed to be the result of the recirculation of emissions in the  
1141 Barcelona outflow within the land-breeze regimes close to the coast. Later at this FL (green and red circles in  
1142 Fig. 28), the backward trajectories and HYSPLIT estimations indicate sampling of regional emissions that had  
1143 travelled along the coast from Valencia. This is consistent with the observed decreases in C<sub>6</sub>H<sub>6</sub>, NO<sub>y</sub> and BC. In  
1144 the upper FL at 15:45 UTC, NO<sub>y</sub>, C<sub>6</sub>H<sub>6</sub> and CO significantly increase in air transported from Portugal (as in the  
1145 36 h backward trajectories) across the Iberian Peninsula at altitudes above 2000 m, after PBL contact with the  
1146 MPC Madrid below 1000 m the evening before. According to the pollution control network of Madrid, the  
1147 average CO surface concentration exceeded 350 ppb on the 27 July 2017, the zonal wind direction was WSW  
1148 and the average wind speeds were greater than 16 km/h. The observed mixing ratio decreases when this feature  
1149 at 3000 m disappears. Re-entering and stratification of plumes having different processing along the Spanish  
1150 coast has also been documented in the past (e.g. Millán et al., 1997, 2000 and references therein).

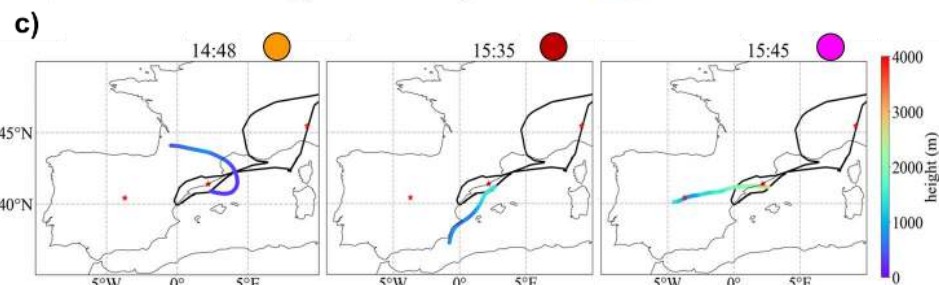
1151



1152



1153



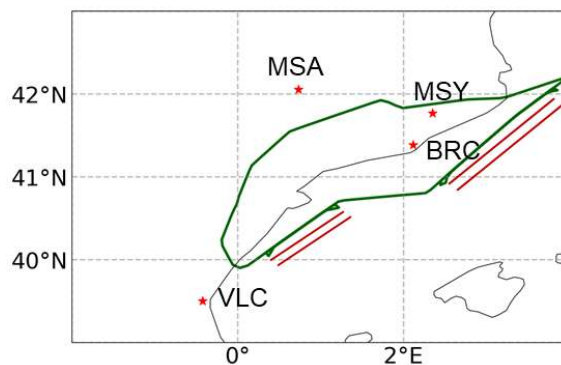
1154

1155 **Figure 28:** Stratified pollution layers along the Spanish coast during the E-EU-09 flight on the 28 July 2017, a) temporal  
 1156 variation of CO, O<sub>3</sub>, RO<sub>2</sub><sup>\*</sup>, NO<sub>y</sub>, NO, SO<sub>2</sub>, C<sub>6</sub>H<sub>6</sub> and BC during the shuttle, b) 3D view of the shuttle colour coded with CO  
 1157 mixing ratios, c) selected backward trajectories (last 24h). Coloured circles marked the corresponding times. Red stars  
 1158 indicate the position of the MPCs of interest.

1159 These HALO measurements are consistent with the long-term analysis of data from the closest four ground-  
 1160 based remote sensing stations available in the framework of EMERGe international. These are data of a lidar in



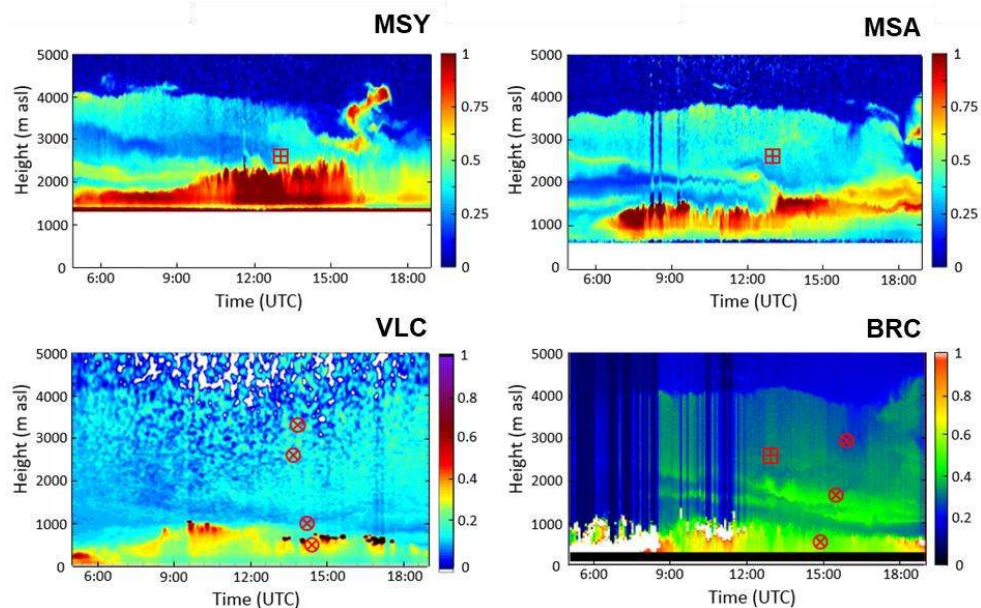
1161 Barcelona (BRC) and three ceilometers in Montseny (MSY), on top of the Serra del Montsec (MSA) (Titos et  
1162 al., 2019) and in Burjassot (VLC) near Valencia. Figure 29 shows the location of the stations with respect to the  
1163 HALO flight track. The stations MSY and MSA were approached at a flight altitude of 2600 m when HALO  
1164 entered the air space above the Iberian Peninsula. Subsequently, HALO shuttles were carried out Northeast of  
1165 Valencia at 500, 1000, 2000 and 2600 m as well as East of Barcelona at 500, 1600 and 3000 m, as presented in  
1166 Fig. 28.



1167

1168 **Figure 29:** Detail of E-EU-F09 flight track (in green) and the ground-based stations with coordinated  
1169 remote sensing measurements in the vicinity: Montseny (MSY), Sierra del Montsec (MSA), Burjassot  
1170 (VLC) and Barcelona (BRC). Red lines indicate the position of the HALO shuttles.

1171 A lofted aerosol layer from above the PBL up to 4000 m altitude was observed at all ground-based remote  
1172 sensing stations and also probed by HALO (see Fig. 30).

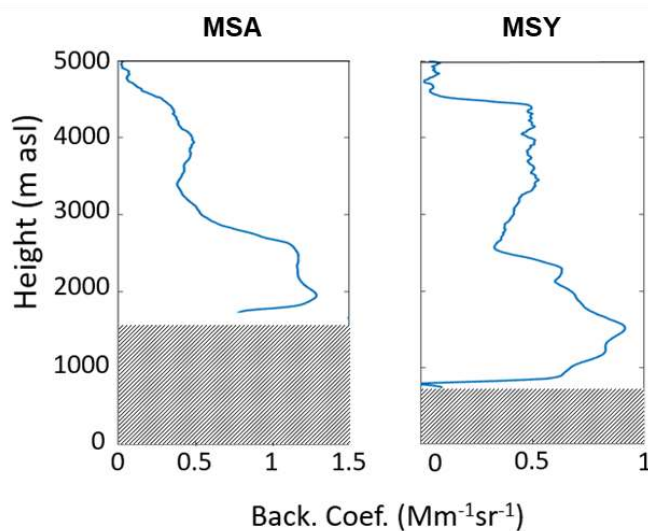


1173

1174 **Figure 30:** Time series of range-corrected lidar signals ground-based remote sensing measurements in MSY, MSA (both at a  
1175 wavelength of 1064 nm), VLC (910 nm) and BRC (532 nm) on the 28 July 2017. Signal strengths relative to the maximum  
1176 signal of the corresponding measurement are depicted. Red circles show time and altitude of the HALO overpasses used for  
1177 comparison of airborne with ground-based remote sensing measurements (see Fig. 31 and Fig. 32). Red squares show further  
1178 HALO overpasses.



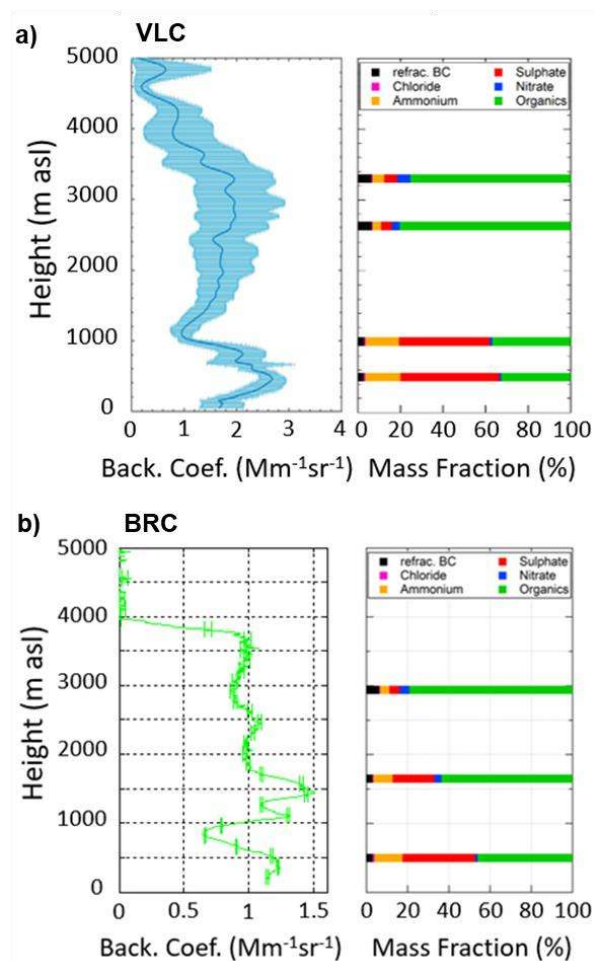
1179 The profiles of the backscatter coefficient derived at MSA, MSY, VLC and BRC on the 28 July 2017 are  
1180 displayed in Fig. 31 and Fig. 32. These measurements illustrate the lofted aerosol layer shown in Fig. 30 with  
1181 increased backscatter coefficients ranging from 0.4 to 1.9 ( $\text{Mm}\cdot\text{sr}^{-1}$ ). The composition of PM1 particles (i.e.,  
1182 with diameter up to 1 micron) was retrieved from the HALO in-situ measurements at different altitudes during  
1183 the shuttles. The observed PM1 composition near Burjassot is shown in Fig. 32. Although the ceilometer  
1184 measurements refer to total aerosol and the in-situ data only to PM1, both reveal two distinct aerosol layers: a)  
1185 a PBL below 1000 m altitude with a backscatter coefficient between 2.0 and 2.7 ( $\text{Mm}\cdot\text{sr}^{-1}$ ) and enhanced  
1186 concentrations of sulphate and ammonium, and b) a lofted aerosol layer between 1500 and 3500 m altitude with  
1187 higher organic, nitrate and BC mass fraction. The difference in composition is likely related to different aerosol  
1188 sources. While the boundary aerosol layer has a local origin, the lofted aerosol layer is influenced by the  
1189 transport of regional emissions. This is consistent with the transport of the MPC Madrid outflow as indicated in  
1190 Fig. 28.



1191

1192 **Figure 31:** Profiles of the backscatter coefficient derived at 1064 nm in MSA and MSY for the 28 July  
1193 2017 from 12:50 to 13:20 UTC. The grey shadings indicate the height of the ceilometers.

1194 Similarly, the lidar and in-situ measurements close to Barcelona reveal a different aerosol composition of the  
1195 PBL below 900 m and a lofted aerosol layer above 2000 m. In addition, a third aerosol layer evolved between  
1196 1000 and 1800 m altitude with a backscatter coefficient up to 1.5 ( $\text{Mm}\cdot\text{sr}^{-1}$ ). The mass fractions of ammonium,  
1197 sulphate and organic aerosol are between the values of those of the PBL and of the lofted aerosol layer above.



1198

1199 **Figure 32:** Distinct aerosol layers observed near Burjassot/Valencia and Barcelona. a) Profile of the backscatter coefficient  
 1200 derived at 910 nm for 13:30-14:30 UTC in VLC (left), and fractional composition of PM1 measured (SP2 and AMS) on-  
 1201 board HALO (right), b) the same derived in BRC at 532 nm for 14:45-15:45 UTC. The periods of comparison with the  
 1202 HALO data are 13:42-13:56 (9:30 min) at 3300 m; 13:34-13:40 (5:30 min) at 2630 m; 14:03-14:14(11:30 min) at 1000 m and  
 1203 14:18-14:31 (23 min) at 500 m for VLC, and 15:43-16:00:(17:30 min) at 2940 m; 15:16-15:40 (24 min) at 1650 m, and  
 1204 14:47-15:14 (27 min) at 500 m for BRC.

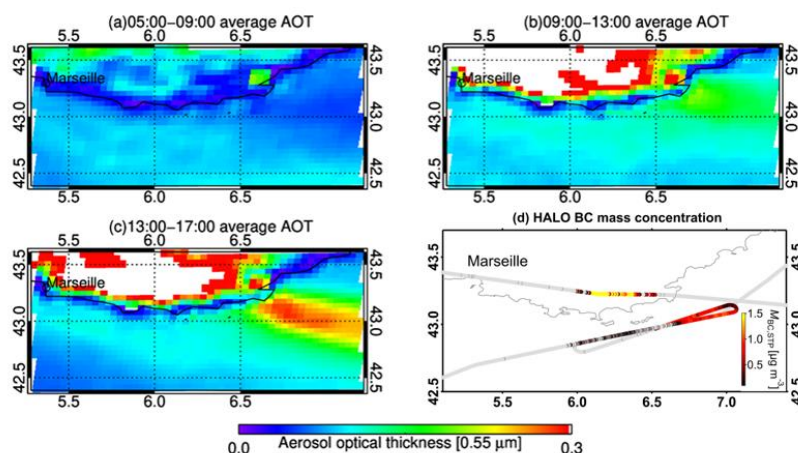
#### 1205 4.4 Specific case studies of mixing of MPC outflows with air masses of biogenic origin: forest fires and 1206 dust

1207 Typically the composition of the measured pollution plumes indicated that emission came from sources other  
 1208 than of the targeted MPCs. These influence the photochemical oxidation and chemical reactions of the probed air  
 1209 masses. Supporting satellite- and ground-based measurements of forest fire and dust signals enable the  
 1210 identification of these sources.



1211 BB emission from fires was e.g. probed during the E-EU-07 flight downwind of Marseille. The plume transport  
1212 eastwards from near Marseille is well-captured by SEVIRI with AOT values around 0.25 at 0.55  $\mu\text{m}$  in the  
1213 afternoon, as shown in Fig. 26. This plume was probed by HALO in-situ measurements at around 11:30 and  
1214 16:30 UTC. As an example of the agreement between remote sensing satellite retrievals and HALO  
1215 observations, BC mass concentrations are also depicted in the figure. The highest BC was measured at roughly  
1216 2000 m and exceeded  $7 \mu\text{g m}^{-3}$ . In the PBL, measured BC mass concentrations were as high as  $1 \mu\text{g m}^{-3}$ . The  
1217 stratification of pollution plumes above the PBL is a typical feature for BB emissions (Holanda et al., 2020).

1218

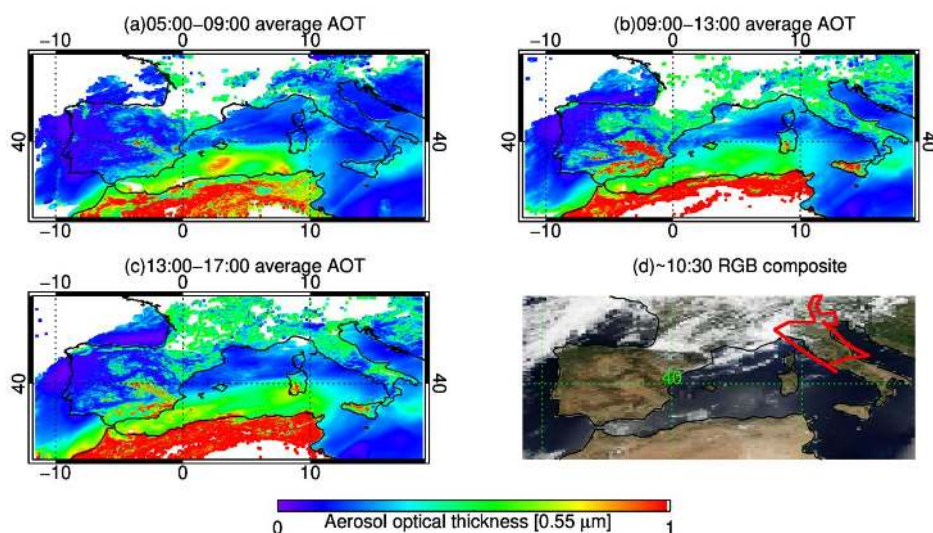


1219

1220 **Figure 33:** (a - c) Aerosol optical thickness at 0.55  $\mu\text{m}$  as retrieved from SEVIRI from 05:00 to 17:00 UTC on 24 July 2017.  
1221 (d) E-EU-07 flight track, colour-coded with BC mass concentration ( $M_{\text{BC}}$ ). For a better contrast, the scale for  $M_{\text{BC}}$  ranges  
1222 from 0.1 to  $1.5 \mu\text{g m}^{-3}$ . Grey colour on the flight track indicates values below  $0.1 \mu\text{g m}^{-3}$ . The mass concentration reached  
1223 values up to  $7 \mu\text{g m}^{-3}$  at the French coast.

1224 Mixing ratios of  $\text{CH}_4$  comparable to those in urban plumes were measured in this BB event during E-EU-07 (not  
1225 shown). This distinct peak concentration strongly influences the local GHG distribution (Klausner, 2020),  
1226 although the contribution of BB emissions to total global anthropogenic  $\text{CH}_4$  is on the order of a few percent  
1227 (Saunois et al., 2019).

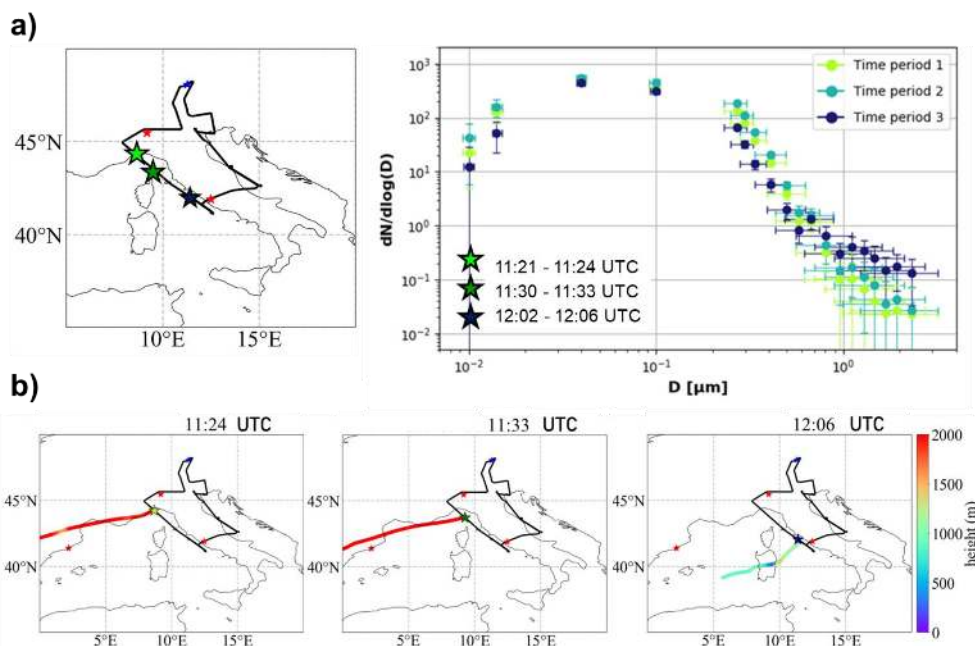
1228 Dust events were observed and contributed significantly to some of the plumes measured over Europe during the  
1229 EMerGe IOP. On 11 July 2017, there was a Saharan dust event affecting the air masses measured during E-EU-  
1230 03, as indicated by both satellite- and ground-based observations. Figure 34 shows the MODIS satellite RGB  
1231 image at 10:30 UTC and the corresponding elevated AOT at 0.55  $\mu\text{m}$  as retrieved from SEVIRI from 09:00 to  
1232 13:00 UTC.



1233

1234 **Figure 34:** (a-c) Aerosol optical thickness at 0.55  $\mu\text{m}$  as retrieved from SEVIRI from 05:00 to 17:00 UTC on 11 July 2017,  
1235 (d) MODIS RGB composite figure showing corrected reflectance at 10:30 UTC (<https://worldview.earthdata.nasa.gov/>). The  
1236 MODIS RGB composite is created combining red, green and blue bands into one picture. White areas are clouds. The E-EU-  
1237 03 flight track (in red) is superimposed on (d).

1238 The impact of dust on the aerosol size distributions observed on board HALO close to the western coast of Italy  
1239 during E-EU-03 is illustrated in Fig. 35. The concentration of particles with a diameter below 250 nm was  
1240 analysed by the Differential Mobility Analyzer (DMA) in 6 steps of 30 s duration, resulting in a period of 3  
1241 minutes for each integrated measurement. The evaluated DMA data points are then combined with the data from  
1242 an Optical Particle Counter (OPC) for particles in the range from 250 nm to 3  $\mu\text{m}$ . The first two sequences in  
1243 Fig. 35 are taken at 2900 m and the third at 1300 m altitude. The third period and lowest in altitude had the  
1244 smallest total number concentration with a clear enhancement of the particles above 600 nm. According to  
1245 FLEXTRA, HALO flew approximately 800 m above the PBL at the time of sampling. The increase in the coarse  
1246 mode particles above the PBL implies mineral dust rather than sea salt. According to backward trajectories, the  
1247 air mass probed had recent contact at altitudes below 1000 m with the dust plumes over the Mediterranean near  
1248 Sardinia shown by MODIS in Fig.34.

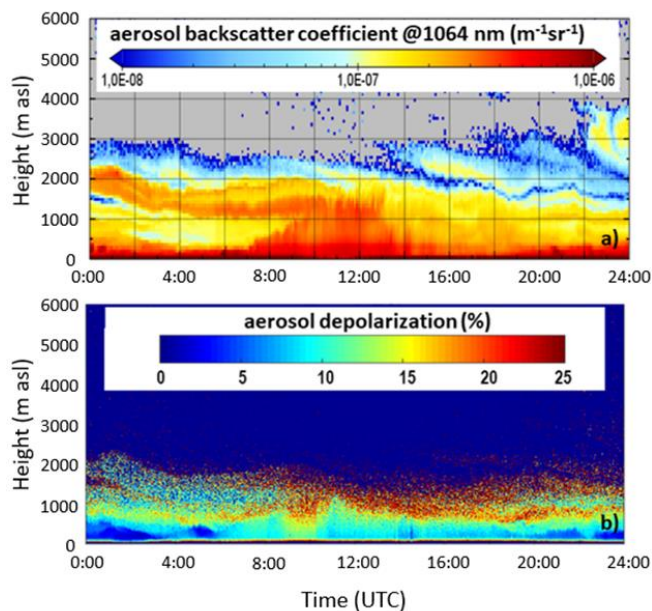


1249

1250 **Figure 35:** Example of the effect of dust plumes on the aerosol concentration during E-EU-03 on the 11 July 2017. a)  
1251 Particle size distribution for 3 selected time periods (right) and position of the sample points in the flight track (left). The  
1252 error bars on the y-axis are the standard deviations of the mean measured concentrations. The error bars in x-direction  
1253 indicate the 16th and 84th percentile of the median diameters of the sensitivities of each size channel, b) 48h backward  
1254 trajectories for the three periods selected. The red stars indicate the position of the MPCs of interest.

1255 These observations agree with the measurement of the continuous automated lidar-ceilometer (ALC) in Rome on  
1256 11 July 2017, which include the overpass by HALO in the Rome area (see Fig. 36). A lofted aerosol layer with  
1257 increased depolarization was detected at an altitude between 1000 and 2000 m from the morning and mixed with  
1258 local particles lifted by PBL dynamics in the middle of the day, at the time of the DMA measurement. This  
1259 indicates that HALO flew above a dust layer during the first two periods of the DMA measurement. Thus,  
1260 HALO probed rather low concentrations of large particles. Subsequently, HALO dived into the dust layer and  
1261 this explains the increase of particles larger than 600 nm.





1262

1263 **Figure 36:** Aerosol profile measurements performed in Rome (Italy) on 11 July 2017 by the Automated Lidar-Ceilometer  
1264 network (ALICENET). Aerosol backscatter coefficient ( $\text{m}^{-1} \text{sr}^{-1}$ ) at 1064 nm (top), and aerosol depolarization in % (bottom).

1265 The comparison of fine and coarse mode particles observed on board the Sky Arrow with aerosol properties at  
1266 the ground provides evidence for the important role of fine particle photo-nucleation in the MPC Rome, favoured  
1267 by high radiation and temperatures (Campanelli et al., 2021; Barnaba et al., 2021 in preparation).

1268 The extent and effect of mixing of air masses of different nature observed during the EMERGe IOP is  
1269 investigated in more detail elsewhere (Förster et al., 2021 in preparation; Holanda et al., in preparation 2021).

## 1270 5 Processing of polluted air masses during transport

1271 Chemical and physical processing of MPC emissions during transport has an important impact on the potential to  
1272 form  $\text{O}_3$  and other secondary photochemical oxidants in the outflows. In addition, photochemical processing  
1273 changes the volatility and hygroscopicity of the aerosol particles and thereby their impact on cloud formation. In  
1274 this sense, the EMERGe airborne observations of primary and secondary pollutants and the ratios between  
1275 species having different chemical lifetime were used as tracers of the degree of processing of the pollution  
1276 plumes probed.

1277 The  $\text{NO}/\text{NO}_y$  ratio provides information about the reactivity of the air mass but is not a reliable chemical clock  
1278 due to the complex and rapid chemistry involved in the air masses investigated. Depending on the chemical and  
1279 physical conditions, the lifetime of NO versus the formation of other reactive nitrogen compounds is of the order  
1280 of a few hours or less. Internal transformation processes within the family of total reactive nitrogen  $\text{NO}_y$  do not  
1281 alter their integrated concentration. However, washout and aerosol formation are loss processes controlling the  
1282 lifetime of  $\text{NO}_y$ , which varies between hours and days.

1283 A more robust chemical clock is the  $\text{NO}_y$  to CO ratio which is generally used to study ageing of an air mass with  
1284 respect to ozone and nitrogen chemistry (e.g. Stohl et al., 2002). The CO lifetime varies between several weeks



1285 and months (e.g. Emmons et al., 2010). Depending on the distance from the source as well as on the chemical  
1286 and physical properties of the air mass, the  $\text{NO}_y/\text{CO}$  ratio declines to background values within a few days. As  
1287 expected within the EMeRGe IOP in Europe, the  $\text{NO}_y/\text{CO}$  values were generally significantly higher for the  
1288 processed polluted plumes than for the background air masses. For instance, during E-EU-08 discussed in Sect.  
1289 4.2, the  $\text{NO}_y$  to CO ratio was of the order of 0.01 to 0.02 in the air sampled outside the outflow of London and  
1290 increased up to 0.1 in the London outflow plumes, as the air mass was processed and mixed.

1291 The ratio between VOCs with comparable emission sources but significantly different chemical lifetimes is often  
1292 used as a chemical clock to study emissions from point sources. This is the case for  $\text{C}_7\text{H}_8$  and  $\text{C}_6\text{H}_6$  emitted from  
1293 gasoline-powered engines used in traffic and industry (Gelencsér et al., 1997; Shaw et al., 2015; Warneke et al.,  
1294 2001). The atmospheric lifetime of these aromatic hydrocarbons, i.e., 1.9 and 9.4 days, respectively (Garzón et  
1295 al., 2015), is assumed to be controlled only by the reaction with OH radicals (Atkinson, 2000). Provided that the  
1296 emission rates are known, the  $\text{C}_7\text{H}_8/\text{C}_6\text{H}_6$  ratio is expected to decrease with increasing distance to the pollution  
1297 source and can be used to estimate the photochemical age of the sampled air (Winkler et al., 2002; Warneke et  
1298 al., 2007). For EMeRGe, the ratio of  $\text{C}_7\text{H}_8/\text{C}_6\text{H}_6$  is a good indicator for the presence of freshly or already  
1299 processed anthropogenic emissions in the probed air. However, since the emission ratios of distinct VOC sources  
1300 vary (Barletta et al., 2005), the active plume mixing before sampling as in EMeRGe, limits the use and  
1301 feasibility of this chemical clock for the determination of the transport time of a specific outflow.

1302 Information about the ageing of the air mass is additionally derived from differences in the chemical  
1303 composition of aerosol particles. Aerosol mass spectrometer data using organic ions containing oxygen, e.g.  
1304  $\text{CO}_2^+$  ( $m/z$  44) and  $\text{C}_2\text{H}_5\text{O}^+$  ( $m/z$  43), are used to assess photochemical oxidation. Observations from laboratory  
1305 and field studies indicate that during photochemical processing the ion signal of  $m/z$  43 decreases while that of  
1306  $m/z$  44 increases (Ng et al., 2010; Lambe et al., 2011). This metric is used to infer the degree of photochemical  
1307 processing of organic aerosol in the atmosphere (e.g., Ng et al., 2011; Schroder et al., 2018; de Sa et al., 2018).  
1308 In that regard, photochemical processing of aerosol particles was evident during the transport of MPC plumes  
1309 during the EMeRGe IOP.

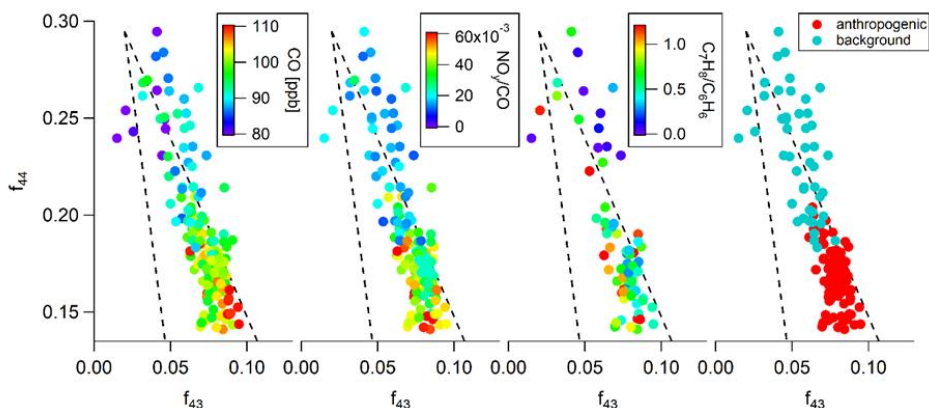
1310 Since photo-oxidation of fresh plumes is fast and mixing of aged plumes with the background occurs, the use of  
1311 aerosol composition to assess photochemical processing requires complementary information from other  
1312 measurements to act as a reliable indicator. Figure 37 shows an example of photochemical processing of the gas  
1313 and the aerosol phases in ageing London plumes as measured by the C-ToF-AMS during E-EU-08. The data are  
1314 plotted in  $f_{44}/f_{43}$  space, where  $f$  denotes the ratio of the respective ion to the total organic ion signal. In these  
1315 metric, atmospheric processing moves the data points towards the upper left corner of the triangle indicated by  
1316 the dotted lines (Ng et al., 2010). The simultaneous measurements of CO are used to indicate dilution, while the  
1317 atmospheric processing is inferred from other gas-phase measurements ( $\text{C}_7\text{H}_8/\text{C}_6\text{H}_6$  and  $\text{NO}_y/\text{CO}$  colour codes).  
1318 Lower CO concentrations due to plume dilution along transport correspond to higher photochemical processing  
1319 in the upper part of the triangle. As  $\text{NO}_y$  has a shorter lifetime than CO, the  $\text{NO}_y/\text{CO}$  ratio indicates that the  
1320 processing is taking place in addition to dilution. Therefore, lower  $\text{NO}_y/\text{CO}$  and  $\text{C}_7\text{H}_8/\text{C}_6\text{H}_6$  ratios in the upper  
1321 part of the triangle indicate aged and processed air. In this case, the FLEXTRA backward trajectories revealed  
1322 that the air masses identified as “background” were transported above the PBL and had no recent contact to the  
1323 MPC London. The anthropogenically influenced air masses represent a mixture of recent emissions and  
1324 photochemically processed London outflow as mentioned in 4.2.2 (see Fig. 24 and Fig. 25).

1325



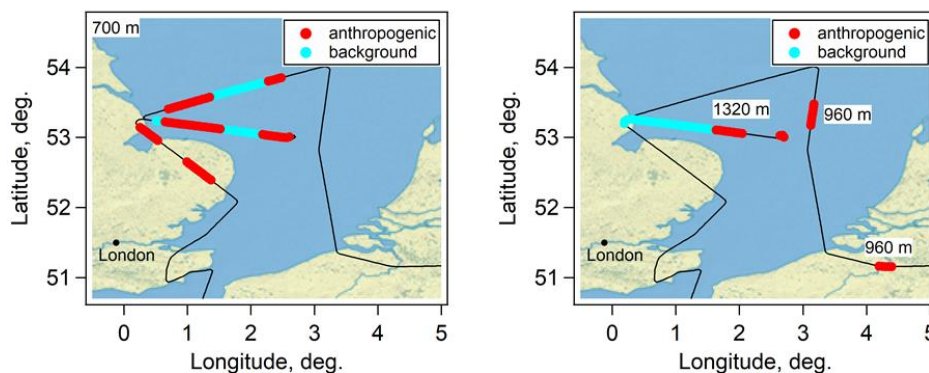
1326

1327 a)



1328

1329 b)



1330

1331 **Figure 37:** a) Scatter plots of C-ToF-AMS signal fractions at  $m/z$  44 ( $f_{44}$ ) and  $m/z$  43 ( $f_{43}$ ) of the London plume measured  
1332 during the E-EU-08 on 26 July 2017 between 10:20 and 12:57 UTC. In this metric, the degree of photochemical processing  
1333 increases to the upper left corner of the triangle which encompasses the range of typical atmospheric observations. The colour  
1334 code indicates dilution (CO) and processing of the gas phase ( $\text{NO}_y$  to CO and  $\text{C}_7\text{H}_8$  to  $\text{C}_6\text{H}_6$  ratios). The right panel shows the  
1335 assignment to unpolluted background air and air masses of anthropogenic polluted origin as introduced in Sect. 4.1. b) Spatial  
1336 distribution of the background and anthropogenic polluted air masses identified in a). The flight altitudes are indicated in the  
1337 graphs.

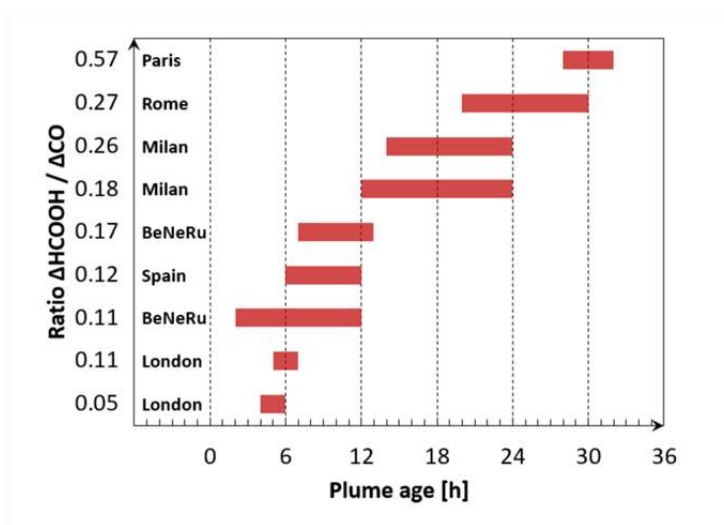
1338 The results presented above confirm the complexity of the air masses as a result of the mixing of sources.

1339 Following the ageing of the outflow of a single MPC is challenging. However, the distinction between fresh and  
1340 aged air is possible and gives a coherent picture for the applied methods and chemical clocks. At large distances  
1341 from the source, the use of gas and aerosol trace species is insufficient for identifying MPC plumes. In this  
1342 context, the relevance of PFC tracers and the support of adequate transport models becomes obvious.

1343 The secondary formation of pollutants as a result of plume processing was further investigated with the support  
1344 of HYSPLIT plume age simulations. An example is formic acid ( $\text{HCOOH}$ ), the most abundant organic acid in  
1345 the troposphere. Although  $\text{HCOOH}$  has primary sources, i.e., the emissions by fossil fuel combustion and  
1346 biomass burning, the secondary formation from gas-phase and aqueous photochemistry has been suggested to be



1347 dominant in the troposphere (Paulot et al., 2011). During EMerGe, HCOOH was measured by CI-ITMS by  
1348 using  $\text{CO}_3^-$  as reactant ion (Viidanoja et al., 1998). Significantly enhanced volume mixing ratios up to 25 ppb  
1349 were observed in the pollution plumes of MPCs in Europe, and HCOOH was found to be more abundant in the  
1350 plumes than sulphur and nitrogen precursor species of inorganic acids (Eirenschmalz et al., in preparation 2021).  
1351 Figure 38 shows HCOOH enhancements above ambient background relative to CO enhancements in different  
1352 MPC plumes as a function of plume age. Here,  $\Delta\text{HCOOH}$  and  $\Delta\text{CO}$  are determined from the measurements, and  
1353 the plume age from HYSPLIT simulations considering CO emissions from EDGAR and the dispersion of the  
1354 plumes during transport. CO is used as an indicator of the strength of emissions from combustion in the  
1355 individual MPC plumes and as tracer for the dilution of the plumes for the actual meteorological conditions  
1356 during the measurements. The  $\Delta\text{HCOOH}$  to  $\Delta\text{CO}$  ratios significantly increase with plume age indicating  
1357 secondary formation of formic acid to be its main source in the MPC plumes, mainly due to oxidation of  $\text{C}_5\text{H}_8$  in  
1358 the plume.



1359

1360 **Figure 38:** Observed enhancements of formic acid ( $\Delta\text{HCOOH}$ ) in MPC plumes relative to observed CO enhancements  
1361 ( $\Delta\text{CO}$ ) as a function of plume age from HYSPLIT simulations. The corresponding city-plume is indicated next to the ratios.

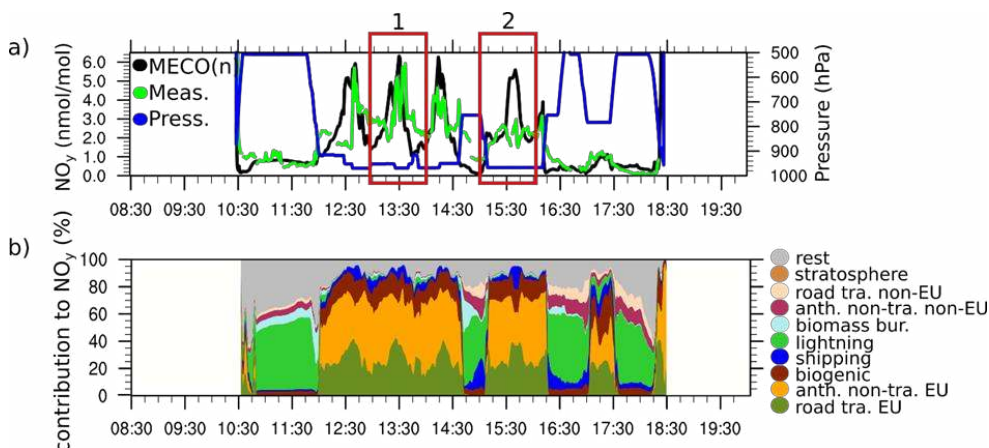
## 1362 6 Simulating the processing of European MPC emissions with the MECO(n) model

1363 Atmospheric modelling is used to place the spatially and temporally limited number of observations during  
1364 EMerGe into a broader context, e.g. by analysing long term trends or temporal and spatial variability in the  
1365 MPC emissions in Europe.

1366 The EMerGe data set offers an opportunity to test whether the transport and transformation of MPC emissions  
1367 are well captured by state-of-the-art atmospheric models. In this context, simulations with the MECO(n) model  
1368 (Kerkweg & Jöckel 2012, Mertens et al., 2016) were performed. The model couples a global and a regional  
1369 chemistry climate model. In the set-up applied here, Central Europe was resolved with up to 7 km horizontal  
1370 resolution. The model data was sampled along the HALO flight paths with 60 s temporal resolution using the  
1371 MESSy submodel S4D (Jöckel et al., 2010). These sampled model data are used for a one-by-one comparison  
1372 with the measurements. The EDGAR 4.3.1 emission inventory for the year 2010 was used.



1373 The tagging method by Grewe et al., (2017) was applied as additional model diagnostics. This method  
1374 decomposes the budget of ozone and ozone related precursors into the contributions of different emission sectors  
1375 (Mertens et al., 2020a). Out of the 12 applied emission categories, land transport (mainly road traffic) in Europe,  
1376 anthropogenic (other than traffic) in Europe, shipping, land transport outside Europe, anthropogenic (other than  
1377 traffic) outside Europe, lightning and biogenic emissions are the most important ones (see Fig. 39b). A detailed  
1378 description of the model and the source apportionment technique are provided in the supplement (see S12).  
1379 The model results show a positive bias in O<sub>3</sub> and a negative bias in CO with respect to the EMERGE  
1380 measurements over Europe. This confirms previous comparisons with other observational data (see Mertens et  
1381 al., 2016, 2020b). Given the complexity of the air masses sampled during EMERGE, the comparison with the  
1382 model results was extended by undertaking different sensitivity studies to investigate the impact of specific set-  
1383 up changes on the simulated mixing ratios.  
1384 An example is given for the E-EU-05 flight on 17 July 2017. The comparison between measured NO<sub>y</sub> mixing  
1385 ratios and MECO(n) results is shown in Fig. 39a, when the London plume was probed over the English Channel.  
1386 The enhancements of NO<sub>y</sub> between 12 and 16 UTC below 900 hPa are reasonably well simulated by the model  
1387 except for the measurements at around 15:30 UTC which are strongly overestimated by the model. To address  
1388 this issue, two plumes marked with '1' and '2' in Fig. 39a were investigated in more detail.

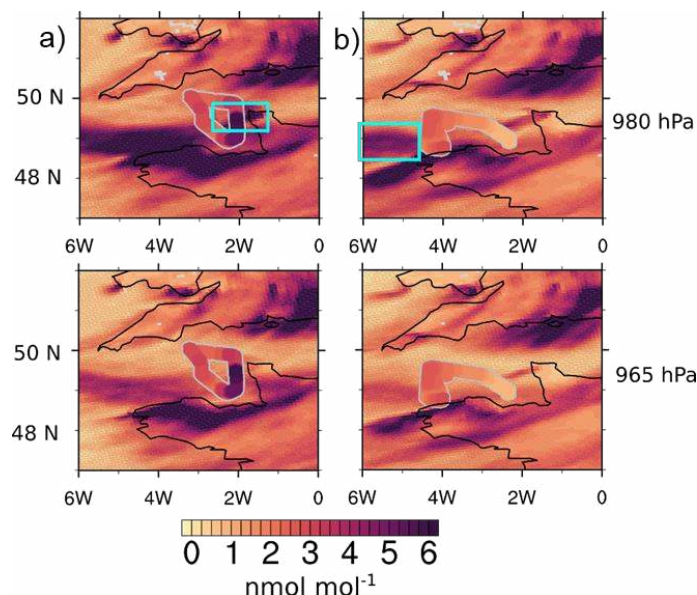


1389  
1390 **Figure 39:** a) NO<sub>y</sub> mixing ratios measured (green) and simulated by the MECO(n) model (black) for E-EU-05 on 17 July  
1391 2017. The blue line denotes the pressure altitude of the aircraft (right axis). b) Relative contributions of different emission  
1392 sectors to the NO<sub>y</sub> mixing ratios simulated by MECO(n). Note that the NO<sub>y</sub> measurements were averaged to 60 s to fit the  
1393 MECO(n) temporal resolution.

1394 The model results and the measurements on the plume marked '1' are shown at 980 hPa and 965 hPa in Fig. 40a.  
1395 980 hPa is the pressure of the model layer which is nearest to the HALO flight altitude at 13:30 UTC while 965  
1396 hPa is pressure of one model layer above. The model results show large horizontal and vertical inhomogeneities  
1397 in the NO<sub>y</sub> mixing ratios indicating different mixtures instead of a single London plume. The NO<sub>y</sub> enhancement  
1398 coincides with the London plume (marked with the turquoise square in Fig. 40a).  
1399 Similarly, Figure 40b shows the model results and measurements for the plume marked '2'. Here, the model  
1400 shows a large plume remanence in the western part (turquoise square in Fig. 40b) leading to the overestimation  
1401 of mixing ratios around 15:30 UTC. The simulated mixing ratios in a higher model layer are lower and agree



1402 better with the observations. These results indicate that a vertical displacement of the plume remanence causes  
1403 the mismatch between measurements and model results around 15:30 UTC.  
1404



1405

1406 **Figure 40:**  $\text{NO}_y$  mixing ratios as simulated by MECO(n) (background) and measured during E-EU-05. The model results at  
1407 980 hPa and 965 hPa are shown. Model results are averaged between a) 13 and 14 UTC, b) 15 and 16 UTC. The measured  
1408 mixing ratios of  $\text{NO}_y$  during 13-14 UTC and 15-16 UTC are colour-coded and highlighted by grey contours. Black lines  
1409 indicate coast lines. The turquoise rectangles highlight the regions discussed in the text.

1410 The agreement between the measurements and model results shows that the emissions of  $\text{NO}_x$  and/or their  
1411 further processing in the model (deposition, washout, chemical transformation) are reasonably well represented  
1412 by MECO(n). However, the simulation of complex plume structures would benefit from a higher model spatial  
1413 resolution.

1414 The diagnostic capabilities of MECO(n), e.g. the tagging method, were applied to individual EMerGe flight  
1415 tracks to provide a better understanding of the impact of emissions on the atmospheric chemistry in Europe.  
1416 Figure 39b shows the relative contribution of the different emission sectors to the measured  $\text{NO}_y$  mixing ratios  
1417 during the E-EU-05 as a stacked graph. According to this, emissions from European road transport,  
1418 anthropogenic non-traffic and biogenic sectors dominate the  $\text{NO}_y$  mixing ratios of the London plume with a  
1419 similar relative contribution in all four plume crossings. For the  $\text{NO}_y$  measurements in the free troposphere (until  
1420 12 UTC approximately) a large relative contribution of lightning emissions is calculated in the model. In these  
1421 regions, however, the absolute mixing ratios are rather low. As the  $\text{NO}_y$  lifetime is much longer in the upper  
1422 troposphere than in the PBL, LRT of  $\text{NO}_y$  might be more likely than encounters of fresh lightning  $\text{NO}$ -plumes.

1423 The MECO(n) model was further evaluated within EMerGe by similar analysis with different measured  
1424 chemical species and emission inventories. The combination of the MECO(n) results with HYSPLIT backward  
1425 trajectories provides good insights into the uncertainty of the model-based estimates of the origin of the air  
1426 masses probed.



## 1427 7 Summary

1428 The present article provides an overview on some of the scientific achievements obtained within the EMeRGe  
1429 IOP in Europe.

1430 The EMeRGe campaign in Europe focused on the identification and measurement of the plumes of pollution  
1431 from selected MPCs, i.e. their emissions, transport and transformation. EMeRGe achieved its measurement  
1432 objectives by exploiting the unique capabilities of the HALO research platform to probe these plumes over a  
1433 relatively large geographical coverage and by the use of forecasting models and tools.

1434 The results obtained from EMeRGe provide new insights into the transport and transformation of pollution  
1435 plumes over Europe during the IOP in July 2017:

- 1436 • EMeRGe provides a unique set of in-situ and remote sensing airborne measurements of trace gases and  
1437 aerosol particles along flight routes in the lower troposphere over Europe. The interpretation of the HALO  
1438 measurement data is facilitated by the use of collocated ground-based and satellite measurements. In that  
1439 respect, EMeRGe enhances previous pollution studies in Europe by adding an extensive experimental data  
1440 set in the PBL.
- 1441 • The selected MPCs are confirmed as pollution hot-spots by analysis using the aircraft measurements,  
1442 backward and forward trajectories, dispersion models, CAMS tracer simulations and satellite observations.
- 1443 • Distinct aerosol layering is observed over some of the investigated MPCs. Collocated ground-based remote  
1444 sensing instruments improved vertical and temporal resolution as compared to HALO. The synergetic use  
1445 of these data improves the understanding of the evolution of the airborne observed scenarios and the  
1446 attribution of the vertical distribution of pollutants probed during the shuttles flights.
- 1447 • Plumes originating from European MPC outflows are typically observed below the top of the BL at 2000 m  
1448 and occasionally after being transported over long distances. The location and position of the city plumes  
1449 are typically well forecasted by the CAMS-global, MECO(n) regional and by HYSPLIT dispersion  
1450 simulations using urban city tracers.
- 1451 • The composition of the pollution plumes measured along the flight tracks depend on the MPC emissions  
1452 and the mixing with air from other emission sources. Enhancements in the concentration of selected  
1453 species, such as CO, NO<sub>y</sub> and VOCs such as C<sub>6</sub>H<sub>6</sub> and CH<sub>3</sub>CN measured on-board HALO, enable the  
1454 identification of anthropogenic and BB signatures in the plumes.
- 1455 • Isotope measurements in VOC samples collected at MPC ground sites and on-board HALO enable the  
1456 determination of atmospheric residence times and the source apportionment. Different ranges of δ<sup>13</sup>C  
1457 values in VOCs are determined and attributed to MPC sources, e.g. for C<sub>6</sub>H<sub>6</sub> in the Po Valley and Rome for  
1458 the first time.
- 1459 • Signatures of urban sources of long-lived greenhouse gases like CH<sub>4</sub> and CO<sub>2</sub> are identified in the airborne  
1460 measurements in plumes close to the MPC regions in Europe. The identification of plumes of GHG and the  
1461 quantification of the MPC contributions to the regional GHG budget are challenging. This results from the  
1462 long lifetime of these gases which yields a well-mixed and large atmospheric background, and the distance  
1463 from the MPC to the sampling.
- 1464 • The aerosol inside the MPC plumes is typically dominated by smaller particles which are clearly visible in  
1465 the total aerosol number concentration for the aerosol radius in the range 0.01 to 3 μm.



- 1466 • Tagging of polluted air masses in the centre of MPCs by ground-based releases of PFC tracers provides a  
1467 unique opportunity to identify successfully and unambiguously MPC outflows after transport times of  
1468 between 5 and 26 hours. The tracer experiments during EMeRGe additionally test the ability of models  
1469 (HYSPLIT, FLEXPART, FLEXPART-WRF, FALL3D) to simulate the transport and dispersion of the  
1470 tracer for different meteorological conditions and topography around the release sites. While the simulated  
1471 position of the PFC plumes agrees with the measurements, the tracer mixing ratios calculated by the  
1472 dispersion models are by a factor 2 to 3 higher than detected. The degree of agreement between the tracer  
1473 simulations and observations depends on the parametrisation of dispersion and the representation of the  
1474 topography in the models, as well as the goodness of tracer sampling in the plume, e.g. matching the  
1475 maximum PFC concentrations was not always possible due to restrictions by air traffic control and flight  
1476 endurance. EMeRGe is one of the first airborne measurement campaigns to use this air mass tracer  
1477 approach and has successfully demonstrated its value.
- 1478 • Regional transport of several European MPC outflows is successfully identified and measured: a) London  
1479 over the English Channel to Central Europe, b) Po Valley either North over the Alps or in a south-easterly  
1480 direction towards the Adriatic, c) Rome over the Apennines into the Adriatic and d) Madrid and Barcelona  
1481 into the Western Mediterranean.
- 1482 • BB emissions mix frequently with anthropogenic pollution during the transport over Europe. BB signatures  
1483 are encountered in a large fraction of the pollution plumes probed during the EMeRGe IOP.
- 1484 • BB also contributes significantly to the concentration of pollutants above the PBL and represents an  
1485 important particle source over Europe, in addition to urban, industrial emissions and mineral dust. BB  
1486 observed during EMeRGe at altitudes above 5000 m is attributed to be in older masses, which had  
1487 originated in North American fires, in agreement with models.
- 1488 • Mineral dust is identified in the aerosol size distribution and the optical properties of some of the air masses  
1489 probed in Southern Europe above the PBL, in agreement with space and ground-based observations.
- 1490 • The photochemical activity as indicated by the presence of free radicals varies widely in the plumes. The  
1491 largest peroxy radical,  $RO_2^*$ , mixing ratios are observed below 3000 m in Southern Europe. This is  
1492 expected and results from higher insolation and temperatures, which accelerate the photochemical  
1493 processing. The  $O_3$  production rates calculated from the  $RO_2^*$  measured on-board are in the same order of  
1494 magnitude as those reported in urban pollution for mixing ratios of  $NO < 1$  ppbv.
- 1495 • HONO mixing ratios detected in the PBL and lower part of the free troposphere often exceed mixing ratios  
1496 expected from known gas-phase reactions as indicated by comparisons with model simulations. Potential  
1497 mechanisms for the heterogeneous HONO formation are explored using theoretical studies in combination  
1498 with the gas-phase, aerosol composition and radiation observations
- 1499 • The photochemical processing of the MPC outflows during transport is inferred from the airborne  
1500 measurements. Ratios of species such as  $NO/NO_y$ ,  $NO/VOC$  and  $C_7H_8/C_6H_6$  and observations of oxidation  
1501 proxies such as peroxy radical concentrations and organic aerosol composition indicate with reasonable  
1502 agreement that chemical processing of the MPC emissions identified during EMeRGe was substantial.  
1503 Measurements of  $\delta^{13}C$  isotopes survey the chemical processing of MPC London plumes and of the MPC  
1504 Rome outflow during the transit over the Apennines.
- 1505 • The analysis of the aerosol composition during EMeRGe indicates that aerosol photochemical processing is  
1506 fast under European summer conditions. Chemical processing modifies both the chemical properties and





1507 the partitioning between gas and particle phase in the air masses over Europe. Simultaneous measurements  
1508 of organic ions, CO and  $C_7H_8/C_6H_6$  and  $NO_3/CO$  ratios on-board enable dilution and processing in the  
1509 plumes to be discriminated.

- 1510 • PFC tracers and adequate transport models are shown to be of indispensable value to quantify the  
1511 processing of MPC plumes at large distances from the sources. Mixing of plumes from the release to the  
1512 observation limits the application of VOC clocks, such as the ratio of  $C_7H_8$  to  $C_6H_6$ , for the investigation of  
1513 the transformation of MPC outflows on large scales.
- 1514 • The precise knowledge of the transport times between the source regions and the HALO sampling sites in  
1515 the plumes obtained from the PFC experiments and dispersion models enables the analysis of chemical  
1516 transformations during transport, e.g. oxidation of  $SO_2$  and formation of HCOOH. The photochemical  
1517 formation of HCOOH is shown to be the main source of HCOOH during the EMerGe IOP in Europe.  
1518 HCOOH is found to be more abundant in the plumes than the precursor species of inorganic acids,  $NO_2$  and  
1519  $SO_2$ .
- 1520 • Secondary organic aerosol prevails in the polluted air masses probed in Europe above 2000 m. In the free  
1521 troposphere above 4000 m the direct effect of anthropogenic emissions on the organic and inorganic  
1522 aerosol components is observed to be small.

1523 First efforts to simulate observations of the EMerGe flight tracks were made with the global/regional  
1524 chemistry-climate model MECO(n). Further investigation of small-scale effects by complementary model  
1525 activities with validated data includes the development of a box model to account for fast chemical  
1526 transformation of pollution in air masses along the flight tracks. The EMerGe set of airborne data supports  
1527 photochemical transport models to assess:

- 1528 • the relative contribution of biogenic, BB and anthropogenic sources to the VOC burden over Europe,
- 1529 • the net ozone production in the investigated MPC outflows in relation to the transport time and mixing of  
1530 the pollution plumes,
- 1531 • the contribution of VOC species such as glyoxal and/or methylglyoxal to secondary aerosol formation in  
1532 aged pollution plumes,
- 1533 • the adequacy of Angstrom coefficients, aerosol fine mode fraction products and the geostationary satellite  
1534 derived AOT to identify aerosol sources and transport features of mixing events of anthropogenic particles  
1535 and mineral dust, and
- 1536 • the significance and representativeness of the transport and concentration patterns obtained during  
1537 EMerGe in summer 2017, which was a period with anomalous meteorological conditions in Central  
1538 Europe.

1539 The collected data during EMerGe help to improve the current understanding of the complex spatial distribution  
1540 of trace gases and aerosol particles resulting from mixing, transport and transformation of pollution plumes over  
1541 Europe. The wide range of observations presented here is the basis for further work being addressed within  
1542 dedicated studies. More detailed analyses of individual data sets are provided elsewhere. Prospective  
1543 deployments of similar characteristics are desirable to consolidate and contextualise the EMerGe results in  
1544 Europe.

1545 The analysis of the EMerGe data obtained in the second IOP in Asia will be presented in separate publications.  
1546



## 1547 Acknowledgements

1548 The authors thank the following teams and individuals, without whom the EMeRGe in Europe IOP would not have been  
1549 possible:

1550 • HALO flight organisation, permissions and related  
1551 the DLR-FX and the HALO EMeRGe team. Special thanks to Lisa Kaser, Frank Probst, Michael Großrubatscher, Stefan  
1552 Grillenbeck, Marc Puskeiler, for flight coordination and planning, to Alexander Wolf, and Thomas Leder, the flight  
1553 engineers and to the BAHAMAS team. The authors also thank enviscope GmbH in particular of Nicole Brehm and Rolf  
1554 Maser for the support during the integration and preparation phase of the IOP in Europe.

1555 • Meteorological and chemical composition forecasting  
1556 Michael Gauss and Álvaro Valdebenito (MetNo) for provision of EMEP forecasts for the campaign and  
1557 CAMS/ECMWF, in particular Johannes Flemming and Luke Jones for providing the weather and trace constituent  
1558 forecasts for the field campaign support. The CAMS-regional modelling team are also acknowledged for providing  
1559 regional model forecast data for Europe.

1560 • LIDAR Observations  
1561 EARLINET for providing aerosol LIDAR measurements and DWD, ALICE-net and RMI for ceilometer measurements.  
1562 The support from AERONET, Service National d'Observation PHOTONS/ AERONET-EARLINET part of the  
1563 ACTRIS-France research infrastructure and GOA-CF, part of ACTRIS-Spain, for their continuous efforts in providing  
1564 high-quality measurements and products, and in particular of all PIs and Co-PIs of the AERONET sites contributing to  
1565 EMeRGe for maintaining their instruments and providing their data to the community is greatly appreciated.

1566 • Luca Ferrero (GEMMA and POLARIS Research Centers, Department of Earth and Environmental Sciences, University  
1567 of Milano-Bicocca) for the air samples collected at the ground in Milan (Italy) during the HALO flights.

1568 • Tracer releases  
1569 Jonathan E. Murray and Helen Graven and the Imperial College team for releasing the PFC tracer in London.

1570 KK and JohS would like to thank Christiane Schulz and Philipp Schuhmann for support during the integration phase. BAH,  
1571 OOK, CP, DW, UP and MLP would like to thank Thomas Klimach, Björn Nilius, Jorge Saturno, Oliver Lauer and Meinrad  
1572 Andreae for support during the EMeRGe campaign in Europe and during the data analysis.

1573 MDAH, MG, YL and JPB thank Wilke Thomssen for support during the preparation and integration phases of EMeRGe and  
1574 Heiko Schellhorn for continuous technical support and retrieval of model data during the campaigns.

## 1575 Funding information

1576 The HALO deployment during EMeRGe was funded by a consortium comprising the German Research  
1577 Foundation (DFG) Priority Program HALO-SPP 1294, the Institute of Atmospheric Physics of DLR, the Max  
1578 Planck Gesellschaft (MPG) and the Helmholtz-Gemeinschaft.

1579 FK, BS, and KP acknowledge the support given by the DFG through the projects PF 384-16, PF 384-17 and PG  
1580 385-19. KB acknowledges additional funding from the Heidelberg Graduate School for Physics. JohS, KK, and  
1581 SB acknowledge funding through the DFG, project No. 316589531. LE and HS acknowledge support by DFG  
1582 through project MEPOLL (SCHL1857/4-1). AH would like to thank DAAD and DLR for a Research  
1583 Fellowship. HS acknowledge financial support by the DLR TraK (Transport and Climate) project. MS  
1584 acknowledges support from the EU (GA no. 654109, 778349, 871115 and 101008004) and the Spanish  
1585 Government (ref. CGL2017-90884-REDT, PID2019-103886RB-I00, RTI2018-096548-B-I00 and MDM-2016-  
1586 0600).

1587 MG, YL, MDAH and JPB acknowledge financial support from the University of Bremen. FLEXPART  
1588 simulations were performed on the HPC cluster Aether at the University of Bremen, financed by DFG within the  
1589 scope of the Excellence Initiative. A.-M. Blechschmidt was partly funded through the CAMS-84 project.

1590 JW acknowledges support from the German Federal Ministry for Economic Affairs and Energy – BMWi (project  
1591 Digitally optimized Engineering for Services – DoEfs; contract no. 20X1701B)

1592 TK thanks DLR VO-R for funding the young investigator research group “Greenhouse Gases”.

1593 MM, PJ, MK acknowledge resources of the Deutsches Klimarechenzentrum (DKRZ) granted by the WLA  
1594 project ID bd0617 for the MECO(n) simulations and the financial support from the DLR projects TraK  
1595 (Transport und Klima) and the Initiative and Networking Fund of the Helmholtz Association through the project  
1596 “Advanced Earth System Modelling Capacity” (ESM).

1597 BAH acknowledges the funding from Brazilian CNPq (process 200723/2015-4).

1598



1599 **References**

- 1600 AERONET: AERONET aerosol data base, available at: <http://aeronet.gsfc.nasa.gov/>, last access: 11 December  
1601 2020
- 1602 Alfarrá, M. R., Prevoť, A. S. H., Szidat, S., Sandradewi, J., Weimer, S., Lanz, V. A., Schreiber, D., Mohr, M., and  
1603 Baltensperger, U.: Identification of the mass spectral signature of organic aerosols from wood burning emissions,  
1604 *Environ. Sci. Technol.*, 41, 5770–5777, doi.org/10.1021/es062289b, 2007.
- 1605 Alvarado, L. M. A., Richter, A., Vrekoussis, M., Hilboll, A., Kalisz Hedegaard, A. B., Schneising, O., and  
1606 Burrows, J. P.: Unexpected long-range transport of glyoxal and formaldehyde observed from the Copernicus  
1607 Sentinel-5 Precursor satellite during the 2018 Canadian wildfires, *Atmos. Chem. Phys.*, 20, 2057–2072, 2020.
- 1608 Andreae, M. O., and Rosenfeld, D.: Aerosol–cloud–precipitation interactions. Part I. The nature and sources of  
1609 cloud-active aerosols, *Earth-Science Reviews* 89, 13–41, 2008.
- 1610 Andreae, M. O., Afchine, A., Albrecht, R., Holanda, B. A., Artaxo, P., Barbosa, H. M. J., Borrmann, S.,  
1611 Cecchini, M. A., Costa, A., Dollner, M., Fütterer, D., Järvinen, E., Jurkat, T., Klimach, T., Konemann, T., Knote,  
1612 C., Krämer, M., Krisna, T., Machado, L. A. T., Mertes, S., Minikin, A., Pöhlker, C., Pöhlker, M. L., Pöschl, U.  
1613 Rosenfeld, D., Sauer, D., Schlager, H., Schnaiter, M., Schneider, J., Schulz, C., Spanu, A., Sperling, V. B.,  
1614 Voigt, C., Walser, A., Wang, J., Weinzierl, B., Wendisch, M., Ziereis, H.: Aerosol characteristics and particle  
1615 production in the upper troposphere over the Amazon Basin. *Atmos. Chem. Phys.*, 18, 921–961, doi:  
1616 10.5194/acp-18-921-2018, 2018.
- 1617 Andreae, M. O.: Emission of trace gases and aerosols from biomass burning – an updated assessment, *Atmos.*  
1618 *Chem. Phys.*, 19, 8523–8546, doi.org/10.5194/acp-19-8523-2019, 2019.
- 1619 Ashworth, K. et al, Megacity and local contributions to regional air pollution: an aircraft case study over  
1620 London, *Atmos. Chem. Phys.*, 20, 7193–7216, doi:10.5194/acp-20-7193-2020, 2020
- 1621 Atkinson, R.: Atmospheric chemistry of VOCs and NO<sub>x</sub>, *Atmospheric Environment*, 34, 2063–2101, 2000.
- 1622 Barnaba, F. and Gobbi, G. P., Aerosol seasonal variability over the Mediterranean region and relative impact of  
1623 maritime, continental and Saharan dust particles over the basin from MODIS data in the year 2001. *Atmos.*  
1624 *Chem. Phys.*, 4, doi:10.5194/acpd-4-4285-2004, 2004.
- 1625 Barnaba, F., Angelini, F., Curci, G., and Gobbi, G.P.: An important fingerprint of wildfires on the European  
1626 aerosol load, *Atmos. Chem. Phys.*, 11, 10487–10501, doi: 105194/acp-11-10487-2011, 2011.
- 1627 Beekmann, M., Prévôt, A. S. H., Drewnick, F., Sciare, J., Pandis, S. N., Denier van der Gon, H. A. C., Crippa,  
1628 M., Freutel, F., Poulain, L., Gheri, V., Rodriguez, E., Beirle, S., Zotter, P., von der Weiden-Reinmüller, S.-L.,  
1629 Bressi, M., Fountoukis, C., Petetin, H., Szidat, S., Schneider, J., Rosso, A., El Haddad, I., Megaritis, A., Zhang,  
1630 Q. J., Michoud, V., Slowik, J. G., Moukhtar, S., Kolmonen, P., Stohl, A., Eckhardt, S., Borbon, A., Gros, V.,  
1631 Marchand, N., Jaffrezo, J. L., Schwarzenboeck, A., Colomb, A., Wiedensohler, A., Borrmann, S., Lawrence, M.,  
1632 Baklanov, A., and Baltensperger, U.: In situ, satellite measurement and model evidence on the dominant regional  
1633 contribution to fine particulate matter levels in the Paris megacity, *Atmos. Chem. Phys.*, 15, 9577–9591,  
1634 <https://doi.org/10.5194/acp-15-9577-2015>, 2015. Beirle, S., Borger, C., Dörner, S., Li A., Hu, Z., Liu, F., Wang,  
1635 Y., Wagner, T.: Pinpointing nitrogen oxide emissions from space, *Sci. Adv.* 2019, 5, eaax9800 13 November  
1636 2019.
- 1637 Boeke, N. L., Marshall, J. D., Alvarez, S., Chance, K. V., Fried, A., Kurosu, T. P., Rappenglück, B., Richter, D.,  
1638 Walega, J., Weibring, P. and Millet, D.B.: Formaldehyde columns from the Ozone Monitoring Instrument:  
1639 Urban versus background levels and evaluation using aircraft data and a global model, *J. Geophys. Res.*, 116,  
1640 D05303, doi:10.1029/2010JD014870, 2011.



- 1641 Bohn, B., and Lohse, I.: Calibration and evaluation of CCD spectroradiometers for ground-based and airborne  
1642 measurements of actinic flux densities, *Atmos. Meas. Tech.*, 10, 3151–3174, doi:10.5194/amt-10-3151-2017,  
1643 2017.
- 1644 Bond, T.C., Doherty, S.J., Fahey, D.W., Forster, P.M., Berntsen, T., DeAngelo, B.J., Flanner, M.G., Ghan, S.,  
1645 Kärcher, B., Koch, D., Kinne, S., Kondo, Y., Quinn, P.K., Sarofim, M.C., Schultz, M.G., Schulz, M.,  
1646 Venkataraman, C., Zhang, H., Zhang, S., Bellouin, N., Guttikunda, S.K., Hopke, P.K., Jacobson, M.Z., Kaiser,  
1647 J.W., Klimont, Z., Lohmann, U., Schwarz, J.P., Shindell, D., Storelvmo, T., Warren, S.G., and Zender, C.S.:  
1648 Bounding the role of black carbon in the climate system: A scientific assessment, *Journal of Geophysical*  
1649 *Research: Atmospheres*, Vol. 118, 5380–5552, doi: 10.1002/jgrd.50171, 2013.
- 1650 Brands, M., M. Kamphus, T. Böttger, J. Schneider, F. Drewnick, A. Roth, J. Curtius, C. Voigt, A. Borbon, M.  
1651 Beekmann, A. Bourdon, T. Perrin, and S. Borrmann: Characterization of a Newly Developed Aircraft-Based  
1652 Laser Ablation Aerosol Mass Spectrometer (ALABAMA) and First Field Deployment in Urban Pollution  
1653 Plumes over Paris During MEGAPOLI 2009, *Aerosol Sci. Technol.*, 45, 46–64, doi:  
1654 10.1080/02786826.2010.517813, 2011.
- 1655 Bréon, F.M., Vermeulen, A., and Descloitres J.: An evaluation of satellite aerosol products against sun  
1656 photometer measurements. *Remote Sensing of Environment*, doi:10.1016/j.rse.2011.06.017, 2011.
- 1657 Bréon, F.M., Broquet, G., Puygrenier, V., Chevallier, F., Xueref-Remy, I., Ramonet, M., Dieudonné, E., Lopez,  
1658 M., Schmidt, M., Perrussel, O., and Ciais, P.: An attempt at estimating Paris area CO<sub>2</sub> emissions from  
1659 atmospheric concentration measurements, *Atmos. Chem. Phys.* 2015, 15 (4), 1707–1724. DOI: 10.5194/acp-15-  
1660 1707-2015.
- 1661 Brito, J., and Zahn, A.: An unheated permeation device for calibrating atmospheric VOC measurements, *Atmos.*  
1662 *Meas. Tech.*, 4(10), 2143–2152, doi: 10.5194/amt-4-2143-2011, 2011.
- 1663 Burrows, J.P., Richter A., Dehn A., Deters B., Himmelmann S., Voigt S. and Orphal J.: Atmospheric remote  
1664 sensing reference data from GOME: Part 2 temperature dependent absorption cross-sections of O<sub>3</sub> in the 231–794  
1665 nm range, *Journal of Quantitative Spectroscopy and Radiative Transfer*, Volume: 61 Issue: 4, 509–517, 1999.
- 1666 Butler, T. M., and Lawrence, M. G.: The influence of megacities on global atmospheric chemistry: A modelling  
1667 study, *Environ. Chem.*, 6 (3), 219– 225. 2009.
- 1668 Butler, T.M., Stock, Z.S., Russo, M.R., Denier van der Gon, H.A.C., and Lawrence, M.G.: Megacity ozone air  
1669 quality under four alternative future scenarios. *Atmos. Chem. Phys.*, 12, 4413–4428, doi:10.5194/acp-12-4413-  
1670 2012, 2012.
- 1671 Campos Braga, R., Rosenfeld, D., Weigel, R., Jurkat, T., Meinrat O. Andreae, M.O., Wendisch, M., Pöschl, U.,  
1672 Voigt, C., Mahnke, C., Borrmann, S., Albrecht, R.I., Molleker, S., Vila, D.A., Machado, L.A.T., and Grulich, L.:  
1673 Further evidence for CCN aerosol concentrations determining the height of warm rain and ice initiation in  
1674 convective clouds over the Amazon basin, *Atmos. Chem., Phys.*, 17, 14433–14456, [https://doi.org/10.5194/acp-](https://doi.org/10.5194/acp-17-14433-2017)  
1675 [17-14433-2017](https://doi.org/10.5194/acp-17-14433-2017), 2017.
- 1676 Cassiani, M., Stohl, A., and Eckhardt S.: The dispersion characteristics of air pollution from world’s megacities,  
1677 *Atmospheric Chemistry and Physics*, 13, 9975–9996, 2013.
- 1678 Chan Miller, C., Jacob, D. J., Marais, E. A., Yu, K., Travis, K. R., Kim, P. S., Fisher, J. A., Zhu, L., Wolfe, G.  
1679 M., Hanisco, T. F., Keutsch, F. N., Kaiser, J., Min, K.-E., Brown, S. S., Washenfelder, R. A., González Abad,  
1680 G., and Chance, K.: Glyoxal yield from isoprene oxidation and relation to formaldehyde: chemical mechanism,  
1681 constraints from SENEX aircraft observations, and interpretation of OMI satellite data, *Atmos. Chem. Phys.*, 17,  
1682 8725–8738, <https://doi.org/10.5194/acp-17-8725-2017>, 2017.
- 1683 Chance, K., Palmer, P. I., Spurr, R. J. D., Martin, R. V., Kurosu, T. P., and Jacob, D.: Satellite observations of  
1684 formaldehyde over North America from GOME, *Geophys. Res. Lett.*, 27, 3461– 3464, 2000.



- 1685 Chen H., Winderlich, J., Gerbig, C., Hoefler, A., Rella, C. W., Crosson, E. R., Van Pelt, A. D., Steinbach, J.,  
1686 Kolle, O., Beck, V., Daube, B. C., Gottlieb, E. W., Chow, V. Y., Santoni, G. W., and S. C. Wofsy, High-  
1687 accuracy continuous airborne measurements of greenhouse gases (CO<sub>2</sub> and CH<sub>4</sub>) using the cavity ring-down  
1688 spectroscopy (CRDS) technique, *Atmos. Mes. Tech.*, 3, 375-386, 2010.
- 1689 Copernicus Climate Change Service (C3S): ERA5: Fifth generation of ECMWF atmospheric reanalyses of the  
1690 global climate. Copernicus Climate Change Service Climate Data Store (CDS), 2017.
- 1691 Crippa, M., DeCarlo, P. F., Slowik, J. G., Mohr, C., Heringa, M. F., Chirico, R., Poulain, L., Freutel, F., Sciare,  
1692 J., Cozic, J., Di Marco, C. F., Elsasser, M., Nicolas, J. B., Marchand, N., Abidi, E., Wiedensohler, A., Drewnick,  
1693 F., Schneider, J., Borrmann, S., Nemitz, E., Zimmermann, R., Jaffrezo, J.-L., Prévôt, A. S. H., and  
1694 Baltensperger, U.: Wintertime aerosol chemical composition and source apportionment of the organic fraction in  
1695 the metropolitan area of Paris, *Atmos. Chem. Phys.*, 13, 961–981, <https://doi.org/10.5194/acp-13-961-2013>,  
1696 2013.
- 1697 Curci, G., Ferrero, L., Tuccella, P., Barnaba, F., Angelini, F., Bolzacchini, E., et al., : How much is particulate  
1698 matter near the ground influenced by upper-level processes within and above the boundary layer? A summertime  
1699 case study in Milan (Italy) evidences the distinctive role of nitrate. , *Atmos. Chem. Phys.*, 15(5), 2629-2649,  
1700 2015
- 1701 De Smedt, I., Stavrou, T., Hendrick, F., Danckaert, T., Vlemmix, T., Pinardi, G., Theys, N., Lerot, C., Gielen,  
1702 C., Vigouroux, C., Hermans, C., Fayt, C., Veeffkind, P., Müller, J.-F., and Van Roozendaal, M.: Diurnal,  
1703 seasonal and long-term variations of global formaldehyde columns inferred from combined OMI and GOME-2  
1704 observations, *Atmos. Chem. Phys.*, 15, 12519–12545, <https://doi.org/10.5194/acp-15-12519-2015>, 2015.
- 1705 De Gouw, J. A., Warneke, C., Parrish, D. D., Holloway, J. S., Trainer, M., and Fehsenfeld, F. C.: Emission  
1706 sources and ocean uptake of acetonitrile (CH<sub>3</sub>CN) in the atmosphere, *J. Geophys. Res.*, D11, 108, 4329,  
1707 doi:10.1029/2002JD002897, 2003.
- 1708 De Sá, S. S., Palm, B. B., Campuzano-Jost, P., Day, D. A., Hu, W., Isaacman-VanWertz, G., Yee, L. D., Brito,  
1709 J., Carbone, S., Ribeiro, I. O., Cirino, G. G., Liu, Y., Thalman, R., Sedlacek, A., Funk, A., Schumacher, C.,  
1710 Shilling, J. E., Schneider, J., Artaxo, P., Goldstein, A. H., Souza, R. A. F., Wang, J., McKinney, K. A., Barbosa,  
1711 H., Alexander, M. L., Jimenez, J. L., and Martin, S. T.: Urban influence on the concentration and composition of  
1712 submicron particulate matter in central Amazonia, *Atmos. Chem. Phys.*, 18, 12185–12206, [doi.org/10.5194/acp-](https://doi.org/10.5194/acp-18-12185-2018)  
1713 18-12185-2018, 2018.
- 1714 Diémoz, H., Barnaba, F., Magri, T., Pession, G., Dionisi, D., Pittavino, S., Tombolato, I., Campanelli, M., Della  
1715 Ceca, L. S., Hervo M., Di Liberto, L., Ferrero, L., Gobbi, G. P.: Transport of Po Valley aerosol pollution to the  
1716 northwestern Alps – Part I: Phenomenology. *Atmospheric Chemistry and Physics*. 19. 3065-3095. [10.5194/acp-](https://doi.org/10.5194/acp-19-3065-2019)  
1717 19-3065-2019, 2019a.
- 1718 Diémoz, H., Gobbi, G.P., Magri, T., Pession, G., Pittavino, S., Tombolato, I.K.F., Campanelli, M., and Barnaba,  
1719 F.: Transport of Po Valley aerosol pollution to the northwestern Alps –Part 2: Long-term impact on air quality,  
1720 *Atmos. Chem. Phys.*, 19, 10129–10160, 2019b.
- 1721 Dodman, D.: Blaming cities for climate change? An analysis of urban greenhouse gas emissions inventories.  
1722 *Environ.Urban*. 21 (No. 1, April), 185–202, 2009.
- 1723 Dufour, G., Wittrock, F., Camredon, M., Beekmann, M., Richter, A., Aumont, B., and Burrows, J. P.:  
1724 SCIAMACHY formaldehyde observations: constraint for isoprene emission estimates over Europe?, *Atmos.*  
1725 *Chem. Phys.*, 9, 1647–1664, <https://doi.org/10.5194/acp-9-1647-2009>, 2009
- 1726 European Environmental Agency: Air quality in Europe - 2019 report, No 10/2019; ISBN 978-92-9480-088-6,  
1727 doi:10.2800/822355.



- 1728 European Strategy and Policy Analysis System, ESPAS, Global Trends to 2030: The future of urbanization and  
1729 Megacities, ESPAS Ideas Paper series, 2018
- 1730 Finardi et al., Analysis of pollutants exchange between the Po Valley and the surrounding European region,  
1731 Urban Climate 2014
- 1732 Fischer, E. V., Jacob, D. J., Yantosca, R. M., Sulprizio, M. P., Millet, D. B., Mao, J., Paulot, F., Singh, H. B.,  
1733 Roiger, A., Ries, L., Talbot, R. W., Dzepina, K., and Pandey Deolal, S.: Atmospheric peroxyacetyl nitrate  
1734 (PAN): a global budget and source attribution, *Atmos. Chem. Phys.*, 14, 2679–2698, <https://doi.org/10.5194/acp-14-2679-2014>, 2014.
- 1736 Fisher, R., Lowry, D., Wilkin, O., Sriskantharajah, S., and Nisbet, E.G.: High-precision, automated stable  
1737 isotope analysis of atmospheric methane and carbon dioxide using continuous-flow isotope-ratio mass  
1738 spectrometry, *Rapid communications in mass spectrometry: RCM*, 20 (2), 200–208. doi: 10.1002/rem.2300,  
1739 2006.
- 1740 Flemming, J., Huijnen, V., Arteta, J., Bechtold, P., Beljaars, A., Blechschmidt, A.-M., Diamantakis, M.,  
1741 Engelen, R. J., Gaudel, A., Inness, A., Jones, L., Josse, B., Katragkou, E., Marecal, V., Peuch, V.-H., Richter, A.,  
1742 Schultz, M. G., Stein, O., and Tsikerdekis, A.: Tropospheric chemistry in the Integrated Forecasting System of  
1743 ECMWF, *Geosci. Model Dev.*, 8, 975-1003, doi:10.5194/gmd-8-975-2015, 2015.
- 1744 Flemming, F., Jones, L., and Blechschmidt, A.-M.: CAMS supports scientific aircraft campaigns, ECMWF  
1745 Newsletter No. 160, Summer 2019, available online at <https://www.ecmwf.int/en/publications/newsletters>.
- 1746 Forzieri, G., Cescatti, A., Batista e Silva, F., Feyen, L.: Increasing risk over time of weather-related hazards to  
1747 the European population: a data-driven prognostic study, *The Lancet Planetary Health*, Vol 1, Issue 5, p e-200-  
1748 e208, 2017
- 1749 Freney, E. J., Sellegri, K., Canonaco, F., Colomb, A., Borbon, A., Michoud, V., Doussin, J.-F., Crumeyrolle, S.,  
1750 Amarouche, N., Pichon, J.-M., Bourianne, T., Gomes, L., Prevot, A. S. H., Beekmann, M., and Schwarzenböck,  
1751 A.: Characterizing the impact of urban emissions on regional aerosol particles: airborne measurements during the  
1752 MEGAPOLI experiment, *Atmos. Chem. Phys.*, 14, 1397–1412, <https://doi.org/10.5194/acp-14-1397-2014>, 2014
- 1753 Freutel, F., Schneider, J., Drewnick, F., von der Weiden-Reinmüller, S.-L., Crippa, M., Prévôt, A. S. H.,  
1754 Baltensperger, U., Poulain, L., Wiedensohler, A., Sciare, J., Sarda-Estève, R., Burkhardt, J. F., Eckhardt, S., Stohl,  
1755 A., Gros, V., Colomb, A., Michoud, V., Doussin, J. F., Borbon, A., Haeffelin, M., Morille, Y., Beekmann, M.,  
1756 and Borrmann, S.: Aerosol particle measurements at three stationary sites in the megacity of Paris during  
1757 summer 2009: meteorology and air mass origin dominate aerosol particle composition and size distribution,  
1758 *Atmos. Chem. Phys.*, 13, 933–959, <https://doi.org/10.5194/acp-13-933-2013>, 2013.
- 1759 Fu, T.-M., Jacob, D. J., Wittrock, F., Burrows, J. P., Vrekoussis, M., and Henze, D. K.: Global budgets of  
1760 atmospheric glyoxal and methylglyoxal, and implications for formation of secondary organic aerosols, *J.*  
1761 *Geophys. Res.-Atmos.*, 113, D15303, <https://doi.org/10.1029/2007JD009505>, 2008.
- 1762 Fu, Y., Tai, A. P. K. and Liao, H.: Impacts of historical climate and land cover  
1763 changes on fine particulate matter (PM<sub>2.5</sub>) air quality in East Asia between 1980 and 2010, *Atmospheric*  
1764 *Chemistry and Physics*, 16(16), pp. 10369–10383. doi: 10.5194/acp-16-10369-2016, 2016.
- 1765 Gardi, C.: *Urban Expansion, Land Cover and Soil Ecosystem Services*, Ed. Taylor & Francis, ISBN  
1766 1317504712, 9781317504719, 2017.
- 1767 Garzon, J.P., Huertas, J. I., Magana, M. Huertas, M.E., Cardenas, B., Watanabe, T., Maeda, T., Wakamatsu, S.,  
1768 Blanco, S.: Volatile organic compounds in the atmosphere of Mexico City, *Atmospheric Environment*, 119, 425-  
1769 429, 2015.



- 1770 Gelencsér, A; Siszler, K; and Hlavay, J: *Environmental Science & Technology* 31 (10), 2869-2872, doi:  
1771 10.1021/es970004c,1997.
- 1772 General, S., Pöhler, D., Sihler, H., Bobrowski, N., Frieß, U., Zielcke, J., Horbanski, M., Shepson, P. B., Stirm, B.  
1773 H., Simpson, W. R., Weber, K., Fischer, C., and Platt, U.: The Heidelberg Airborne Imaging DOAS Instrument  
1774 (HAIDI) – a novel Imaging DOAS device for 2-D and 3-D imaging of trace gases and aerosols, *Atmos. Meas.*  
1775 *Tech.*, 7, 3459-3485, 2014, doi:10.5194/amt-7-3459-2014.
- 1776 George, M., Andrés Hernández, M. D., Nenakhov, V., Liu, Y., and Burrows, J. P.: Airborne measurement of  
1777 peroxy radicals using chemical amplification coupled with cavity ring-down spectroscopy: the PerCEAS  
1778 instrument, *Atmos. Meas. Tech.*, 13, 2577–2600, <https://amt.copernicus.org/articles/13/2577/2020/>, 2020.
- 1779 Gerbig, C., Kley, D., Volz-Thomas, A., Kent, J., Dewey, K., and McKenna, D. S.: Fast response resonance  
1780 fluorescence CO measurements aboard the C-130: Instrument characterization and measurements made during  
1781 North Atlantic Regional Experiment 1993, *J. Geophys. Res.*, 101, 29229-29238, 1996.
- 1782 Gioli, B., Miglietta, F., Vaccari, F. P., Zaldei, A. and De Martino, B.: The Sky Arrow ERA, an innovative  
1783 airborne platform to monitor mass, momentum and energy exchange of ecosystems. *Annals of Geophysics*. 49.  
1784 10.4401/ag-3159, 2009.
- 1785 Gioli, B., Carfora, M.F., Magliulo, V., Metallo, M.C., Poli, A.A., Toscano, P., and Miglietta, F.: Aircraft mass  
1786 budgeting to measure CO<sub>2</sub> emissions of Rome, Italy, *Environmental monitoring and assessment*, 186 (4), 2053–  
1787 2066. DOI: 10.1007/s10661-013-3517-4, 2014.
- 1788 Gkikas, A; Hatzianastassiou, N., Mihalopoulos, N., Katsoulis, V., Kazadzis, S., Pey, J., Querol, X., and Torres,  
1789 O.: The regime of intense desert dust episodes in the Mediterranean based on contemporary satellite observations  
1790 and ground measurements, *Atmos. Chem. Phys.*, 13, 12135–12154, doi:10.5194/acp-13-12135-2013, 2013.
- 1791 Giles, D.M., Sinyuk, A., Sorokin, M.G., Schafer, J.S., Smirnov, A., Slutsker, I., Eck, T.F., Holben, B.N., Lewis,  
1792 J.R., Campbell, J.R., Welton, E.,J., Korkin, S. V., and Lyapustin, A. I. : Advancements in the Aerosol Robotic  
1793 Network (AERONET) Version 3 database – automated near-real-time quality control algorithm with improved  
1794 cloud screening for Sun photometer aerosol optical depth (AOD) measurements, *Atmos. Meas. Tech.*, 12, 169–  
1795 209, doi.org/10.5194/amt-12-169-2019, 2019.
- 1796 Goldstein, A. and Shaw, S.: Isotopes of volatile organic compounds: an emerging approach for studying  
1797 atmospheric budgets and chemistry, *Chem. Rev.*, 103, 5025–5048, doi:10.1021/cr0206566, 2003.
- 1798 Grewe, V., Tsati, E., Mertens, M., Frömming, C., & Jöckel, P.: Contribution of emissions to concentrations: the  
1799 TAGGING 1.0 submodel based on the Modular Earth Submodel System (MESSy 2.52), *Geoscientific Model*  
1800 *Development*, 10, 2615–2633, doi: 10.5194/gmd-10-2615-2017, URL [https://www.geosci-model-](https://www.geosci-model-dev.net/10/2615/2017/)  
1801 [dev.net/10/2615/2017/](https://www.geosci-model-dev.net/10/2615/2017/), 2017
- 1802 Grimm, N.B., Faeth, S.H., Golubiewski, N.E., Redman, C.L., Wu, J., Bai, X., Briggs, J.M.: Global change and  
1803 the ecology of cities. *Science* 319, 756–760. doi.:10.1126/science.1150195, 2008.
- 1804 Guerreiro, S. B., Dawson, R. J., Kilsby, C., Lewis, E., and Ford, A.: Future heat-waves, droughts and floods in  
1805 571 European cities, *Environ. Res. Lett.* 13 034009, doi.org/10.1088/1748-9326/aaaad3, 2018.
- 1806 Haywood, J. and Boucher, O.: Estimates of the direct and indirect radiative forcing due to tropospheric aerosols:  
1807 A review, *Reviews of Geophysics*, 2000, 38.10.1029/1999RG000078.
- 1808 Heckel A., Richter, A. Tarsu T., Wittrock, F., Hak C., Pundt I., Junkermann W. and Burrows J.P. :MAX-DOAS  
1809 measurements of formaldehyde in Po-Valley, *Atmospheric Chemistry and Physics*, 5, 909-918, 2005.
- 1810 Helfter, C., Tremper, A.H., Halios, C.H., Kotthaus, S., Björkegren, A., Grimmond, C.S.B., Barlow, J.F., and  
1811 Nemitz, E.: Spatial and temporal variability of urban fluxes of methane, carbon monoxide and carbon dioxide  
1812 above London, UK, *Atmos. Chem. Phys.*, 16 (16), 10543–10557. DOI: 10.5194/acp-16-10543-2016, 2016



- 1813 Hennigan, C. J., Sullivan, A. P., Collett, J. L., and Robinson, A. L.: Levoglucosan stability in biomass burning  
1814 particles exposed to hydroxyl radicals, *Geophys. Res. Lett.*, 37, L09806, doi:10.1029/2010GL043088, 2010.
- 1815 Hennigan, C. J., Miracolo, M. A., Engelhart, G. J., May, A. A., Presto, A. A., Lee, T., Sullivan, A. P.,  
1816 McMeeking, G. R., Coe, H., Wold, C. E., Hao, W.-M., Gilman, J. B., Kuster, W. C., de Gouw, J., Schichtel, B.  
1817 A., Collett Jr., J. L., Kreidenweis, S. M., and Robinson, A. L.: Chemical and physical transformations of organic  
1818 aerosol from the photo-oxidation of open biomass burning emissions in an environmental chamber, *Atmos.*  
1819 *Chem. Phys.*, 11, 7669–7686, doi.org/10.5194/acp-11-7669-2011, 2011.
- 1820 Hilboll, A., Richter, A., and Burrows, J. P.: Long-term changes of tropospheric NO<sub>2</sub> over megacities derived  
1821 from multiple satellite instruments, *Atmos. Chem. Phys.*, 13, 4145–4169, doi:10.5194/acp-13-4145-2014, 2014
- 1822 Holanda, B.A., Pöhlker, M.L., Walter, D., Saturno, J., Sörgel, M., Ditas, J., Ditas, F., Schulz, C., et al.: Influx of  
1823 African biomass burning aerosol during the Amazonian dry season through layered transatlantic transport of  
1824 black carbon-rich smoke, *Atmos. Chem. Phys.*, 20, 4757–4785, doi.org/10.5194/acp-20-4757-2020, 2020
- 1825 Holanda et al., in preparation 2021: Characteristic correlations between CCN and BC of most relevant aerosol  
1826 species.
- 1827 Holben, B.N., Eck, T.F., Slutsker, I., Tanré, D., Buis, J.P., Setzer, A., Vermote, E., Reagan, J.A., Kaufman, Y.J.,  
1828 Nakajima, T., Lavenu, F., Jankowiak, I., and Smirnov, A.: Aeronet—A Federated Instrument Network and Data  
1829 Archive for Aerosol Characterization. *Remote Sensing of Environment*, 66, 1–16. doi.org/10.1016/S0034-  
1830 4257(98)00031-5, 1998.
- 1831 Hollingsworth, A. R., Engelen, R. J., Textor, C., Benedetti, A., Boucher, O., Chevallier, F., Dethof, A., Elbern,  
1832 H., Eskes, H., Flemming, Granier, C., Kaiser, J. W., Morcrette, J.-J., Rayner, P., Peuch, V.-H., Rouil, L., Schultz,  
1833 M. G., Simmons, A. J., and Consortium, T. G.: Toward a monitoring and forecasting system for atmospheric  
1834 composition: The GEMS project, *B. Am. Meteorol. Soc.*, 89, 1147–1164, 2008
- 1835 Hoole, C., Hincks, S. and Rae, A.: The contours of a new urban world? Megacity population growth and density  
1836 since 1975. *Town Planning Review*, 90 (6). ISSN 0041-0020, 2019. https://doi.org/10.3828/tp.2019.41
- 1837 Hüneke, T., Aderhold, O.-A., Bounin, J., Dorf, M., Gentry, E., Grossmann, K., Groß, J.-U., Hoor, P., Jöckel, P.,  
1838 Kenntner, M., Knapp, M., Knecht, M., Lörks, D., Ludmann, S., Matthes, S., Raecke, R., Reichert, M., Weimar,  
1839 J., Werner, B., Zahn, A., Ziereis, H., and Pfeilsticker, K.: The novel HALO mini-DOAS instrument: inferring  
1840 trace gas concentrations from airborne UV/visible limb spectroscopy under all skies using the scaling method,  
1841 *Atmos. Meas. Tech.*, 10, 4209–4234, https://doi.org/10.5194/amt-10-4209-2017, 2017.
- 1842 Huijnen, V., Williams, J., van Weele, M., van Noije, T., Krol, M., Dentener, F., Segers, A., Houweling, S.,  
1843 Peters, W., de Laat, J., Boersma, F., Bergamaschi, P., van Velthoven, P., Le Sager, P., Eskes, H., Alkemade, F.,  
1844 Scheele, R., Nédélec, P., and Pätz, H.-W.: The global chemistry transport model TM5: description and  
1845 evaluation of the tropospheric chemistry version 3.0, *Geosci. Model Dev.*, 3, 445–473,  
1846 https://doi.org/10.5194/gmd-3-445-2010, 2010.
- 1847 Huntrieser, H., and H. Schlager: Air Pollution Export from and Import to Europe: Experimental Evidence, In:  
1848 *The Handbook of Environmental Chemistry, Vol. 4 Air Pollution: Intercontinental Transport of Air Pollution*  
1849 (Ed. A. Stohl), Springer Verlag, pp. 69–98. 2004.
- 1850 Huntrieser, H., Heland, J., Schlager, H., Forster, C., Stohl, A., Aufmhoff, H., Arnold, F., Scheel, H.E., Campana,  
1851 M., Gilge, S., Eixmann, R., and Cooper, O.: Intercontinental air pollution transport from North America to  
1852 Europe: Experimental evidence from airborne measurements and surface observations, *J. Geophys. Res.*, 110,  
1853 D01305, doi:10.1029/2004JD005045, 2005.
- 1854 Im, U., Markakis, K., Koçak, M., Gerasopoulos, E., Daskalakis, N., Mihalopoulos, N., Poupkou, A., Kindap, T.,  
1855 Unal, A., and Kanakidou, M.: Summertime aerosol chemical composition in the Eastern Mediterranean and its  
1856 sensitivity to temperature, *Atmos. Environ.*, 50, 164–173, https://doi.org/10.1016/j.atmosenv.2011.12.044, 2012.





- 1857 Inness, A., Blechschmidt, A.-M., Bouarar, I., Chabrillat, S., Crepulja, M., Engelen, R. J., Eskes, H., Flemming,  
1858 J., Gaudel, A., Hendrick, F., Huijnen, V., Jones, L., Kapsomenakis, J., Katragkou, E., Keppens, A., Langerock,  
1859 B., de Mazière, M., Melas, D., Parrington, M., Peuch, V. H., Razinger, M., Richter, A., Schultz, M. G., Suttie,  
1860 M., Thouret, V., Vrekoussis, M., Wagner, A., and Zerefos, C.: Data assimilation of satellite-retrieved ozone,  
1861 carbon monoxide and nitrogen dioxide with ECMWF's Composition-IFS, *Atmos. Chem. Phys.*, **15**, 5275-5303,  
1862 doi:10.5194/acp-15-5275-2015, 2015.
- 1863 IPCC, 2014: Climate Change 2014: Synthesis Report. Contribution of Working Groups I, II and III to the Fifth  
1864 Assessment Report of the Intergovernmental Panel on Climate Change (Core Writing Team, R.K. Pachauri and  
1865 L.A. Meyer (eds.)). IPCC, Geneva, Switzerland, 151 pp.
- 1866 Jacob, D.J., and Winner, D.A.: Effect of climate change on air quality, *Atmospheric Environment*, **43**, 51-63,  
1867 doi:10.1016/j.atmosenv.2008.09.051, 2009.
- 1868
- 1869 Jöckel, P., Kerkweg, A., Pozzer, A., Sander, R., Tost, H., Riede, H., Baumgaertner, A., Gromov, S., & Kern, B.:  
1870 Development cycle 2 of the Modular Earth Submodel System (MESSy2), *Geoscientific Model Development*, **3**,  
1871 717–752, doi: 10.5194/gmd-3-717-2010, URL <http://www.geosci-model-dev.net/3/717/2010/>, 2010
- 1872
- 1873 Jonson, J. E., Schulz, M., Emmons, L., Flemming, J., Henze, D., Sudo, K., Tronstad Lund, M., Lin, M.,  
1874 Benedictow, A., Koffi, B., Dentener, F., Keating, T., Kivi, R., and Davila, Y., The effect of intercontinental  
1875 emission sources on European air pollution levels. *Atmos. Chem. Phys.*, **18**, 13655–13672,  
1876 <https://doi.org/10.5194/acp-18-13655-2018>, 2018.
- 1877
- 1878 Kaiser, J. W., Heil, A., Andreae, M. O., Benedetti, A., Chubarova, N., Jones, L., Morcrette, J.-J., Razinger, M.,  
1879 Schultz, M. G., Suttie, M., and van der Werf, G. R.: Biomass burning emissions estimated with a global fire  
1880 assimilation system based on observed fire radiative power, *Biogeosciences*, **9**, 527–554, [https://doi.org/10.5194](https://doi.org/10.5194/bg-9-527-2012)  
1881 [/bg-9-527-2012](https://doi.org/10.5194/bg-9-527-2012), 2012.
- 1882 Kaiser, J., Wolfe, G. M., Min, K. E., Brown, S. S., Miller, C. C., Jacob, D. J., de Gouw, J. A., Graus, M.,  
1883 Hanisco, T. F., Holloway, J., Peischl, J., Pollack, I. B., Ryerson, T. B., Warneke, C., Washenfelder, R. A., and  
1884 Keutsch, F. N.: Reassessing the ratio of glyoxal to formaldehyde as an indicator of hydrocarbon precursor  
1885 speciation, *Atmos. Chem. Phys.*, **15**, 7571–7583, <https://doi.org/10.5194/acp-15-7571-2015>, 2015.
- 1886 Kalivitis, N., Gerasopoulos, E., Vrekoussis, M., Kouvarakis, G., Kubilay, N., Hatzianastassiou, N., Vardavas, I.  
1887 and Mihalopoulos, N., Dust transport over the eastern Mediterranean derived from Total Ozone Mapping  
1888 Spectrometer, Aerosol Robotic Network, and surface measurements, *Journal of Geophysical Research-*  
1889 *Atmospheres* **112**(D3). 2007.
- 1890 Kalnay, E., Kanamitsu, M., Kistler, R., Collins, W., Deaven, D., Gandin, L., Iredell, M., Saha, S., White, G.,  
1891 Woollen, J., Zhu, Y., Leetmaa, A., Reynolds, B., Chelliah, M., Ebisuzaki, W., Higgins, W., Janowiak, J., Mo, K.  
1892 C., Ropelewski, C., Wang, J., Jenne, R., and Joseph, D. : The NCEP/NCAR 40-year reanalysis project, *Bull.*  
1893 *Amer. Meteor. Soc.*, **77**, 437-470, 1996.
- 1894 Kanakidou, M., Mihalopoulos, N., Kindap, T., Im, U., Vrekoussis, M., Gerasopoulos, E., Dermizaki, E., Unal,  
1895 A., Koçak, M., Markakis, K., Melas, D., Kouvarakis, G., Youssef, A.F., Richter, A., Hatzianastassiou, N.,  
1896 Hilboll, A., Ebojje, F., Wittrock, F., von Savigny, C., Burrows, J.P., Ladstaetter-Weissenmayer, A., Moubasher,  
1897 H.: Megacities as hot spots of air pollution in the East Mediterranean, *Atmospheric Environment*, **45**, 1223-  
1898 1235, 2011.
- 1899 Kerkweg, A. & Jöckel, P.: The 1-way on-line coupled atmospheric chemistry model system MECO(n) – Part 2:  
1900 On-line coupling with the Multi-Model-Driver (MMD), *Geoscientific Model Development*, **5**, 111–128, doi:  
1901 10.5194/gmd-5-111-2012, URL <http://www.geosci-model-dev.net/5/111/2012/>, 2012
- 1902 Kluge, F., Hüneke, T., Knecht, M., Lichtenstern, M., Rotermund, M., Schlager, H., Schreiner, B., and  
1903 Pfeilsticker, K.: Profiling of formaldehyde, glyoxal, methylglyoxal, and CO over the Amazon: normalized



- 1904 excess mixing ratios and related emission factors in biomass burning plumes, *Atmos. Chem. Phys.*, 20, 12363–  
1905 12389, <https://doi.org/10.5194/acp-20-12363-2020>, 2020.
- 1906 Klausner, T. M., Aircraft-based in situ measurements of CH<sub>4</sub> and CO<sub>2</sub> downstream of European and Asian urban  
1907 centres at local to synoptic scales. Dissertation, LMU München: Fakultät für Physik, doi: 10.5282/edoc.26983,  
1908 2020.
- 1909 Klausner, T., Mertens, M., Huntrieser, H., Galkowski, M., Kuhlmann, G., Baumann, R., Fiehn, A., Jöckel P.,  
1910 Pühl, M., and Roitger, A.: Urban greenhouse gas emissions from the Berlin area: A case study using airborne  
1911 CO<sub>2</sub> and CH<sub>4</sub> in situ observations in summer 2018. *Elem Sci Anth*, 8: 15, [doi.org/10.1525/elementa.411](https://doi.org/10.1525/elementa.411), 2020.
- 1912 Kuc, T., Rozanski, K., Zimnoch, M., Necki, J.M., and Korus, A.: Anthropogenic emissions of CO<sub>2</sub> and CH<sub>4</sub> in  
1913 an urban environment, *Applied Energy* 2003, 75 (3-4), 193–203. DOI: 10.1016/S0306-2619(03)00032-1.
- 1914 Kunkel, D., M. G. Lawrence, H. Tost, A. Kerckweg, P. Jöckel, and Borrmann S.: Urban emission hot spots as  
1915 sources for remote aerosol deposition, *Geophys. Res. Lett.*, 39, L01808, doi: 10.1029/2011GL049634, 2012.
- 1916 Laborde, M., Crippa, M., Tritscher, T., Jurányi, Z., Decarlo, P. F., Temime-Roussel, B., Marchand, N., Eckhardt,  
1917 S., Stohl, A., Baltensperger, U., Prévôt, A. S. H., Weingartner, E., and Gysel, M.: Black carbon physical  
1918 properties and mixing state in the European megacity Paris, *Atmos. Chem. Phys.*, 13, 5831–5856,  
1919 <https://doi.org/10.5194/acp-13-5831-2013>, 2013.
- 1920 Lai, C., Liu, Y., Ma, J., Ma, Q., He, H.: Degradation kinetics of levoglucosan initiated by hydroxyl radical under  
1921 different environmental conditions, *Atmospheric Environment*, 91, 32-39,  
1922 [doi.org/10.1016/j.atmosenv.2014.03.054](https://doi.org/10.1016/j.atmosenv.2014.03.054), 2014.
- 1923 Lambe, A. T., Onasch, T. B., Massoli, P., Croasdale, D. R., Wright, J. P., Ahern, A. T., Williams, L. R.,  
1924 Worsnop, D. R., Brune, W. H., and Davidovits, P.: Laboratory studies of the chemical composition and cloud  
1925 condensation nuclei (CCN) activity of secondary organic aerosol (SOA) and oxidized primary organic aerosol  
1926 (OPOA), *Atmos. Chem. Phys.*, 11, 8913–8928, [doi.org/10.5194/acp-11-8913-2011](https://doi.org/10.5194/acp-11-8913-2011), 2011.
- 1927 Lawrence, M.G., Butler, T.M., Steinkamp, J., Gurjar, B.R., and J. Lelieveld: Regional pollution potentials of  
1928 megacities and other major population centers, *Atmos. Chem. Phys.*, 7, 3969–3987, doi:10.5194/acp-7-3969-  
1929 2007, 2007.
- 1930 Lawrence, M.G., and Lelieveld, J.: Atmospheric pollutant outflow from southern Asia:  
1931 a review, *Atmos. Chem. Phys.*, 10, 11017–11096, doi:10.5194/acp-10-11017-2010,  
1932 2010.
- 1933 Lelieveld, J., Berresheim, H., Borrmann, S., Crutzen, P.J., Dentener, F.J., Fischer,  
1934 H., et al.: Global air pollution crossroads over the Mediterranean. *Science* 298, 794,  
1935 doi: 10.1126/science.1075457, 2002
- 1936 Lelieveld, J., Evans, J., Fnais, M., Giannadaki, D., and Pozzer, A.: The Contribution of Outdoor Air Pollution  
1937 Sources to Premature Mortality on a Global Scale, *Nature*, vol. 525, pp. 367-371, 2015.
- 1938 Lelieveld, J., Klingmüller, K., Pozzer, A., Burnett, R. T., Haines, A., and Ramanathan, V.: Effects of fossil fuel  
1939 and total anthropogenic emission removal on public health and climate, *P. Natl. Acad. Sci. USA*, 116, 7192–  
1940 7197, <https://doi.org/10.1073/pnas.1819989116>, 2019.
- 1941
- 1942 Lelieveld, J., Pozzer, A., Pöschl, U., Fnais, M., Haines, A., and Münzel, T.: Loss of life expectancy from air  
1943 pollution compared to other risk factors: a worldwide perspective, *Cardiovascular Research*, 116, 1910-1917,  
1944 2020, doi: 10.1093/cvr/cvaa025.
- 1945 Leung, D. M., Tai, A. P. K., Mickley, L. J., Moch, J. M., Van Donkelaar, A., Shen, L. and Martin, R. V.,  
1946 Synoptic meteorological modes of variability for fine particulate matter (PM<sub>2.5</sub>) air quality in major



- 1947 metropolitan regions of China, *Atmospheric Chemistry and Physics*, 18(9), pp. 6733–6748. doi: 10.5194/acp-18-  
1948 6733-2018, 2018.
- 1949 Lian, J., Bréon, F.-M., Broquet, G., Zaccheo, T.S., Dobler, J., Ramonet, M., Stauffer, J., Santaren, D., Xueref-  
1950 Remy, I., and Ciaï, P.: Analysis of temporal and spatial variability of atmospheric CO<sub>2</sub> concentration within  
1951 Paris from the GreenLITE TM laser imaging experiment, *Atmos. Chem. Phys. Discuss.* 2019.  
1952 <https://doi.org/10.5194/acp-2019-547>, in review.
- 1953 Liu, D., Allan, J. D., Young, D. E., Coe, H., Beddows, D., Fleming, Z. L., Flynn, M. J., Gallagher, M. W.,  
1954 Harrison, R. M., Lee, J., Prevot, A. S. H., Taylor, J. W., Yin, J., Williams, P. I., and Zotter, P.: Size distribution,  
1955 mixing state and source apportionment of black carbon aerosol in London during wintertime, *Atmos. Chem.*  
1956 *Phys.*, 14, 10061–10084, <https://doi.org/10.5194/acp-14-10061-2014>, 2014.
- 1957 Mallaun, C., Giez, A. and Baumann, R.: Calibration of 3-D wind measurements on a single engine research  
1958 aircraft *Atmos. Meas. Tech.*, 8, 3177-3196, doi: 10.5194/amt-8-3177-2015, 2015.
- 1959 Mar, K.A., Putting the brakes on climate change – it’s about more than just CO<sub>2</sub>, *Climanosco Research Articles*  
1960 3, <https://doi.org/10.37207/CRA.3.1>, 2021
- 1961 Mayer, M., Wang, C., Webster, M., and Prinn, R. G.: Linking local air pollution to global chemistry and climate,  
1962 *J. Geophys. Res.*, 105, 22869–22896, 2000.
- 1963 Mei, L. L., Rozanov, V., Vountas, M., Burrows, J., Levy, R., Lotz, W., Retrieval of aerosol optical properties  
1964 using MERIS observations: algorithm and some first results, *Remote Sensing of Environment*, doi:10.1016/  
1965 *j.rse.2016.11.015*, 197, 125-140, 2017a
- 1966 Mei, L. L., Rozanov, V., Vountas, M., Burrows, J., Levy, R., Lotz, W., A Cloud masking algorithm for the  
1967 XBAER aerosol retrieval using MERIS data, *Remote Sensing of Environment* doi:  
1968 10.1016/j.rse.2016.11.016, 197, 141-160, 2017b
- 1969 Melchiorri, M.; Florczyk, A.J.; Freire, S.; Ehrlich, D.; Schiavina, M.; Pesaresi, M.; Kemper, T. Megacities  
1970 Spatiotemporal Dynamics Monitored with the Global Human Settlement Layer. In *Proceedings of the REAL*  
1971 *CORP 2018 Expanding Cities—Diminishing Space*, Wien, Austria, 4–6 April 2018; Schrenk, M., Popovisch,  
1972 V. V., Zeile, P., Elisei, P., Beyer, C., Navratil, G., Eds.; CORP: Wien, Austria, 2018; pp. 285–294.
- 1973 Mertens, M., Kerkweg, A., Jöckel, P., Tost, H., & Hofmann, C.: The 1-way on-line coupled model system  
1974 MECO(n) – Part 4: Chemical evaluation (based on MESSy v2.52), *Geoscientific Model Development*, 9, 3545–  
1975 3567, doi: 10.5194/gmd-9-3545-2016, URL <http://www.geosci-model-dev.net/9/3545/2016/>, 2016
- 1976 Mertens, M., Kerkweg, A., Grewe, V., Jöckel, P., & Sausen, R.: Attributing ozone and its precursors to land  
1977 transport emissions in Europe and Germany, *Atmospheric Chemistry and Physics*, 20, 7843–7873, doi:  
1978 10.5194/acp-20-7843-2020, URL <https://www.atmos-chem-phys.net/20/7843/2020/>, 2020
- 1979 Mertens, M., Kerkweg, A., Grewe, V., Jöckel, P., & Sausen, R.: Are contributions of emissions to ozone a matter  
1980 of scale? – a study using MECO(n) (MESSy v2.50), *Geoscientific Model Development*, 13, 363–383, doi:  
1981 10.5194/gmd-13-363-2020, URL <https://www.geosci-model-dev.net/13/363/2020/>, 2020
- 1982 Millán, M.M., Salvador, R., Mantilla, E., Kallos, G.: Photooxidant dynamics in the Mediterranean basin in  
1983 summer: Results from European research projects, *Journal of Geophysical Research*, 102, N0. D7, 8811-8823,  
1984 1997.
- 1985 Millán, M. M., Mantilla, E., Salvador, R., Carratalá, A., Sanz, M. J., Alonso, L., Gangoiti, G., and Navazo, M.:  
1986 Ozone Cycles in the Western Mediterranean Basin: Interpretation of Monitoring Data in Complex Coastal  
1987 Terrain. *Journal of Applied Meteorology*, 39: 487-508. 2000.
- 1988



- 1989 Monks, P. S., Granier, C., Fuzzi, S., Stohl, A., Williams, M. L., Akimoto, H., Amann, M., Baklanov, A.,  
1990 Baltensperger, U., Bey, I., Blake, N., Blake, R. S., Carslaw, K., Cooper, O. R., Dentener, F., Fowler, D.,  
1991 Fragkou, E., Frost, G. J., Generoso, S., Ginoux, P., Grewe, V., Guenther, A., Hansson, H. C., Henne, S., Hjorth,  
1992 J., Hofzumahaus, A., Huntrieser, H., Isaksen, I. S. A., Jenkin, M. E., Kaiser, J., Kanakidou, M., Klimont, Z.,  
1993 Kulmala, M., Laj, P., Lawrence, M. G., Lee, J. D., Liousse, C., Maione, M., McFiggans, G., Metzger, A.,  
1994 Mieville, A., Moussiopoulos, N., Orlandou, J. J., O'Dowd, C. D., Palmer, P. I., Parrish, D. D., Petzold, A., Platt,  
1995 U., Pöschl, U., Prévôt, A. S. H., Reeves, C. E., Reimann, S., Rudich, Y., Sellegri, K., Steinbrecher, R., Simpson,  
1996 D., ten Brink, H., Theloke, J., van der Werf, G. R., Vautard, R., Vestreng, V., Vlachokostas, Ch., von Glasow, R.:  
1997 Atmospheric composition change-global and regional air quality, *Atmospheric Environment*, 43, 5268–5350,  
1998 doi:10.1016/j.atmosenv.2009.08.021, 2009.
- 1999 Myriokefalitakis, S., Vrekoussis, M., Tsigaridis, K., Wittrock, F., Richter, A., Brühl, C., Volkamer, R., Burrows,  
2000 J.P., and Kanakidou, M.: Influence of natural and anthropogenic secondary sources on the glyoxal global  
2001 distribution, *Atmos. Chem. Phys.*, 8, 4965–4981, 2008.
- 2002 Ng, N. L., Canagaratna, M. R., Zhang, Q., Jimenez, J. L., Tian, J., Ulbrich, I. M., Kroll, J. H., Docherty, K. S.,  
2003 Chhabra, P. S., Bahreini, R., Murphy, S. M., Seinfeld, J. H., Hildebrandt, L., Donahue, N. M., DeCarlo, P. F.,  
2004 Lanz, V. A., Prévôt, A. S. H., Dinar, E., Rudich, Y., and Worsnop, D. R.: Organic aerosol components observed  
2005 in Northern Hemispheric datasets from Aerosol Mass Spectrometry, *Atmos. Chem. Phys.*, 10, 4625–4641,  
2006 doi.org/10.5194/acp-10-4625-2010, 2010.
- 2007 Ng, N. L., Canagaratna, M. R., Jimenez, J. L., Chhabra, P. S., Seinfeld, J. H., and Worsnop, D. R.: Changes in  
2008 organic aerosol composition with aging inferred from aerosol mass spectra, *Atmos. Chem. Phys.*, 11, 6465–  
2009 6474, doi.org/10.5194/acp-11-6465-2011, 2011.
- 2010 Odendahl, C., Springford, J., Johnson, S. and J. Murray: The big European sort? The diverging fortunes of  
2011 Europe's regions, Centre for European Reform, [www.cer.eu](http://www.cer.eu); 2019.
- 2012 O'Shea, S.J., Allen, G., Fleming, Z.L., Bauguitte, S.J.-B., Percival, C.J., Gallagher, M.W., Lee, J., Helfter, C.,  
2013 and Nemitz, E.: Area fluxes of carbon dioxide, methane, and carbon monoxide derived from airborne  
2014 measurements around Greater London: A case study during summer 2012, *J. Geophys. Res.* 119 (8), 4940–4952.  
2015 doi: 10.1002/2013JD021269, 2014.
- 2016 Paulot, F., Wunch, D., Crouse, J. D., Toon, G. C., Millet, D. B., DeCarlo, P. F., Vigouroux, C., Deutscher, N.  
2017 M., González Abad, G., Notholt, J., Warneke, T., Hannigan, J. W., Warneke, C., de Gouw, J. A., Dunlea, E. J.,  
2018 De Mazière, M., Griffith, D. W. T., Bernath, P., Jimenez, J. L., and Wennberg, P. O.: Importance of secondary  
2019 sources in the atmospheric budgets of formic and acetic acids, *Atmos. Chem. Phys.*, 11, 1989–2013,  
2020 <https://doi.org/10.5194/acp-11-1989-2011>, 2011.
- 2021 Pappalardo et al., EARLINET: towards an advanced sustainable European aerosol lidar network, *Atmos. Meas.*  
2022 *Tech.*, 7, 2389–2409, doi:10.5194/amt-7-2389-2014, 2014.
- 2023 Paz, S., Goldstein, P., Kordova-Biezuner, L. et al. Differences in Benzene Patterns Among Traffic and Industrial  
2024 Areas and a Prediction Model for Benzene Rates Based on NOx Values. *Water Air Soil Pollut* 226, 161,  
2025 doi.org/10.1007/s11270-015-2406-6, 2015.
- 2026 Pey, J., Querol, X., Alastuey, A., Forastiere, F., and Stafoggia, M.: African dust outbreaks over the  
2027 Mediterranean Basin during 2001–2011: PM10 concentrations, phenomenology and trends, and its relation with  
2028 synoptic and mesoscale meteorology, *Atmos. Chem. Phys.*, 13, 1395–1410, doi:10.5194/acp-13-1395-2013,  
2029 2013.
- 2030 Pikridas, M., Vrekoussis, M., Sciare, J., Mihalopoulos, N., Kleanthous, S., and Savvidis, C. Spatial and temporal  
2031 (short and long-term) variability of submicron, fine and sub-10 µm particulate matter (PM1, PM2.5, PM10) in  
2032 Cyprus, *Atmos. Environ.*, 191:79–93, 2018. doi:10.1016/j.atmosenv.2018.07.048, 2018.



- 2033 Pitt, J.R., Allen, G., Bauguitte, S.J.-B., Gallagher, M.W., Lee, J.D., Drysdale, W., Nelson, B., Manning, A.J., and  
2034 Palmer, P.I.: Assessing London CO<sub>2</sub>, CH<sub>4</sub> and CO emissions using aircraft measurements and dispersion  
2035 modelling, *Atmos. Chem. Phys.* 2019, 19 (13), 8931–8945. DOI: 10.5194/acp-19-8931-2019.
- 2036 Pöhlker, M. L., Pöhlker, C., Ditas, F., Klimach, T., Hrabě de Angelis, I., Araújo, A., Brito, J., Carbone, S.,  
2037 Cheng, Y., Chi, X., Ditz, R., Gunthe, S. S., Kesselmeier, J., Könemann, T., Lavrič, J. V., Martin, S. T.,  
2038 Mikhailov, E., Moran-Zuloaga, D., Rose, D., Saturno, J., Su, H., Thalman, R., Walter, D., Wang, J., Wolff, S.,  
2039 Barbosa, H. M. J., Artaxo, P., Andreae, M. O., and Pöschl, U.: Long-term observations of cloud condensation  
2040 nuclei in the Amazon rain forest – Part 1: Aerosol size distribution, hygroscopicity, and new model  
2041 parametrizations for CCN prediction, *Atmos. Chem. Phys.*, 2016.
- 2042 Pöhlker, M. L., Ditas, F., Saturno, J., Klimach, T., Hrabě de Angelis, I., Araújo, A. C., Brito, J., Carbone, S.,  
2043 Cheng, Y., Chi, X., Ditz, R., Gunthe, S. S., Holanda, B. A., Kandler, K., Kesselmeier, J., Könemann, T., Krüger,  
2044 O. O., Lavrič, J. V., Martin, S. T., Mikhailov, E., Moran-Zuloaga, D., Rizzo, L. V., Rose, D., Su, H., Thalman,  
2045 R., Walter, D., Wang, J., Wolff, S., Barbosa, H. M. J., Artaxo, P., Andreae, M. O., Pöschl, U., and Pöhlker, C.:  
2046 Long-term observations of cloud condensation nuclei over the Amazon rain forest – Part 2: Variability and  
2047 characteristics of biomass burning, long-range transport, and pristine rain forest aerosols, *Atmos. Chem. Phys.*,  
2048 2018.
- 2049 Pöhlker, C., Walter, D., Paulsen, H., Könemann, T., Rodríguez-Caballero, E., Moran-Zuloaga, D., Brito, J.,  
2050 Carbone, S., Degrendele, C., Després, V. R., Ditas, F., Holanda, B. A., Kaiser, J. W., Lammel, G., Lavrič, J. V.,  
2051 Ming, J., Pickersgill, D., Pöhlker, M. L., Praß, M., Löbs, N., Saturno, J., Sörgel, M., Wang, Q., Weber, B.,  
2052 Wolff, S., Artaxo, P., Pöschl, U., and Andreae, M. O.: Land cover and its transformation in the backward  
2053 trajectory footprint region of the Amazon Tall Tower Observatory, *Atmos. Chem. Phys.*, 19, 8425–8470,  
2054 <https://doi.org/10.5194/acp-19-8425-2019>, 2019.
- 2055 Pöschl, U.: Atmospheric aerosols: Composition, transformation, climate and health effects, *Angew. Chem. Int.*  
2056 *Ed.*, 44(46), 7520–7540, doi:10.1002/anie.200501122, doi: 10.1002/anie.200501122, 2005.
- 2057 Ramanathan V., Crutzen P. J., Kiehl J. T., Rosenfeld D.: Aerosols, climate, and the hydrological cycle. *Science*  
2058 294:2119–2124, DOI: 10.1126/science.1064034.
- 2059 Reddington, C.L., McMeeking G., Mann, G.W. Coe, H., Frontoso M. G, Liu, D., Flynn,  
2060 M., Spracklen, D.V., and Carslaw, K.S.: The mass and number size distributions of  
2061 black carbon aerosol over Europe, *Atmos. Chem. Phys.*, 13, 4917-4939, 2013.
- 2062 Rautenhaus, M., G. Bauer, and A. Dörnbrack.: A web service based tool to plan atmospheric research flights.  
2063 *Geosci. Model Dev.*, 5, 55–71, doi.org/10.5194/gmd-5-55-2012. 2012.
- 2064 Ren, Yu, Schlager, H., Martin D.: The Application of TD/GC/NICI–MS with an Al<sub>2</sub>O<sub>3</sub>-PLOT-S Column for the  
2065 Determination of Perfluoroalkylcycloalkanes in the Atmosphere. *Chromatographia*, 77, pp 309-316. doi:  
2066 10.1007/s10337-013-2584-6., 2013.
- 2067 Ren, Y., Baumann, R., Schlager, H.: An airborne perfluorocarbon tracer system and its first application for a  
2068 Lagrangian experiment. *Atmos. Meas. Tech.*, 8, 69-80. doi: 10.5194/amt-8-69-2015, 2015.
- 2069 Richter, A., Burrows, J. P., Nüß, H., Granier, C, Niemeier, U., Increase in tropospheric nitrogen dioxide over  
2070 China observed from space, *Nature*, 437, 129-132, doi: 10.1038/nature04092, 2005.
- 2071 Richter, A., Begoin, M., Hilboll, A., and Burrows, J. P.: An improved NO<sub>2</sub> retrieval for the GOME-2 satellite  
2072 instrument, *Atmos. Meas. Tech.*, 4, 1147-1159, doi:10.5194/amt-4-1147-2011, 2011.
- 2073 Roiger, A., Aufmhoff, H., Stock, P., Arnold, F., Schlager, H.: An aircraft-borne chemical ionization – ion trap  
2074 mass spectrometer (CI-ITMS) for fast PAN and PPN measurements. *Atmos. Meas. Tech.*, 4, 173-188. DOI:  
2075 10.5194/amt-4-173-2011, 2011.



- 2076 Rolph, G., Stein, A., and Stunder, B.: Real-time Environmental Applications and Display sYstem: READY.  
2077 Environmental Modelling & Software, 95, 210-228, <https://doi.org/10.1016/j.envsoft.2017.06>, 2017.
- 2078 Rosenfeld, D., Lohmann, U., Raga, G. B., O'Dowd, C. D., Kulmala, M., Fuzzi, S., Reissell, A., and Andreae, M.  
2079 O.: Flood or drought: How do aerosols affect precipitation?, Science, 321, 1309-1313, 10.1126/science.1160606,  
2080 2008.
- 2081 Rudolph, J., Czuba, E., and Huang, L.: The stable carbon isotope fractionation for reactions of selected  
2082 hydrocarbons with OH-radicals and its relevance for atmos-pheric chemistry, J. Geophys. Res., 105, 29329–  
2083 29346, doi:10.1029/2000JD900447, 2000.
- 2084 Schneider, J., Weimer, S., Drewnick, F., Borrmann, S., Helas, G., Gwaze, P., Schmid, O., Andreae, M. O. and  
2085 Kirchner, U.: Massspectrometric analysis and aerodynamic properties of various types of combustion-related  
2086 aerosol particles, Int. J. Mass. Spec., 258, 37–49, doi.org/10.1016/j.ijms.2006.07.008, 2006.
- 2087 Schroder, J. C., Campuzano-Jost, P., Day, D. A., Shah, V., Larson, K., Sommers, J. M., et al. (2018). Sources  
2088 and secondary production of organic aerosols in the northeastern United States during WINTER. Journal of  
2089 Geophysical Research: Atmospheres, 123, 7771– 7796. doi.org/10.1029/2018JD028475
- 2090 Schulz, C., Schneider, J., Holanda, B. A., Appel, O., Costa, A., de Sá, S.S., Dreiling, V. Fütterer, D., Jurkat-  
2091 Witschas, T., Klimach, T., Knote, C., Krämer, M., Martin, S.T., Mertes, S., Pöhlker, M.L., Sauer, D., Voigt, C.,  
2092 Walser, A., Weinzierl, A.B., Ziereis, H., Zöger, M., Andreae, M.O., Artaxo, P., Machado, L.-A.T., Pöschl, U.,  
2093 Wendisch, M., and S. Borrmann, Aircraft-based observations of isoprene-epoxydiol-derived secondary organic  
2094 aerosol (IEPOX-SOA) in the tropical upper troposphere over the Amazon region. Atmos. Chem. Phys., 18,  
2095 14979–15001, 2018, <https://doi.org/10.5194/acp-18-14979-2018>.
- 2096 Schumann, U.: Measurement and model data comparisons for the HALO-FAAM formation flight during  
2097 EMERGe on 17 July 2017, DLR FB 2020-48, doi:10.5281/zenodo.4427965, 2020.
- 2098 Schwarz, J. P., Gao, R.S., Spackman, J.R., Watts, L.A., Thomson, D.S., Fahey, D.W., Ryerson, T.B., Peischl, J.,  
2099 Holloway, J.S., Trainer, M., Frost, G.J., Baynard, T., Lack, D.A., de Gouw, J.A., Warneke, C., and Del Negro,  
2100 L.A.: Measurement of the mixing state, mass, and optical size of individual black carbon particles in urban and  
2101 biomass burning emissions, Geophys. Res. Lett., 35, L13810, doi:10.1029/2008GL033968, 2008.
- 2102 Shaw, M. D., Lee, J. D., Davison, B., Vaughan, A., Purvis, R. M., Harvey, A., Lewis, A. C., and Hewitt, C. N.:  
2103 Airborne determination of the tempo-spatial distribution of benzene, toluene, nitrogen oxides and ozone in the  
2104 boundary layer across Greater London, UK, Atmos. Chem. Phys., 15, 5083–5097, doi.org/10.5194/acp-15-5083-  
2105 2015, 2015.
- 2106 Silver, B., Reddington, C.L., Arnold, S.R., and Spracklen: Substantial changes in air pollution across China  
2107 during 2015-2017, Environ. Res. Lett. 13, 114012, 2018.
- 2108 Simpson, I. J., Akagi, S. K., Barletta, B., Blake, N. J., Choi, Y., Diskin, G. S., Fried, A., Fuelberg, H. E.,  
2109 Meinardi, S., Rowland, F. S., Vay, S. A., Weinheimer, A. J., Wennberg, P. O., Wiebring, P., Wisthaler, A.,  
2110 Yang, M., Yokelson, R. J., and Blake, D. R.: Boreal forest fire emissions in fresh Canadian smoke plumes: C1-  
2111 C10 volatile organic compounds (VOCs), CO<sub>2</sub>, CO, NO<sub>2</sub>, NO, HCN and CH<sub>3</sub>CN, Atmos. Chem. Phys., 11,  
2112 6445–6463, <https://doi.org/10.5194/acp-11-6445-2011>, 2011.
- 2113 Speidel, M., Nau, R., Arnold, F., Schlager, H., A. Stohl, Sulfur dioxide measurements in the lower, middle and  
2114 upper troposphere: Deployment of an aircraft-based chemical ionization mass spectrometer with permanent in-  
2115 flight calibration, Atmospheric Environment, 41, 2427-2437, doi:10.1016/j.atmosenv.2006.07.047. 2007.
- 2116 Stein, A.F., Draxler, R.R., Rolph, G.D., Stunder, B.J.B., Cohen, M.D., and Ngan, F.: NOAA's HYSPLIT  
2117 atmospheric transport and dispersion modeling system, Bull. Amer. Meteor. Soc., 96, 2059-2077,  
2118 doi.org/10.1175/BAMS-D-14-00110.1, 2015.



- 2119 Stohl, A., Wotawa, G. Seibert, P. and Kromp-Kolb H.: Interpolation errors in wind fields as a function of spatial  
2120 and temporal resolution and their impact on different types of kinematic trajectories. *J. Appl. Meteor.* 34, p.  
2121 2149-2165, 1995.
- 2122 Stohl, A., Haimberger, L., Scheele, M.P. and Wernli, H.: An intercomparison of results from three trajectory  
2123 models. *Meteorol. Applications* 8, 127-135, 1999.
- 2124 Stohl, A., Eckhardt, S., Forster, C., James, P., and Spichtinger, N.: On the pathways and timescales of  
2125 intercontinental air pollution transport. *J. Geophys. Res.*, 107(D23), 4684, doi:10.1029/2001JD001396, 2002.
- 2126 Stohl, A., Forster, C., Eckhardt, S., Spichtinger, N., Huntrieser, H., Heland, J., Schlager, H., Wilhelm, S.,  
2127 Arnold, F., and Cooper, O.: A backward modeling study of intercontinental pollution transport using aircraft  
2128 measurements. *J. Geophys. Res.*, 108(D12), 4370, doi:10.1029/2002JD002862, 2003.
- 2129 Tan, Z., Fuchs, H., Lu, K., Hofzumahaus, A., Bohn, B., Broch, S., Dong, H., Gomm, S., Häseler, R., He, L.,  
2130 Holland, F., Li, X., Liu, Y., Lu, S., Rohrer, F., Shao, M., Wang, B., Wang, M., Wu, Y., Zeng, L., Zhang, Y.,  
2131 Wahner, A., and Zhang, Y.: Radical chemistry at a rural site (Wangdu) in the North China Plain: observation and  
2132 model calculations of OH, HO<sub>2</sub> and RO<sub>2</sub> radicals, *Atmos. Chem. Phys.*, 17, 663–690,  
2133 <https://doi.org/10.5194/acp-17-663-2017>, 2017.
- 2134 Taraborrelli, D., Cabrera-Perez, D., Bacer, S., Gromov, S., Lelieveld, J., Sander, R., and Pozzer, A.: Influence of  
2135 aromatics on tropospheric gas-phase composition, *Atmos. Chem. Phys. Discuss.*, [https://doi.org/10.5194/acp-](https://doi.org/10.5194/acp-2020-461)  
2136 2020-461, 2020.
- 2137 Thieuleux, F., Moulin, C., Bréon, F. M. , Maignan, F., Poitou, J. , and Tanré, D.: Remote Sensing of Aerosols  
2138 over the oceans using MSG/SEVIRI Imagery, *Ann. Geophys.*, 23, 3561-3568, doi:10.5194/angeo-23-3561-2005
- 2139 Titos, G., Ealo, M., Román, R., Cazorla, A., Sola, Y., Dubovik, O., Alastuey, A., Pandolfi, M.: Retrieval of  
2140 aerosol properties from ceilometer and photometer measurements: long-term evaluation with in situ data and  
2141 statistical analysis at Montsec (southern Pyrenees), *Atmos. Meas. Tech.*, [https://doi.org/10.5194/amt-12-3255-](https://doi.org/10.5194/amt-12-3255-2019)  
2142 2019
- 2143 Turco, M. et al., : Exacerbated Fires in Mediterranean Europe Due to Anthropogenic Warming Projected with  
2144 Non-Stationary Climate-Fire Models, *Nature Communications* 9, no. 1 (December 2018): 3821,  
2145 <https://doi.org/10.1038/s41467-018-06358-z>.
- 2146 United Nations, Department of Economic and Social Affairs, Population Division World Urbanization  
2147 Prospects: The 2018 Revision (ST/ESA/SER.A/420). New York: United Nations, 2019.
- 2148 United Nations Environment Programme (UNEP), World Meteorological Organization (WMO), Integrated  
2149 Assessment of Black Carbon and Tropospheric Ozone, ISBN:92-807-3141-6, 2011.
- 2150 Viidanoja, J., Reiner, T. and Arnold, F: Laboratory investigations of negative ion molecule reactions of formic  
2151 and acetic acids: Implications for atmospheric measurements by Ion Molecule Reaction Mass Spectrometry, *Int.*  
2152 *J. Mass Spectrom.*, 181, 31-41, 1998.
- 2153 Volz-Thomas, A., Xueref, I., and Schmitt, R.: Automatic gas chromatograph and calibration system for ambient  
2154 measurements of PAN and PPN, *Environ. Sci. Poll. Res.*, 9, 72-76, 2001.
- 2155 von der Weiden-Reinmüller, S.-L., Drewnick, F., Zhang, Q. J., Freutel, F., Beekmann, M., and Borrmann, S.:  
2156 Megacity emission plume characteristics in summer and winter investigated by mobile aerosol and trace gas  
2157 measurements: the Paris metropolitan area, *Atmos. Chem. Phys.*, 14, 12931–12950, [https://doi.org/10.5194/acp-](https://doi.org/10.5194/acp-14-12931-2014)  
2158 14-12931-2014, 2014.
- 2159 Vrekoussis, M., Wittrock, F., Richter, A., Burrows, J.P: Temporal and spatial variability of glyoxal as observed  
2160 from space” *Atmos. Chem. Phys.*, 9, 4485-4504, 2009.



- 2161 Vrekoussis, M., Richter, A., Hilboll, A., Burrows, J. P., Gerasopoulos, E., Lelieveld, J., Barrie, L., Zerefos, C.,  
2162 and Mihalopoulos, N. Economic crisis detected from space: Air quality observations over Athens/Greece,  
2163 *Geophys. Res. Lett.*, 40, 458–463, doi:10.1002/grl.50118, 2013.
- 2164 Whalley, L. K., Stone, D., Dunmore, R., Hamilton, J., Hopkins, J. R., Lee, J. D., Lewis, A. C., Williams, P.,  
2165 Kleffmann, J., Laufs, S., Woodward-Massey, R., and Heard, D. E.: Understanding in situ ozone production in  
2166 the summertime through radical observations and modelling studies during the Clean air for London project  
2167 (ClearLo), *Atmos. Chem. Phys.*, 18, 2547–2571, <https://doi.org/10.5194/acp-18-2547-2018>, 2018.
- 2168 Whalley, L. K., Slater, E. J., Woodward-Massey, R., Ye, C., Lee, J. D., Squires, F., Hopkins, J. R., Dunmore, R.  
2169 E., Shaw, M., Hamilton, J. F., Lewis, A. C., Mehra, A., Worrall, S. D., Bacak, A., Bannan, T. J., Coe, H.,  
2170 Percival, C. J., Ouyang, B., Jones, R. L., Crilley, L. R., Kramer, L. J., Bloss, W. J., Vu, T., Kotthaus, S.,  
2171 Grimmond, S., Sun, Y., Xu, W., Yue, S., Ren, L., Acton, W. J. F., Hewitt, C. N., Wang, X., Fu, P., and Heard,  
2172 D. E.: Evaluating the sensitivity of radical chemistry and ozone formation to ambient VOCs and NOx in Beijing,  
2173 *Atmos. Chem. Phys.*, 21, 2125–2147, <https://doi.org/10.5194/acp-21-2125-2021>, 2021.
- 2174 Warneke, C., van der Veen, C., Luxembourg, S., de Gouw, J.A., Kok A.: Measurements of benzene and toluene  
2175 in ambient air using proton-transfer-reaction mass spectrometry: calibration, humidity dependence, and field  
2176 intercomparison, *International Journal of Mass Spectrometry*, Volume 207, Issue 3, doi.org/10.1016/S1387-  
2177 3806(01)00366-9, 2001.
- 2178 Warneke, C., McKeen, S. A., de Gouw, J. A., Goldan, P. D., Kuster, W. C., Holloway, J. S., Williams, E. J.,  
2179 Lerner, B. M., Parrish, D. D., Trainer, M., Fehsenfeld, F. C., Kato, S., Atlas, E. L., Baker, A., and Blak, D. R.:  
2180 Determination of urban volatile organic compound emission ratios and comparison with an emissions database,  
2181 *J. Geophys. Res.*, 112, D10S47, doi:10.1029/2006JD007930, 2007.
- 2182 Warneke, C., Froyd, K. D., Brioude, J., Bahreini, R., Brock, C. A., Cozic, J., de Gouw, J. A., Fahey, D. W.,  
2183 Ferrare, R., Holloway, J. S., Middlebrook, A. M., Miller, L., Montzka, S., Schwarz, J. P., Sodemann, H.,  
2184 Spackman, J. R., and Stohl, A.: An important contribution to springtime Arctic aerosol from biomass burning in  
2185 Russia, *Geophys. Res. Lett.*, 37, L01801, doi:10.1029/2009GL041816, 2010.
- 2186 Wendisch, M., et al.: The ACRIDICON-CHUVA campaign: Studying tropical deep convective clouds and  
2187 precipitation over Amazonia using the new German research aircraft HALO, *Bull. Amer. Meteorol. Soc.*, 97,  
2188 1885-1908, doi: 10.1175/BAMS-D-14-00255, 2016.
- 2189 Wennberg, P. O., Bates, K. H., Crouse, J. D., Dodson, L. G., Mc-Vay, R. C., Mertens, L. A., Nguyen, T. B.,  
2190 Praske, E., Schwantes, R. H., Smarte, M. D., St Clair, J. M., Teng, A. P., Zhang, X., and Seinfeld, J. H.: Gas-  
2191 Phase Reactions of Isoprene and Its Major Oxidation Products, *Chem. Rev.*, 118, 3337–3390,  
2192 doi:10.1021/acs.chemrev.7b00439, 2018.
- 2193 Winkler J., Blank, P., Glaser, K., Gomes, J.A.G., Habram, M., Jambert, C., Jaeschke, W., Konrad, S.,  
2194 Kurtenbach, R., Lenschow, P., Lörzer, J.C., Perros, P.E., Pesch, M., Prümke, H.J., Rappenglück, B., Schmitz,  
2195 Th., Slemr, F., Volz-Thomas, A., and Wickert, B.: Ground-Based and Airborne Measurements of Nonmethane  
2196 Hydrocarbons in BERLIOZ: Analysis and Selected Results, *Journal of Atmospheric Chemistry* 42: 465–492,  
2197 2002.
- 2198 Wintel, J., Hösen, E., Koppmann, R., Krebsbach, M., Hofzumahaus, A., and Rohrer, F.: Stable carbon isotope  
2199 ratios of toluene in the boundary layer and the lower free troposphere, *Atmos. Chem. Phys.*, 13, 11059-11071,  
2200 doi:10.5194/acp-13-11059-2013, 2013.
- 2201 World Health Organization (WHO), Review of evidence on health aspects of air pollution – REVIHAPP Project.  
2202 WHO Regional Office for Europe, Copenhagen, Denmark, 2013.
- 2203 Zahn, A., Weppner, J., Widmann, H., Schlote-Holubek, K., Burger, B., Kühner, T., Franke, H.: A fast and  
2204 precise chemiluminescence ozone detector for eddy flux and airborne application, *Atmos. Meas. Tech.*, 5 (2),  
2205 363–375. doi:10.5194/amt-5-363-2012, 2012.





- 2206 Zhang, Y. H., Su, H., Zhong, L. J., Cheng, Y. F., Zeng, L. M., Wang, X. S., Xiang, Y. R., Wang, J. L., Gao, D.  
2207 F., Shao, M., Fan, S. J., and Liu, S. C.: Regional ozone pollution and observation-based approach for analyzing  
2208 ozone-precursor relationship during the PRIDE-PRD2004 campaign, *Atmos. Environ.*, 42, 6203–6218,  
2209 <https://doi.org/10.1016/j.atmosenv.2008.05.002>, 2008.
- 2210 Zhu, T., Melamed, M., Parrish, D. Gauss, M., Gallardo Klenner, L., Lawrence, M., Konare, A. and Liousse, C.:  
2211 Impacts of Megacities on air pollution and climate, WMO/ IGAC, GAW Report No.205. 2012.
- 2212 Ziereis, H., Minikin, A., Schlager, H., Gayet, J.F., Auriol, F., Stock, P., Baehr, J., Petzold, A., Schumann, U.,  
2213 Weinheimer, A., Ridley, B., and Ström, J.: Uptake of reactive nitrogen on cirrus cloud particles during INCA,  
2214 *Geophys. Res. Lett.*, 31(5), 2004.
- 2215 Zimnoch, M., Necki, J., Chmura, L., Jasek, A., Jelen, D., Galkowski, M., Kuc, T., Gorczyca, Z., Bartyzel, J., and  
2216 Rozanski, K.: Quantification of carbon dioxide and methane emissions in urban areas: Source apportionment  
2217 based on atmospheric observations, *Mitig Adapt Strateg Glob Change* 2019, 24 (6), 1051–1071. DOI:  
2218 [10.1007/s11027-018-9821-0](https://doi.org/10.1007/s11027-018-9821-0).